# Determination of field output factors and volume averaging correction factors for different detectors in narrow Co-60 beams

**Šegedin, Nikola**

UNIVERSITY OF RIJEKA

FACULTY OF PHYSICS

Nikola Šegedin

# DETERMINATION OF FIELD OUTPUT FACTORS AND VOLUME AVERAGING CORRECTION FACTORS FOR DIFFERENT DETECTORS IN NARROW CO-60 BEAMS

DOCTORAL DISSERTATION

Rijeka, 2024.

UNIVERSITY OF RIJEKA

FACULTY OF PHYSICS

Nikola Šegedin

# DETERMINATION OF FIELD OUTPUT FACTORS AND VOLUME AVERAGING CORRECTION FACTORS FOR DIFFERENT DETECTORS IN NARROW CO-60 BEAMS

Supervisor:       Assoc. Prof. Slaven Jurković, PhD

Co-supervisors:  Asst. Prof. Hrvoje Hršak, PhD

Assoc. Prof. Sanja Dolanski Babić, PhD

Rijeka, 2024.

Mentor rada: izv. prof. dr. sc. Slaven Jurković

Komentori: doc. dr. sc. Hrvoje Hršak

izv. prof. dr. sc. Sanja Dolanski Babić

Doktorski rad obranjen je dana _____ u/na _____
_____, pred povjerenstvom u sastavu:

1. _____

2. _____

3. _____

4. _____

5. _____

# Determination of field output factors and volume averaging correction factors for different detectors in narrow Co-60 beams

## Abstract

Accurate small photon field dosimetry is critical for the effectiveness and outcome of the treatment in radiation oncology. Small photon field dosimetry refers to the determination of an absorbed dose in a photon beam whose size is smaller than 3 cm · 3 cm. It is complex due to the finite size of the detector, loss of lateral charged particle equilibrium, and perturbation of secondary electron fluence by the detector. Absorbed dose distributions of a small photon field with nominal field sizes of 16 mm, 8 mm, or 4 mm delivered by Gamma Knife is characterised by a large dose gradient and an ellipsoidal shape. This work aims to experimentally determine detector-specific field output correction factors and measurement uncertainties in such small photon fields for different detectors commonly used for dosimetry of small Co-60 beams delivered by a Gamma Knife. Detector-specific correction factors of active detectors are determined by dividing field output factors of Monte Carlo calculated and EBT3 film measured values with values of active detectors. In addition, volume averaging correction factors and their contribution to a detector-specific field output correction factor were determined. This has been done by the simulation of the detector's geometry and position within the ellipsoid absorbed dose model and integration over the detector's volume. Finally, dose profiles were measured in non-reference geometry. An analysis of measured profiles was performed, and detectors appropriate for such dose profile measurements are recommended.

# Određivanje korekcijskih faktora za izlazne faktore polja i korekcijskih faktora na volumno usrednjavanje za različite detektore u uskim fotonskim snopovima Co-60

## Prošireni sažetak

Dozimetrija malih polja obuhvaća određivanje apsorbirane doze u uskim snopovima fotona veličine manje od 3×3 cm$^2$. Raspodjele apsorbirane doze snopova Co-60 Gamma Knife uređaja karakterizirane su velikim gradijentom doze i elipsoidnim oblikom nominalnih veličina: 16, 8 ili 4 mm. Dozimetrija malih polja je složena zbog veličine detektora, narušenih uvjeta bočne elektronske ravnoteže i utjecaja detektora na tok sekundarnih elektrona. Cilj rada je eksperimentalno odrediti izlazne faktora polja, njihove korekcije u odnosu na referentne vrijednosti kao i odrediti mjerne nepouzdanosti za različite vrste i tipove detektora. Dodatno su određeni korekcijski faktori na volumno usrednjavanja za različite detektore te njihov doprinos u ukupnoj korekciji. To je učinjeno simulacijom geometrije i položaja detektora unutar elipsoidnog modela raspodjele doze. Također, izmjereni su profili doza gama noža različitim detektorima te su uspoređeni s vrijednostima dobivenim Monte Carlo simulacijama. Analizom rezultata preporučen je detektor najpogodniji za određivanje profila u nereferentnoj geometriji.

Izlazni faktori za snopove gama noža određeni su za dvanaest detektora; sedam ionizacijskih komora, četiri poluvodička detektora te jedan dijamantni detektor. Detektori su prilikom mjerenja bili postavljeni u plastičnom (*eng. solid water*) fantomu paralelno sa z-osi Gamma Knife-a. Usporedbom dobivenih rezultata s podacima dobivenim Monte Carlo simulacijama te onih određenih referentnim dozimetrom (radiokromski EBT3 film) utvrđeno je da ionizacijske komore podcjenjuju veličinu izlaznih faktora zbog narušenih uvjeta bočne elektronske ravnoteže, izraženog volumnog usrednjavanja odziva detektora te činjenice da su napravljene

od tkivu ne ekvivalentnog materijala. Sukladno očekivanjima, veličina odstupanja raste s veličinom efektivnog volumena ionizacijske komore. Zbog perturbacija detektora na snop Co-60, odziv detektora je potrebno korigirati korekcijskim faktorom specifičnim za pojedini detektor. Pokazano je da ionizacijske komore Semiflex T31010, Semiflex 3D T331021, PinPoint T31014, PinPoint 3D T3016, RAZOR i CC04, zbog veličine efektivnog volumena, nisu primjerene za dozimetriju u najmanjem polju Gamma Knife-a od 4 mm i njihovi korekcijski faktori su izvan granica prihvatljivosti. S povećanjem veličine polja smanjuje se utjecaj spomenutih perturbacija na točnost određivanja izlaznih faktora. Tako, izlazni faktori RAZORnano ionizacijske komore najmanjeg efektivnog volumena pokazuju najbolje slaganje s referentnim vrijednostima, ali i s rezultatima dobivenim EBT3 filmom. Apsorbirana doza određena na temelju mjerenja silicijevim poluvodičkim detektorom je precijenjena prvenstveno zbog većeg efektivnog atomskog broja silicija u odnosu na vodu. U 8 mm polju, izlazni faktori određeni s ovim detektorima pokazuju statistički značajno slaganje s Monte Carlo vrijednostima. Neki poluvodički detektori imaju zaštitu efektivnog volumena od raspršenih fotona niskih energija te su prvenstveno namijenjeni dozimetriji velikih polja. Pokazano je da se oni također mogu koristiti i u dozimetriji uskih snopova Co-60 kao kod Gamma Knife-a. Izlazni faktori određeni s ovim detektorima pokazuju manje slaganja s Monte Carlo vrijednostima od poluvodičkih detektora bez zaštite. Sintetički jednokristalni detektor se pokazao kao odličan izbor za dozimetriju malih polja gama noža.

Korekcijski faktori volumnog usrednjavanja detektora određeni su primjenom analitičkog elipsoidnog modela raspodjele apsorbirane doze polja Gamma Knife-a te simuliranjem geometrije efektivnog volumena detektora unutar takvih raspodjela. Integriranjem modela apsorbirane doze po efektivnom volumenu detektora izračunata je korekcija na volumno usrednjavanje odziva za četrnaest detektora: šest ionizacijskih komora, pet poluvodičkih detektora, dva plastična scintilacijska detektora te sintetički jednokristalni detektor. U pravilu se korekcijski faktor na volumeno usrednjavanje odziva povećava s volumenom detektora. Međutim, rezultati ranijih istraživanja su pokazala da je osim veličine efektivnog volumena bitan i njegov oblik što je potvrđeno i ovim modelom. Primjerice, ionizacijska komora PinPoint T31014 u usporedbi s ionizacijskom komorom CC04 ima veći korekcijski faktor na volumno usrednjavanje iako komora CC04 ima tri puta veći volumen, i to prvenstveno zbog veće duljine

detektora tj. komora CC04 je kompaktnija. Omjer duljine i promjera aktivnog volumena (l/d) CC04 komoru iznosi 0,9 dok za PinPoint T31014 on iznosi 2,5.

Profili doze određeni su dozimetrijski korištenjem različitih vrsta i tipova detektora te su dobiveni rezultati uspoređeni s profilima određeni Monte Carlo simulacijama. Ionizacijske komore većeg volumena nisu primjerene za mjerenja profila doze jer su im efektivni volumeni preveliki za točno mjerenje odziva u području velikih gradijenta doze. S druge strane, sintetički jednokristalni detektor i poluvodički detektori pokazuju manja odstupanja od referentnih vrijednosti te su dobar izbor za određivanje profila doza.

**Ključne riječi**: dozimetrija malih fotonskih polja, gama nož, volumno usrednjavanje, korekcijski faktori, izlazni faktori, profili apsorbirane doze

# Table of Contents

# 1. Introduction and Motivation

Stereotactic radiosurgery (SRS) with narrow photon beams has started in the early 1950s by the Swedish neurosurgeon Lars Leksell who used a stereotactic frame of his own design to accurately determine a focal point of Cobalt 60 (Co-60) beams to treat small brain tumours and malformations. This has led to the development of the first Leksell Gamma Knife (LGK, Elekta Instruments AB, Stockholm, Sweden). The success of the first Gamma Knife (GK) has led to the creation of clinical radiosurgery accelerators almost simultaneously both in the United Kingdom and the United States of America, and soon spread across the world.[1,2] From the creation of the first Gamma Knife to the present, over 1 million patients have been treated, with about 80 000 new patients each year, in more than 300 Gamma Knife centres worldwide.[3,4] With the expected increase in the number of patients diagnosed with cancer, specialized treatments such as stereotactic radiosurgery and stereotactic body radiation therapy (SBRT) will be even more important and used as a method of choice for cancer treatment.[5–7]

Field sizes of photon beams that traditionally spanned from 3×3 cm$^2$ to 40×40 cm$^2$ are now being regularly collimated down to 4×4 mm$^2$ making most of the available radiation detectors too large for accurate dosimetry. Therefore, the behaviour of detectors in various types of narrow photon fields is still a subject of investigation. Narrow photon beams are commonly used in modern radiation oncology and; therefore, accurate and precise dosimetry of such fields is crucial for the effective delivery of radiation therapy. Studies from the early 2000s have shown a substantial problem in the determination of an absorbed dose in narrow fields.[8,9] Despite this, the use of narrow and non-standard fields in radiotherapy and stereotactic radiosurgery has increased significantly, creating a need for a unifying approach to standardize and enable accurate delivery of absorbed dose to the target volume while minimizing the exposure to the surrounding tissue. This has led to the collaboration of The American Association of Physicists in Medicine (AAPM) and the International Atomic Energy Agency (IAEA) in creating the first international Code of Practice (CoP), Technical Report Series 483 (TRS-483) dedicated to the dosimetry of small static field that fulfilled the need for a systematic and internationally unified approach to the dosimetry of small static fields.[10,11]

Leksell Gamma Knife Icon is one of the radiosurgery units that use small photon fields to deliver a high-absorbed dose (up to 100 Gy). High absorbed dose delivery accuracy is achieved with a rigid Tungsten collimator providing three different field sizes: 16, 8, and 4 mm. The 16, 8, and 4 mm field can be related to the respective beam collimator aperture, and these values represent a projection of a diameter for a single collimator hole to the device's isocentre.[13] In practice, photons are emitted by 192 Co-60 sources and are focused on a single point (isocentre) with a spatial error smaller than 0.3 mm. The resulting absorbed dose is ellipsoidal in shape. For brevity in the further text, the terms 16 mm, 8 mm, and 4 mm field size will be used. For absorbed dose calculation, the determination of field output factors (OF) and dose profiles is of paramount importance since they are input parameters for the calculation algorithm built into the system for calculation and optimization of absorbed dose distribution, also known as treatment planning system (TPS). Field output factor determination of narrow Co-60 beams is demanding due to the steep dose gradients (up to 70 %/mm), loss of lateral charged particle equilibrium (LCPE), perturbation of secondary electron fluence by the difference in detectors and tissue stopping powers, and dose volume-averaging of the detector.[11–15] This effect is especially pronounced in the 4 mm field size being comparable with the size of detector.[13,16] Unlike standard phantoms in which measurements are performed, most of the detectors used are not tissue equivalent and there is a perturbation of secondary electron fluence, which affects the reading of the detector. To correct perturbations, a detector-specific correction factor (DSCF) is introduced. The detector-specific correction factor accounts for the volume-averaging effect, beam perturbation due to the non-water equivalence of the detector, and spectral dependence of the photon energy absorption in the medium.[11,14]

There are three research hypotheses and subsequent objectives of this dissertation:

- Data acquired with a perturbation-free detector (GAFChromic EBT3 radiochromic films, Ashland Advanced Materials, Bridgewater NJ) along with available data determined using Monte Carlo simulation will enable the determination of field output factors and the detector-specific correction factors for detectors not listed in the IAEA TRS-483 CoP.

- Analytically modelled ellipsoidal absorbed dose distribution of narrow Co-60 beams will enable the determination of volume-averaging correction factor for different detectors.

- Analysis of absorbed dose profiles measured with different detectors will provide the data necessary to recommend suitable detectors for dose profile measurements in non-reference geometry.

## 1.1. Overview of the previous research

In previous research, field output factors and detector-specific correction factors have been determined by Monte Carlo (MC) simulations [15–21], using measured data acquired by different detectors [12,14,22–31], analytically [32,33], or some combination of these methods. [13,17,24]

Nowadays, an increasing number of investigations in the field is based on Monte Carlo simulations to determine various physical quantities which affect absorbed dose to quantify detector-specific perturbations.[16–18,20,34,35] Monte Carlo simulations of particle transport follow discrete steps in the process of interactions with matter using a random number to sample from possible interactions based on probability density functions. They have been giving consistent results throughout different studies and are considered reference techniques for calculating dosimetry quantities. EGSnrc and PENELOPE code have been used for modelling different detectors in narrow photon beams used by Gamma Knife for reference dosimetry both in parallel and perpendicular orientation.[18] Additionally, detectors were modelled inside three different spherical phantoms: Solid Water (Elekta, Stockholm), Acrylonitrile Butadiene Styrene (ABS, Elekta, Stockholm) and liquid water. Detector-specific correction factors for all investigated detectors were within 3% of the reference (MC) value and all had the smallest correction in a liquid water phantom and parallel orientation. Similar Monte Carlo studies support these conclusions.[15]

Furthermore, GAFChromic EBT3 films and diamond detectors were used to validate penEasy Monte Carlo code results. The relative dose profiles along the X and Z axis, for each investigated collimator size and field output factors, have been investigated and compared against the values acquired with the diamond detector. Results were in good agreement with the Monte Carlo simulation.[17] The maximum difference in OF was 2.1% for the 4 mm collimator. The results of the EBT3 dosimetry and penEasy calculation were in excellent agreement. The difference was 0.4% for the 8 mm, and 0.7% for the 4 mm collimator.

Likewise, field output factors and detector-specific correction factors were investigated for a range of different detectors using PEGASOS, a Monte Carlo system based on the PENELOPE code.[36] The liquid ionization chamber (V=1.71 mm$^3$) had a correction factor close to unity for all beams. Six air-vented ionization chambers (volume from 15.71 mm$^3$ to 23.75 mm$^3$) yield

detector-specific correction factors larger than 1.3. A large correction is related to volume-averaging due to the size of the detector's effective volumes and thus are not recommended for dosimetry of Gamma Knife's photon beams. Investigated silicon diode detectors had correction of field output factors between 0.95 and 1.0 mainly contributed to the non-tissue equivalence of the detector. Using the Monte Carlo chain technique, it is possible to determine each detector-specific perturbation inside the photon beam. It has been shown that volume-averaging has a dominant contribution to overall correction for most of the studied detectors.[37]

Experimental methods of determination of field output factors and detector–specific correction factors are performed with various detectors. [8,12–14,17,22,24,37–39] Field output factors are determined using detectors that can be considered perturbation-free (e.g. Exradin W1/W2, EBT3, etc.), and field output factors of studied detectors are compared in a way that the detector's specific correction is determined.

Air-vented ionization chambers are used in radiation dosimetry due to their high sensitivity, dose rate independence, low directional independence, and abundance of dosimetry data for these detectors. [8,13,33,37,40] However, in small photon fields, they have displayed a reduction in sensitivity, perturbation of secondary electron fluence, lower spatial resolution, and larger volume-averaging effect.[13] Detector-specific correction factors for some ionization chambers can be larger than 1.300 and thus are not recommended for small photon field dosimetry. [14] Recently developed small-volume ionization chambers have an improved spatial resolution but require corrections up to 1.050. [14]

Diode detectors are used in small photon field dosimetry due to higher sensitivity and better spatial resolution than ionization chambers but have some disadvantages such as dependence of response on dose rate, energy, and direction.[33] It is known that silicon diode detectors overrespond due to low-energy scattered photons.[1,13,14,29] Depending on the size and design, differences in detector-specific field output factors and field output factors from the reference values can be as large as 10% in small fields.[14,23,41]

Radiochromic film has an excellent spatial resolution. It is considered tissue equivalent and shows minimal directional dependence. [17,42,43] It is widely considered a perturbation-free detector. Field output factors determined using this type of detector show excellent

agreement with Monte Carlo simulations.[17,24,26,30] A disadvantage of radiochromic film is its long saturation time (more than 48 hours), lower signal-to-noise ratio (SNR), and demanding postirradiation processing.

Diamond detectors are solid-state detectors whose effective volume is made of natural or synthetic diamond. They are water equivalent and suitable for field output factors determination and dose profile measurements due to their small size, high response, and low directional independence.[12,13,29] Field output factors and detector-specific correction factors determined with a diamond detector have shown a discrepancy with Monte Carlo simulation data of 1.5% and 0.2% for 4 and 8 mm field sizes, respectively.[44]

Plastic scintillator detectors (PSD) are a new type of detector with attractive properties like water equivalency, high spatial resolution, energy and dose rate independence, and linear dose response. The main disadvantage of PSDs is the production of Cherenkov light which contaminates the main signal. Research with PSDs on Gamma Knife has been very limited so far.[45]

Researchers also use a range of different detectors, some of which have not been stated so far (e.g. alanine, TLDs, MOSFETs, etc.). In general, handling these detectors can be challenging, and they may have less desired properties (e.g., large DSCF, instability, directional dependence, etc.).[12,13,46]

Finally, different mathematical tools are used to model the response of the detector and correct the perturbations e.g., using detectors of different sizes and extrapolating data to zero (point) size, determining the convolution kernel of detectors response, characterizing the influence of the physical properties of the detector, correcting for angular dependence etc.[13,33,37,40]

Generally, according to recent literature, more studies of detector-specific correction factors and field output factors of Gamma Knife beams are based on Monte Carlo simulations than the experimental approach, which may indicate the direction of research in small photon field dosimetry. Some of the problems with the lack of Monte Carlo data come from the complex geometry of the Gamma Knife collimating system. With the advances in computing power, newer simulations tend to be more detailed and accurate. So far, an estimate of volume-

averaging of Co-60 beams used by Gamma Knife has been done once by printing the organic PSD detector in the shape of individual voxels.[47] Although ingenious, this solution is impractical since it requires experience and equipment for high-precision 3D printing. Moreover, such detectors are not standardized in design or response and lack an adequate research base. With this in mind, investigation of the behaviour of the detectors in small photon fields is an ongoing process.

## 1.2. Outline of the thesis

The thesis is based on three goals; the determination of field output factors and volume-averaging correction factors for different detectors commonly used for small field dosimetry, coupled with dose profile measurements of Gamma Knife's narrow photon beams in non-reference geometry.

In Chapter 1 "Introduction and Motivation", a brief historical development and overview of the status of small photon field dosimetry is presented. Special emphasis was given to the field output factor determination as well as the current knowledge overview of the behaviour and performance of different detectors in small photon fields. The three hypotheses and subsequent objectives are stated.

In Chapter 2 the physics of small photon field dosimetry is introduced, and the main problems are discussed. The focus is on the main effects such as loss of charged particle equilibrium, partial source occlusion and volume-averaging of the measured signal. Since these problems are not exclusive to the dosimetry of Gamma Knife's narrow photon beam, they are discussed as general problems. The second chapter was finished with the concepts and formalism introduced by IAEA TRS-483 CoP, which will be followed through this dissertation.

Research methods and materials are presented in Chapter 3. A Gamma Knife Icon device used for Stereotactic radiosurgery is introduced. The design and capabilities of this device are discussed. Next, the list of detectors that are used in this research, as well as their design, is presented. The detector's capabilities and physical working principles are explained in more detail. For the calculation of the volume-averaging correction factors, a formalism of an ellipsoid absorbed dose model is introduced. At the end, statistical methods used for the uncertainty analysis are presented.

The experimental setup for field output factor and dose profile determination is presented in Chapter 4. Volume-averaging correction factor calculated using the ellipsoid absorbed dose model is explained along with the main characteristics and problems with the Gamma Knife's dose profiles determination.

In Chapter 5., field output factors, volume-averaging correction factors and dose profile measurements along with the results of uncertainty analysis are presented and discussed.

At the end, in Chapter 6., the main points of this research are summarized and concluded.

In Appendix A, schematics used for modelling the ionization chambers for volume-averaging calculations are presented. These schematics are provided by the vendor, PTW Freiburg and IBA Dosimetry.

Finally, in Appendix B, a MATLAB code for volume-averaging determination is provided. The MATLAB code can be used and shared by other researchers without any limitations.

# 2. Physics of a small field dosimetry

Dosimetry of broad high-energy photon beams used in radiotherapy is simplified by the fact that a large part of an absorbed dose distribution can be considered as a region where the requirement on charge particle equilibrium (CPE) is fulfilled (Fano's theorem). Therefore, measurements in such regions are well-established and accurate.[2,8,13,48] Small photon fields differ from broad beams in important dosimetry properties, named and explained in the next chapter, making most of the commonly used detectors large relative to the radiation field size.[10] Dosimetry of such fields refers to the measurements and characterization of an absorbed dose delivered by the photon fields smaller than 3×3 cm$^2$. The dosimetry of a small photon fields is challenging because of the presence of steep dose gradients and the lack of charged particle equilibrium making experimental procedures demanding. In the present chapter, the specific physical aspects of small photon field dosimetry are summarized.

Three physical conditions make a high-energy photon field small, and at least one of them must be fulfilled:

1. There is a loss in the lateral charge particle equilibrium (LCPE) on the beam axis.
2. There is a partial occlusion of the primary photon source on the beam's central axis due to the collimation process.
3. The detector's size is similar or large compared to the beam dimensions.

## 2.1. Charge particle equilibrium

The charge particle equilibrium (CPE) condition is fulfilled when the number of charged particles leaving the volume is equal to the number entering it, both for energy and type of particle. This is an important property since detectors, used for the absorbed dose determination, work under the assumption of the CPE, and the ratio of the absorbed dose to kinetic energy released per unit mass (collision KERMA, $K_C$) $D/K_C$ is used to determine a degree of CPE. When the absorbed dose is equal to collision KERMA in a certain volume, the CPE condition is fulfilled. Lateral charge particle equilibrium range $r_{LCPE}$ is the minimum radius of a circular field for which the absorbed dose is equal to collision KERMA at the centre of a field. If the half-width (radius) of a beam is smaller than the maximum range of secondary electrons there will be a loss of lateral charge particle equilibrium. Violation of the CPE creates difficulty in the accurate determination of an absorbed dose-to-water for non-water equivalent material.[10,19,49] A violation of LCPE in narrow photon beams is illustrated in Figure 1. b).
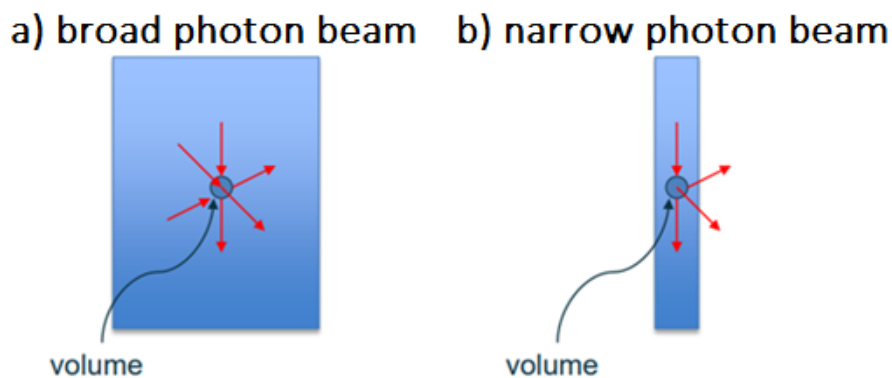


Figure 1.  Charge particle equilibrium in a) broad photon beam, and b) loss of lateral charge particle equilibrium in narrow photon beam. Red arrows represent secondary electrons entering and leaving the volume.

This condition has been quantified using Monte Carlo by evaluating the necessary beam radius in centimetres for different energies to achieve CPE at the beam axis (Figure 2.) and is expressed in terms of a tissue–phantom ratio (TPR) for a 10×10 cm$^2$ field as:[10]

$$r_{LCPE} = 8.369 \cdot TPR_{20,10} - 4.382 \qquad \textbf{2.1}$$

Where $TPR_{20,10}$ is the ratio of an absorbed dose at depth 20 cm and 10 cm. With the increase in the energy of a beam, the radius necessary for achieving LCPE also increases due to the larger mean energy of secondary electrons and as a result more penetrating power. This dependence is illustrated in Figure 2. for different photon beams.
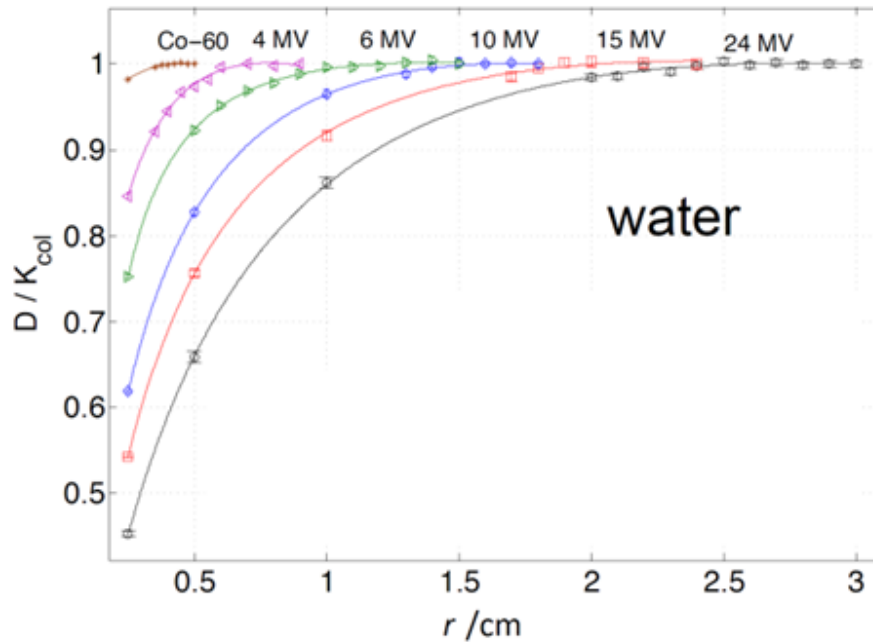


Figure 2. Ratios of dose-to-water to water-collision-kerma calculated by Monte Carlo. The data is plotted as a function of the radius of a narrow photon beam.[10]

For accurate dosimetry of small fields, for a given beam quality, the distance from the detector's outer boundary to the radiation field edge must be smaller than $r_{LCPE}$. This will ensure charged particle equilibrium inside the detector's effective volume because any electron that left the volume will be replenished by an electron produced outside of the volume.

## 2.2. Partial source occlusion

A partial source occlusion is created by the collimator which shields part of the finite primary photon source. This is illustrated in Figure 3., and it becomes important when the field is comparable in size with the primary photon source i.e. when the size of the radiation beam is equal to or less than the full width at half maximum (FWHM) of the emission spectra emitted by the source.
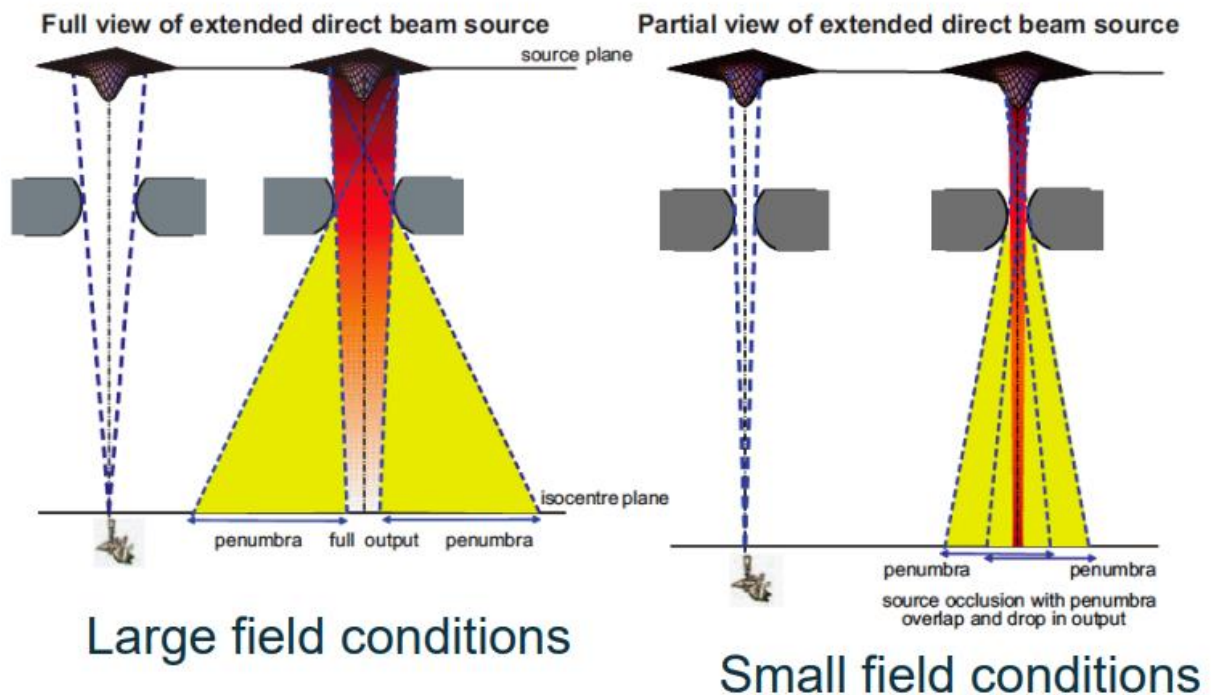


Figure 3. Schematic illustration of a partial source occlusion effect. [49] Note: Distance from source to the isocentre plane is the same in both cases.

This effect changes the emission spectrum, and it is a cause of high-dose gradients which can have a significant effect on the detector's response.[10,49,50] Since the source size is in general smaller than 5 mm, and LCPE begins at the same beam radius (Figure 2.), both loss of charged particle equilibrium and partial source occlusion appeared for the beams with a radius smaller than 5 mm. These effects result in the lower beam output and it is the main reason why field output factors decrease rapidly with a reduction in beam dimensions.[2] This drop becomes more pronounced with the increase of the photon beam energy or as the density of a medium decreases due to the increase in range of the secondary electron .[10,19,49–51] Effects of the partial source occlusion can be summarized as overlapping of penumbras, reduction of a central-axis

dose which decreases the beam output, and finally, apparent field widening causing a mismatch between true field size (FWHM) and nominal field size determined by collimator settings.[50] The effects of the partial source occlusion are illustrated in Figure 4.
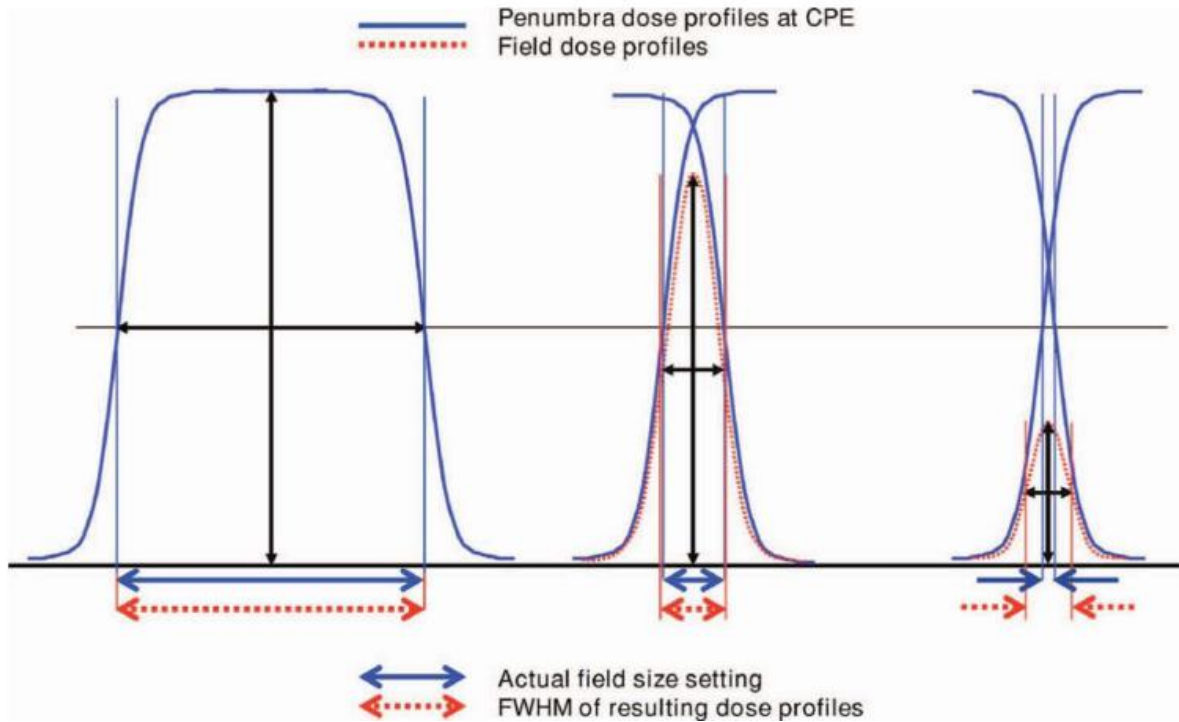


Figure 4. Effects of overlapping penumbras on the FWHM of the lateral beam profile for small fields illustrating the apparent field widening compared to the collimator settings and reduction of the central axis dose.[9,10]

Although an important effect in small photon field dosimetry, the effect of overlapping penumbras is negligible on Gamma Knife since Co-60 sources are packed as small cylinders with a diameter of 1 mm, while the smallest beam diameter is 4 mm.

## 2.3. Volume-averaging

Volume-averaging of a measured response is another problem in small photon field dosimetry. A detector produces a response that is proportional to the mean absorbed dose over its effective volume and the response is affected by the homogeneity of the absorbed dose distribution over the volume of the detector. As a result, the response is averaged over the volume of the detector. [10]

Volume-averaging leads to two distinct consequences:

1. The absorbed dose at the centre of a small field is underestimated.
2. The penumbra is flattened i.e. the field appears to be larger than it is.

An illustration of the volume-averaging problem is shown in Figure 5. with a schematic representation of the volume-averaging effect in the determination of the Gaussian beam profile using a detector 5 mm in length. Both underestimation of the absorbed dose at the central axes of the beam and flattening of the penumbra is visible. This effect is the subject of research primarily concentrated on X-ray beams produced by linear accelerators, CyberKnifes, and Tomotherapy units [10,23,32,50–53], while research regarding volume-averaging in narrow Co-60 beams of Gamma Knife is very limited.[47,54] It has been shown that volume averaging, besides the size of the detector's effective volume, depends on the shape of that volume as well. More compact detectors with a lower length-to-diameter ratio (l/d) will have lower volume averaging correction for the same size of an effective volume.[55]
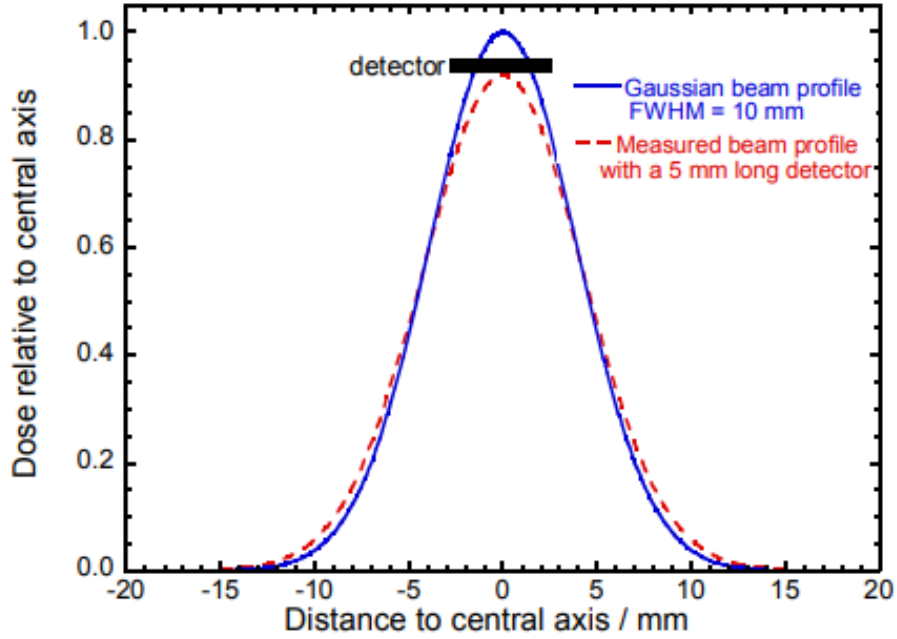
Figure 5. Schematic representation of volume-averaging effect one dimension. The blue curve is a Gaussian dose profile, the red dashed curve represents what a detector of 5 mm length measures.[50]

In practice, it is impossible to eliminate volume-averaging. For field output factors determination, volume-averaging will be one of the limiting factors for the choice of detectors, especially in narrow photon beams of Gamma Knife. The detectors should be chosen in a way that its volume-averaging correction factor $(k_{vol})_{Q_{clin}}^{f_{clin}}$, for the beam quality $Q_{clin}$, in a clinical (clin) field of interest $f_{clin}$, is such that it is limited by $0.95 \leq (k_{vol})_{Q_{clin}}^{f_{clin}} \leq 1.05$.[10] The volume-averaging correction factor can be calculated using the Kawachi formula[53] by integrating dose profiles over the detector's area A perpendicular to the beam axis:

$$(k_{vol})_{Q_{msr,clin}}^{f_{msr,clin}} = \frac{\iint_A w(x,y)dxdy}{\iint_A w(x,y)OAR(x,y)dxdy} \qquad \textbf{2.2}$$

where, $x$ and $y$ are the coordinates of the axes orthogonal to the beam's central axis, $w(x,y)$ is the weighting function specific to the detector's geometry and represents the extension of the air cavity along the beam axis as a function of the beam lateral coordinates. In the Equation 2.2. msr and clin stand for machine-specific reference field and clinical field, respectively. For

most ionization chambers, this can be approximated with unity.[48] Finally, $OAR(x, y)$ is the off-axis ratio or 2D lateral beam profile at the measuring depth normalized to the central axis.

The Equation 2.2. can be used to determine volume-averaging which will affect the detector's response in dosimetry of narrow X-ray beams. In these devices the beam is incident perpendicular to the detector surface, therefore, to determine volume-averaging one must integrate the field over the detector's surface perpendicular to the beam's central axis. However, on Gamma Knife Perfexion there are 192 beams converging to an isocentre as illustrated in Figure 6. The ellipsoid geometry of the Gamma Knife absorbed dose distribution complicates the calculation of the volume-averaging correction factor and it is the main reason why research of detector's volume-averaging in Gamma Knife's narrow photon beams is limited even when it comes to the Monte Carlo simulations. However, if done realistically, Monte Carlo simulations should be the best tool for volume averaging correction factor estimations.



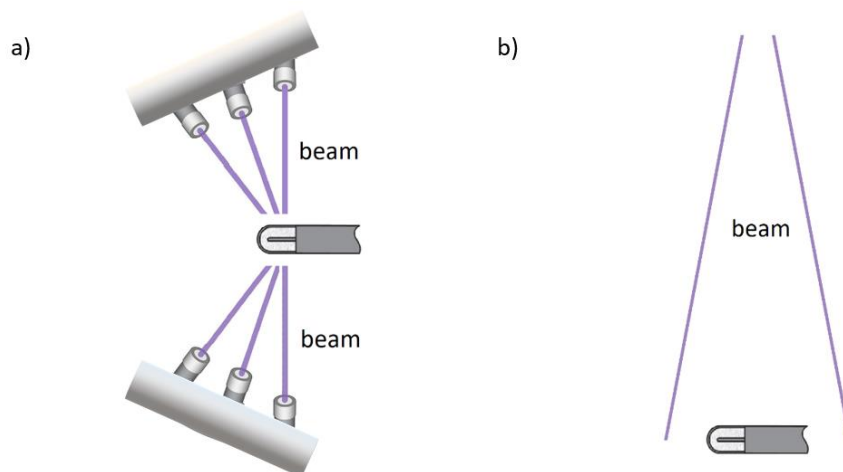Figure 6. A schematic representation of radiation field for a) Gamma Knife Perfexion, and b) LINAC, CyberKnife, or Tomotherapy unit.

Due to the unique geometry of Gamma Knife's collimator system, Kawachi formalism must be modified from 2D to 3D to be applicable for absorbed dose distribution of Gamma Knife's narrow photon beams, and integration must be performed over the detector's effective volume, in a way:

$$(k_{vol})_{Q_{clin}}^{f_{clin}} = \frac{\iiint_V w(x,y,z)dxdydz}{\iiint_V w(x,y,z)OAR(x,y,z)dxdydz} \qquad \textbf{2.3}$$

The effective volume of most available detectors is cylindrical. Therefore, integration was performed in the cylindrical coordinate system, with the assumption that $w(x,y,z) = 1$:

$$(k_{vol})_{Q_{clin}}^{f_{clin}} = \frac{\iiint_V sdsd\varphi dz}{\iiint_V OAR(s,\varphi,z)sdsd\varphi dz} = \frac{V}{\iiint_V OAR(s,\varphi,z)sdsd\varphi dz} \qquad \textbf{2.4}$$

where V is detector's effective volume and s, φ and z are the coordinates in cylindrical coordinate system. Neglecting the weighting function can be justified by the fact that its impact on volume-averaging correction for a 2D case is approximately 0.1 %.[10]

The volume-averaging correction factor $k_{vol}$ is used for a conversion of a mean dose $D_{mean}$ determined by a detector to a point dose:

$$D_P = D_{mean} \cdot (k_{vol})_{Q_{clin}}^{f_{clin}} \qquad \textbf{2.5}$$

if the geometry of the detector is known, as well as the relative dose distribution over the detector's volume the volume-averaging correction factor can be calculated as:

$$(k_{vol})_{Q_{clin}}^{f_{clin}} = \frac{D_p}{D_{mean}} = \frac{D_p}{\frac{1}{V}\int D(\vec{r})d^3r} = \frac{V}{\int \left(\frac{D(\vec{r})}{D_p}\right)d^3r} = \frac{V}{\int D_{rel}(\vec{r})d^3r} \qquad \textbf{2.6}$$

Using Equation 2.6. and by knowing the shape and the value of the detector's effective volume V and a normalized absorbed dose distribution over that volume $D_{rel}(\vec{r})$, a volume-averaging correction factor for the detector can be calculated.

## 2.4. Concepts and formalism in small photon field dosimetry

In this section, concepts and formalism for reference and relative dosimetry of narrow Co-60 beams are presented according to the IAEA TRS-483 CoP.[11] Reference dosimetry refers to a determination of an absorbed dose in water with an ionization chamber for which the charge is measured in the beam of the user's institution. The reference conditions used in the calibration laboratory must be reproduced, and influence quantities are measured at the time of data acquisition and the measured detector's response is corrected accordingly. In the clinical environment, various measurements are performed under non-reference conditions. These measurements are called relative.[56] For irradiation units that cannot attain a reference field, a machine-specific reference field is introduced. The machine-specific reference field has dimensions as close as possible to the conventional reference field and extends at least an $r_{LCPE}$ distance from the outer boundary of the ionization chamber.[10] That is, the size of the detector $d$, and the field size FWHM must fulfil the condition:

$$FWHM_{msr} \geq 2r_{LCPE} + d \qquad \textbf{2.7}$$

which is illustrated in Figure 7. where the yellow area represents the range of secondary electrons, and the blue is a square field over the detector's effective area.
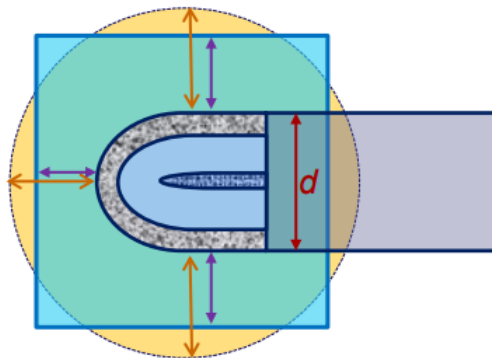


Figure 7. The illustration of a range of secondary electrons leaving the ionization chamber (yellow) and a small field superposed on the ionization chamber (blue). Charge particle equilibrium is violated.[1]

In the majority of cases, the ionization chamber calibration factor in terms of an absorbed dose to water $N_{D,w,Q_0}^{f_{ref}}$ is determined in a 10×10 cm$^2$ reference field $f_{ref}$ with beam quality $Q_0$. For Gamma Knife such a reference field is impossible to achieve and therefore a machine-specific reference field $f_{msr}$ (msr) is used which is the largest 16 mm field. In such conditions, the absolute dose to water $D_{w,Q_{msr}}^{f_{msr}}$ is determined as:

$$D_{w,Q_{msr}}^{f_{msr}} = M_{Q_{msr}}^{f_{msr}} \cdot N_{D,w,Q_0}^{f_{ref}} \cdot k_{Q_{msr},Q_0}^{f_{msr},f_{ref}} \qquad \text{2.8}$$

where $M_{Q_{msr}}^{f_{msr}}$ is the reading of the ionization chamber in a machine-specific reference field corrected for pressure, temperature, incomplete charge collection, polarity humidity etc. The beam quality correction factor $k_{Q_{msr},Q_0}^{f_{msr},f_{ref}}$ accounts for the difference between the response of the ionization chamber in the reference field $f_{ref}$ with beam quality $Q_0$, and a machine-specific reference field $f_{msr}$ with beam quality $Q_{msr}$, and it is defined as a ratio of ionization chamber's calibration coefficients in a machine-specific reference field and conventional reference field (Equation 2.9.).[11]

$$k_{Q_{msr},Q_0}^{f_{msr},f_{ref}} = \frac{N_{D,w,Q_{msr}}^{f_{msr}}}{N_{D,w,Q_0}^{f_{ref}}} = \frac{D_{w,Q_{msr}}^{f_{msr}} / M_{Q_{msr}}^{f_{msr}}}{D_{w,Q_0}^{f_{ref}} / M_{Q_0}^{f_{ref}}} \qquad \text{2.9}$$

For most of the ionization chambers, $Q_0$ is the beam quality of the Co-60 beams. The beam quality correction factor is usually calculated using Monte Carlo simulations.[10] For some ionization chambers that can be used for reference dosimetry of the Gamma Knife Icon beams, they are calculated and listed in IAEA TRS-483 CoP.

Field output factors $\Omega_{Q_{clin},Q_{msr}}^{f_{clin},f_{msr}}$ are measures of the difference of an absorbed dose in clinical fields compared to the machine-specific reference field. They are defined as a ratio of the absorbed dose to water in the clinical field $f_{clin}$ with beam quality $Q_{clin}$ the absorbed dose to water in machine-specific reference field $f_{msr}$ with beam quality $Q_{msr}$ (Equation 2.10.)

$$\Omega^{f_{clin},f_{msr}}_{Q_{clin},Q_{msr}} = \frac{D^{f_{clin}}_{w,Q_{clin}}}{D^{f_{msr}}_{w,Q_{msr}}} \qquad\qquad \textbf{2.10}$$

To determine an absorbed dose, a response is measured in the form of an electric charge produced in the detector's effective volume. In the broad beams, a collected charge is proportional to the absorbed dose. However, in small fields due to the nonequilibrium conditions, the detector's response ratio must be multiplied by the detector-specific correction factor $k^{f_{clin},f_{msr}}_{Q_{clin},Q_{msr}}$ to determine field output factors (Equation 2.11.).

$$\Omega^{f_{clin},f_{msr}}_{Q_{clin},Q_{msr}} = \frac{M^{f_{clin}}_{Q_{clin}}}{M^{f_{msr}}_{Q_{msr}}} \cdot k^{f_{clin},f_{msr}}_{Q_{clin},Q_{msr}} \qquad\qquad \textbf{2.11}$$

The detector-specific correction factor can be determined experimentally by measurements or calculated using Monte Carlo. This correction factor is specific to a given detector and must be determined for each field size, energy, and spectral distribution. For some detectors that are very small and have an energy-independent response, like radiochromic films, liquid ionization chambers, or an organic scintillator; the detector-specific correction factor is very close to unity.[2,8,10,29,49,51] The detector-specific correction factor is a product of four different perturbations in the small fields: ratios of water-to-detector-medium stopping power in clinical and machine-specific reference fields $(s_{w,det})^{Q_{clin}}_{Q_{msr}}$, volume-averaging correction factor ratios $(p_{vol})^{Q_{clin}}_{Q_{msr}}$, ratios due to the fluence perturbations $(p_f)^{Q_{clin}}_{Q_{msr}}$, and, finally, ratios of spectral dependence of photon energy absorption inside the detector medium in clinical and machine specific reference field $(p_{spec})^{Q_{clin}}_{Q_{msr}}$.[14]

$$k^{f_{clin},f_{msr}}_{Q_{clin},Q_{msr}} = \frac{(s_{w,det})_{Q_{clin}}}{(s_{w,det})_{Q_{msr}}} \cdot (p_{vol})^{Q_{clin}}_{Q_{msr}} \cdot (p_f)^{Q_{clin}}_{Q_{msr}} \cdot (p_{spec})^{Q_{clin}}_{Q_{msr}} \qquad \textbf{2.12}$$

It has been shown that fluctuation of stopping power with beam size is negligible e.g. changing the beam dimensions from 10×10 cm$^2$ to 0.5×0.5 cm$^2$ the stopping power changes only by 0.3%.[14,21] Therefore, Equation 2.12. can be approximated as:

$$k_{Q_{clin},Q_{msr}}^{f_{clin},f_{msr}} \approx (p_{vol})_{Q_{msr}}^{Q_{clin}} \cdot (p_f)_{Q_{msr}}^{Q_{clin}} \cdot (p_{spec})_{Q_{msr}}^{Q_{clin}} \qquad \textbf{2.13}$$

A summary of formalism for small static photon field dosimetry is presented in Figure 8.
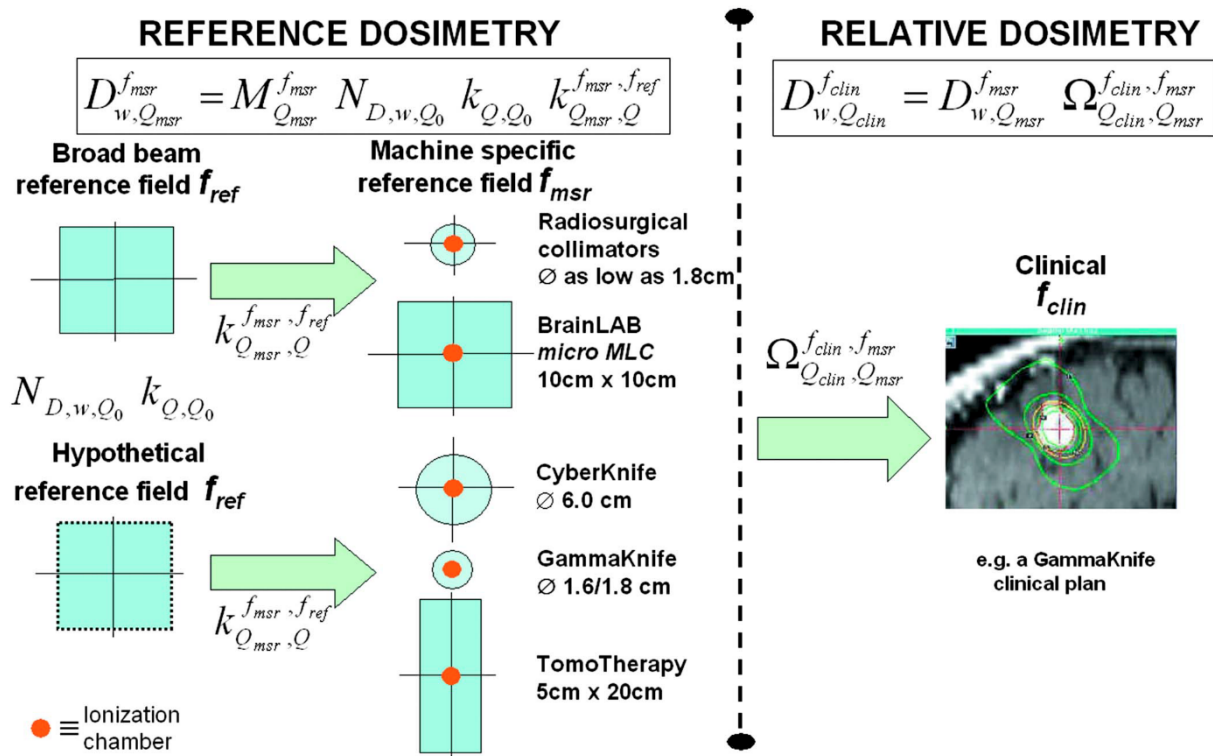


Figure 8.  Schematic overview of the dosimetry of small static fields with reference to machine-specific reference fields according to Alfonso formalism and IAEA TRS-483 CoP.[10,11]

# 3. Research Methods and Materials

## 3.1. Gamma Knife Perfexion - Icon

Leksell Gamma Knife Icon (Elekta, Stockholm, Sweden) is a model of Gamma Knife built on the Perfexion platform with the addition of Cone Beam Computed Tomography (CBCT). This model differs substantially from its predecessor, and it is the first time since Model C that its beam delivery system has been completely redesigned with 192 Co-60 sources arranged in a cone-shaped configuration compared with 201 sources in the hemispherical configuration in previous models (Figure 9.).
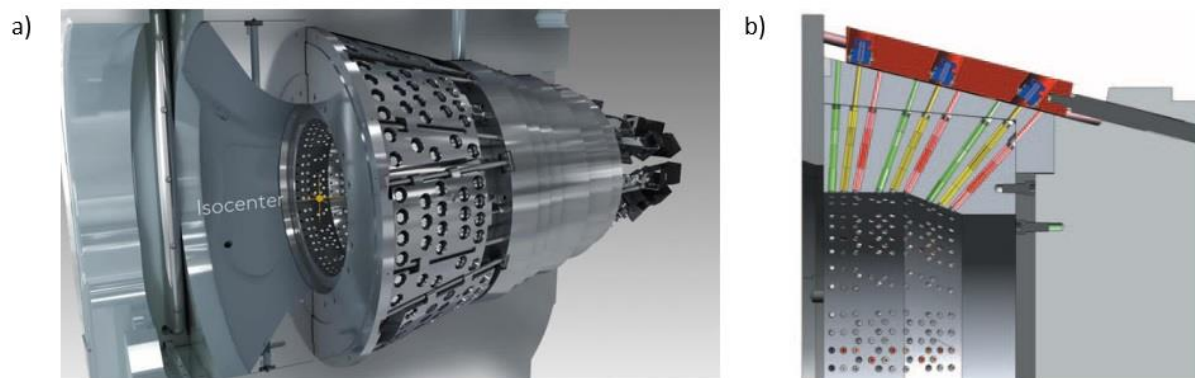


Figure 9. a) Collimator system of Gamma Knife Perfexion and b) its cross-section.

Radionuclide Co-60 decays with $\beta^-$ decay into Ni-60 with the emission of two photons 1.17 MeV and 1.33 MeV. Since the probability for the emission of each photon is approximately equal, the mean energy of Co-60 decay is 1.25 MeV. All photons are focused to a single point - isocentre. The total absorbed dose is equal to the sum of absorbed doses delivered by each beam allowing dose escalation at the isocentre (up to 100 Gy) creating strict requirements on the geometrical and dosimetry accuracy. LGK absorbed dose distribution is ellipsoidal in shape due to the geometry of the collimating system.

On Gamma Knife Perfexion there are three available collimators: 16 mm, 8 mm, and 4 mm. The collimator array is made of a single 120 mm tick tungsten divided into eight identical regions, every with 72 collimators (24 for each of the 3 available collimators). Nominal fields are named 16 mm, 8 mm and 4 mm due to the size of the projection of a beam diameter through a single collimator hole to the isocentre. Gamma Knife absorbed dose distributions are superposition of 192 beams and therefore the actual field size is larger. Different field sizes are created by the automated sliding of Co-60 sources over the top of the collimator system (Figure 9b.).[57]

Depth dose modelling is performed with the new TMR 10 water-based dose calculation algorithm (Elekta Instruments AB, Stockholm, Sweden).[58] TMR 10 calculates the absorbed dose at a point using two different attenuation parameters; first for the attenuation of the primary photon fluence and the second term where the distance from the focal point is multiplied by the virtual attenuation coefficient of the particular beam. In clinical practice, dose distributions often have to be multicentric and irregular in shape.
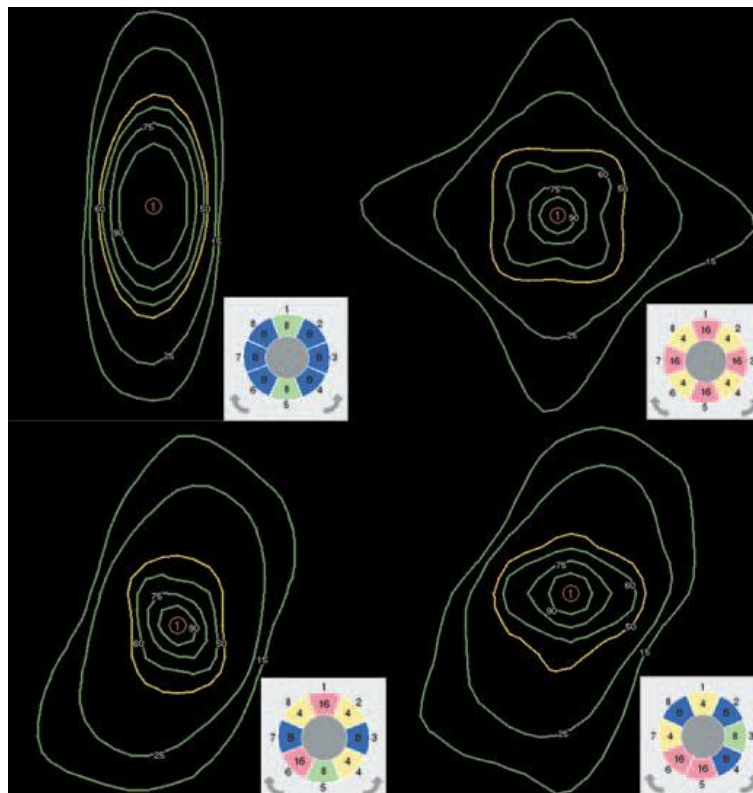


Figure 10. Examples of isodose shapes from single isocentre using composite shot features.[59]

Figure 11. Leksell Gamma Knife Icon.[3]

## 3.2. Detectors

Detectors that were used for the determination of field output factors, volume-averaging correction factors and dose profile measurements are presented in Table 1.[60–66]

Listed air–vented ionization chambers range in size of their effective volumes from 3 mm$^3$ to 125 mm$^3$. Some of the ionization chambers whose dosimetry properties have been investigated in this research do not have detector-specific correction factors in IAEA TRS - 483 CoP. PinPoint and PinPoint 3D have detector–specific correction factors listed in IAEA TRS - 483 CoP, except for the smallest 4 mm field in which they are not recommended for use due to the size of their effective volume (Table 1.).[10]

Diodes are a p–type semiconductor detectors with their effective volumes significantly smaller than the ones from air-vented ionization chambers ranging from 0.02 mm$^3$ to 0.19 mm$^3$. Smaller volumes of diode detectors will result in a smaller volume-averaging correction factor making them appropriate for dose profile measurements in small photon fields. Diode detectors are intended for relative dosimetry of Gamma Knife's narrow photon beams with only two detectors (Diode P and E) listed in IAEA TRS - 483 CoP.

The diamond detector is made from a synthetic diamond with correction factors for Gamma Knife Perfexion available in the literature.[10] Out of all active types of detectors, it has the smallest effective volume. This detector was specially designed for the relative dosimetry of narrow photon beams.

Plastic scintillator detectors (PSD) are considered perturbation free due to their tissue equivalence and can be used for reference and relative dosimetry.[66] They are active detectors requiring correction for Cherenkov radiation. In this study, two plastic scintillator detectors are modelled in the Gamma Knife Perfexion narrow photon beams to determine its volume-averaging correction factors. Since they are not used in field output factor determination of dose profile measurements, the physics of plastic scintillator detectors and their behaviour in narrow Co-60 photon beams is omitted. No detector-specific correction factors are listed in IAEA TRS-483 CoP for these types of detectors.[10]

EBT3 film is a well-established detector for reference and relative dosimetry with correction factors approximated with unity. Radiochromic film is a passive detector requiring calibration of optical density against the absorbed dose.

In the present section, the physics of the listed detector types will be explained in more detail with emphasis on their advantages and disadvantages when it comes to small field dosimetry.

| Name | Type | Manufacturer | Effective volume / mm³ | Used in research of: | | | Gamma Knife Perfexion: | |
| :---: | :---: | :---: | :---: | :---: | :---: | :---: | :---: | :---: |
| | | | | OFs | $k_{vol}$ | Dose profiles | Dosimetry type: | DSCF available in IAEA TRS-483 CoP: |
| Semiflex T31010 | Air – vented ion. chamber | PTW - Freiburg | 125 | Yes | Yes | No | Reference | Yes |
| Semiflex 3D T31021 | Air – vented ion. chamber | PTW - Freiburg | 70 | Yes | Yes | No | Relative | No |
| PinPoint T31014 | Air – vented ion. chamber | PTW – Freiburg | 15 | Yes | Yes | Yes | Relative | Yes, except for the 4 mm field |
| PinPoint 3D T31016 | Air – vented ion. chamber | PTW - Freiburg | 16 | Yes | Yes | Yes | Reference & Relative | Yes, except for the 4 mm field |
| RAZOR chamber | Air – vented ion. chamber | IBA Schwarzenbruck | 10 | Yes | Yes | Yes | Relative | No |
| RAZOR nano chamber | Air – vented ion. chamber | IBA Schwarzenbruck | 3 | Yes | No | Yes | Relative | No |
| IBA CC04 | Air – vented ion. chamber | IBA Schwarzenbruck | 40 | Yes | Yes | Yes | Reference | Yes |
| Diode P T60016 | p – type semiconductor | PTW - Freiburg | 0.030 | Yes | Yes | Yes | Relative | Yes |
| Diode E T60017 | p – type semiconductor | PTW - Freiburg | 0.030 | Yes | Yes | Yes | Relative | Yes |
| EFD 3G-pSi | p – type semiconductor | IBA Schwarzenbruck | 0.190 | No | Yes | Yes | Relative | No |
| RAZOR diode | p – type semiconductor | IBA Schwarzenbruck | 0.020 | Yes | Yes | Yes | Relative | No |
| EDGE detector | p – type semiconductor | Sun Nuclear Corp. | 0.020 | Yes | Yes | No | Relative | No |
| microDiamond T60019 | Synthetic diamond | PTW - Freiburg | 0.004 | Yes | Yes | Yes | Relative | Yes |
| Exradin W2 1x1 | Plastic scintillator | Standard Imaging | 0.785 | No | Yes | No | Reference & Relative | No |
| Exradin W2 1x2 | Plastic scintillator | Standard Imaging | 2.356 | No | Yes | No | Reference & Relative | No |
| EBT3 | Radiochromic films | GAFchromic | / | Yes | No | Yes | Reference & Relative | Approximated with unity |

Table 1. List of the detectors used along their main characteristics.[60,61,63–65,67,68]

## 3.2.1. Ionization chambers

Ionization chambers are established and frequently used for both relative and reference dosimetry in small photon fields. They can be air-vented or filled with nonpolar liquid. They work under the principle of ionization of atoms in a medium placed in an electric field through which incident photon beams pass. They can be cylindrical or plane-parallel in design.
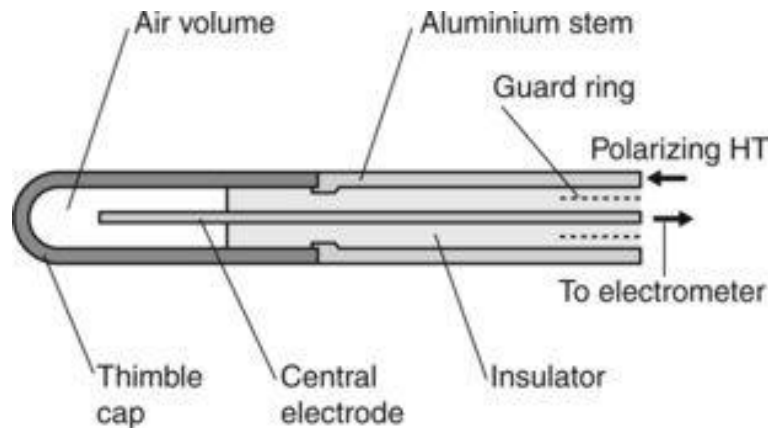


Figure 12. Schematic illustration of a cylindrical ionization chamber. HT stands for High Tension.[69]

A thimble chamber (cylindrical) is the most used type of ionization chamber in narrow photon beam dosimetry. It consists of a central electrode and a cylindrical wall with a spherical or conical end mounted on a cylindrical stem (Figure 12.). When an ionization chamber is placed in the radiation beam, ionization of the medium occurs creating electrons in the walls of a chamber that transverse the air cavity, ionizing the medium inside it. A collected charge can be related to the absorbed dose through a calibration factor typically obtain from the secondary standardised dosimetry laboratory (SSDL). The wall must be thick at least as the range of secondary electrons produced in photon interactions to ensure that all electrons crossing the cavity originated in the wall itself, not surrounding material.[69] However, the chamber's walls will attenuate the photon beam and this attenuation must be appropriately considered when designing chambers. Effective volume can vary from 0.001 cm$^3$ to 10 000 cm$^3$ depending on the purpose of an ionization chamber. Smaller ionization chambers are typically used in medical physics while large ones are used in nuclear and reactor physics. Ionization chambers are characterised by an excellent dose response, dose rate independence, low directional dependence, and an abundance of dosimetry data with these

detectors.[9,13,29] Furthermore, the reading of air-vented ionization chambers must be corrected for the difference in pressure and temperature from the reference conditions in which the chamber was calibrated as

$$k_{Tp} = \frac{(t + 273.15)p_0}{(t_0 + 273.15)p} \qquad \textbf{3.1}$$

where $t$ is temperature in °C and $p$ is pressure in kPa of the air in the cavity of the ionization chamber, and $t_0$ and $p_0$ are the reference values for temperature and pressure i.e., 20 °C and 101.325 kPa. Ionization chambers are known to exhibit the polarity effect which results in the change of an intensity of collected current when the polarity of collecting potential is reversed, and this needs to be appropriately considered.[10,70] Additional effect which may influence the accuracy of collected charge is ion recombination effect. In ionization chambers, two separate ion recombination effects can take place: the recombination of ions formed by separate ionizing particle tracks and recombination of ions formed by a single ionizing track.[10] As with the polarity effect, determined charge with ionization chamber must be corrected for this influence.

So far all of the mentioned effects are influence factors that may affect the accuracy of measurements. Beside this, ionization chambers have several perturbation factors that have an impact on their accuracy in dosimetry of small fields: $p_{wall}$ and $p_{cell}$ are perturbations due to the non-tissue equivalence of wall and central electrode material, $p_{vol}$ is perturbation due to the volume-averaging and $p_{dis}$ is perturbation due to displacement effect. The total perturbation correction factor $p_{tot}$ for air-vented ionization chambers is a product of individual perturbations (Figure 13.). The main problem with these detectors, as it will be shown in this work, is that some of them are too large to be used in a narrow photon beams due to volume-averaging and loss of lateral charged particle equilibrium.[10,51]
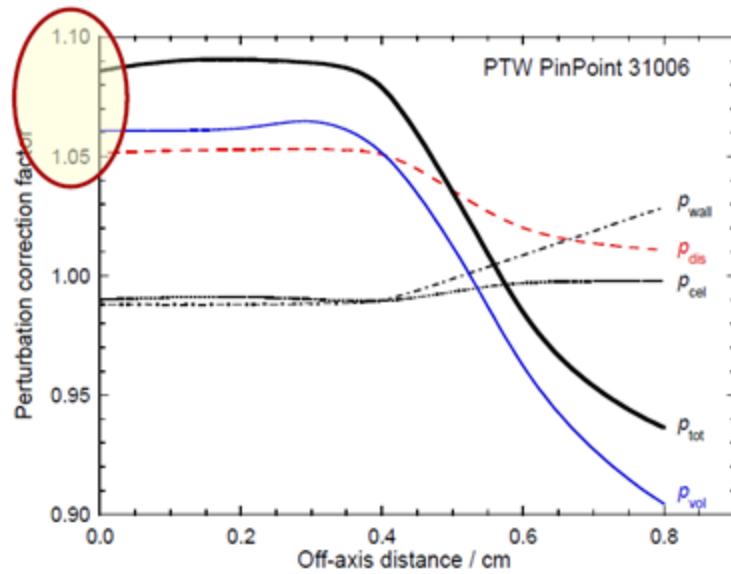
Figure 13. Perturbation correction factors as s function of off-axis distance in small fields for PinPoint T31006 chamber.[71]

The development of ionization chambers with small effective volumes (less than 0.1 cm$^3$) enabled them to be used in the dosimetry of narrow photon beams. It has been shown that although small in volume, these ionization chambers still considerably underestimate field output factors in small fields.[21,29] Some of the physical characteristics of ionization chambers listed in Table 1., are stated in Table 2., and Table 3. for ionization chambers produced by PTW and IBA, respectively.

|  |  | Semiflex T31010 | Semiflex 3D T31021 | PinPoint T31014 | PinPoint 3D T31016 |
|---|---|---|---|---|---|
| Specification | Reference point / mm [a] | 4.5 | 3.45 | 3.4 | 2.4 |
| | Response / nC/Gy [b] | 3.3 | 2 | 0.8 | 0.4 |
| | Chamber voltage / V | 400 | 400 | 400 | 300 |
| Materials and measures | Wall area density / mg/cm$^2$ | 78 | 84 | 85 | 84 |
| | Dimension [c] | Radius 2.75 Length 6.5 | Radius 2.4 Length 4.8 | Radius 1 Length 5 | Radius 1.45 Length 2.9 |
| | Electrode [d] | Al 99.98, 1.1 | Al 99.98, 0.8 | Al 99.98, 0.3 | Al 99.98, 0.6 |
| | Build-up cap | PMMA, 3 mm tick | PMMA, 3 mm tick | PMMA, 3 mm tick | PMMA, 3 mm tick |

Table 2. Physical characteristics of PTW ionization chambers.

[a] Reference point on the chamber's axis, from the tip of a chamber.

[b] Nominal response.

[c] Dimensions in millimetres.

[d] Material, and the diameter of an electrode in millimetres.

|  |  | RAZOR chamber | RAZORnano chamber | CC04 |
|---|---|---|---|---|
| Specification | Reference point / mm [a] | 2.3 | 1.4 | 2.3 |
| | Response / nC/Gy [b] | 0.3 | 0.11 | 1 |
| | Chamber voltage / V | 300 | 300 | 300 |
| Materials and measures | Wall area density / mg/cm$^2$ | 88 | 88 | 70 |
| | Dimension [c] | Radius 1 Length 3.6 | Diameter 2 | Radius 2 Length 3.6 |
| | Electrode [d] | Graphite, 0.55 | Graphite – EDM3, 1 | Shonka (C-552), 1 |

Table 3. Physical characteristics of IBA ionization chambers.

[a] Reference point on the chamber's axis, from the tip of a chamber.

[b] Nominal response.

[c] Dimensions in millimetres.

[d] Material, and the diameter of an electrode in millimetres.

## 3.2.2. Silicon detectors

Semiconductor or diode detectors are commonly used in small-field dosimetry.[29] They are made of silicon in a way that a layer of n-type silicon is brought into contact with p-type silicon. This allows the electrons to drift from the n-region to the p-region creating an intrinsic zone. Incident ionizing radiation liberates electrons from the intrinsic zone to the p-layer generating an electrical current, while positive charge carriers travel in the opposite direction. The produced electrical current is proportional to an absorbed dose. Semiconductor detectors do not require an external bias voltage.[63–65] A schematic representation of the semiconductor detector's working principle is shown in Figure 14.
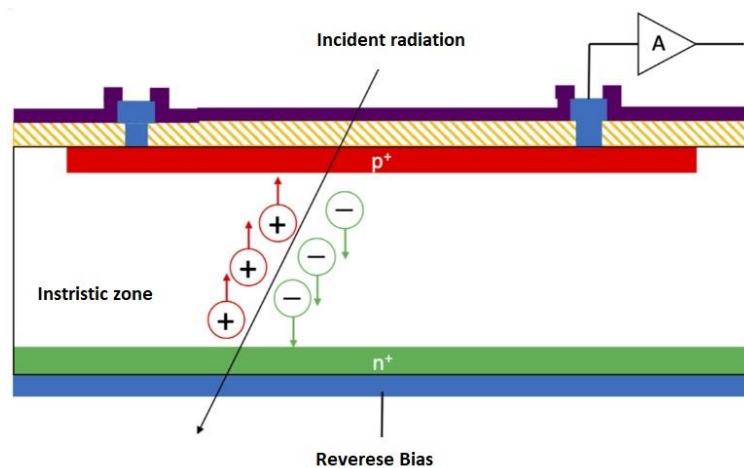


Figure 14. A schematic representation of a semiconductor detector. When traversing through a silicon detector, incoming radiation creates electron-hole pairs along its path. In the presence of an electric field, these charge carriers are separated and start drifting toward the electrodes.[72]

A silicon detector consists of a layered silicon disk placed horizontally or vertically in the protective and/or build-up material depending on the intended application of such a detector (Figure 15.).[63–65]
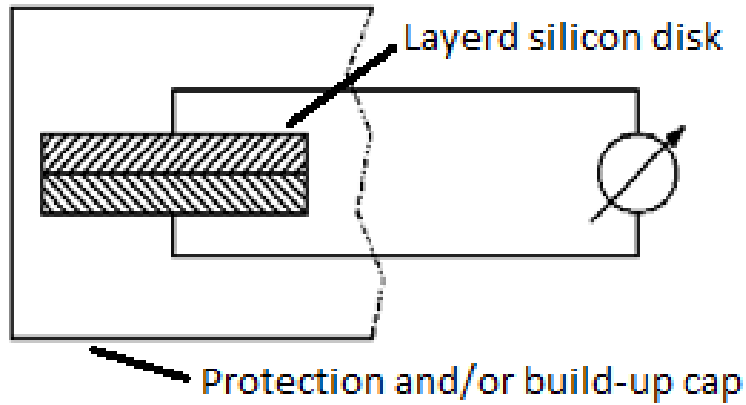
Figure 15. An illustration of a semiconductor detector.[63]

The sensitivity of silicon detectors is larger when compared to an ionization chamber since it requires only 3.6 eV to create an electron-hole pair in silicon compared to the energy required to generate an ion pair in the air (33.97 eV). Therefore, their effective volumes can be significantly smaller, minimizing the volume-averaging effect. The silicon detectors have been widely used in small photon field dosimetry due to their small size, high resolution, and real-time readout.[29] They also have disadvantages such as the dependence on energy, temperature, dose rate, and direction.[14,33,39,41]
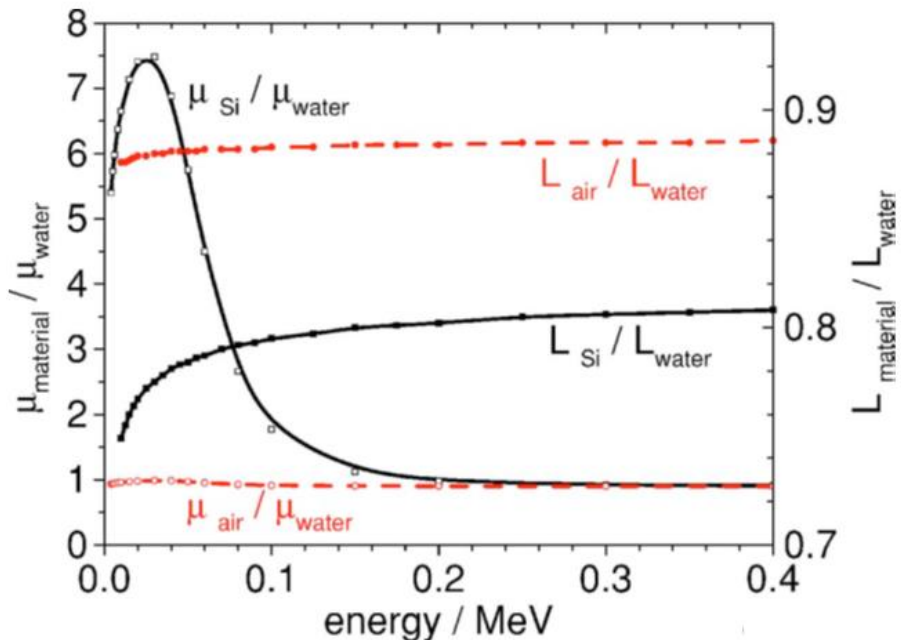


Figure 16. Energy absorption coefficient ratios (left y scale) and restricted stopping power ratios (right y scale) for air and silicon relative to the water.[41]

From Figure 16 one can see the main reasons for the difference in response of silicon detectors and ionization chambers. For air, both stopping power and absorption coefficients change only slightly with beam energy resulting in the uniform response of the ionization chambers. By contrast, in silicon, the absorption coefficient is increased almost eight times larger for low photon energies (at approx. 200 keV). Therefore, silicon detectors will overrespond to the low-energy photons. [13,33,39] Consequently, silicon detectors are not recommended for dosimetry in broad photon beam geometry due to a significant number of scattered photons. To resolve for this, shielding of an effective volume for some diode detectors is added. Some of the physical characteristics of a silicon detector listed in Table 1. used for field output determination and dose profile measurements, are stated in Table 4. for PTW detectors, and in Table 5. for IBA and Sun Nuclear detectors.

| | | Diode P T60016 | Diode E T60017 |
|---|---|---|---|
| **Specification** | **Reference point / mm [a]** | 2.42 | 0.77 |
| | **Response / nC/Gy [b]** | 9 | 9 |
| | **Bias voltage / V** | 0 | 0 |
| **Materials and measures** | **Window area density / mg/cm$^2$** | 250 | 140 |
| | **Dimensions** | Radius 0.56 mm | Radius 0.56 mm |
| | | Tick 30 μm | Tick 30 μm |

Table 4. Physical characteristics of PTW semiconductor detectors. Diode P and E have the same design, except Diode P's effective volume is shielded thus it is more suitable for dosimetry involving broad beam geometries.
[a] Reference point on the detector's axis, from the tip of a detector.
[b] Nominal response.

| | | EFD 3G-pSI | RAZOR diode | EDGE detector |
|---|---|---|---|---|
| **Specification** | **Reference point / mm** [a] | 1.2 | 0.8 | 0.3 |
| | **Response / nC/Gy** [b] | 100 | 4.1 | 32 |
| | **Bias voltage / V** | 0 | 0 | 0 |
| **Materials and measures** | **Window area density** | Not stated | Not stated | Not stated |
| | **Dimensions** | Radius 0.8 mm Tick 0.08 mm | Radius 0.3 mm Tick 0.02 mm | 0.8 x 0.8 mm (rectangular) Tick 0.03 mm |

Table 5. Physical characteristics of IBA and Sun Nuclear semiconductor detectors.
[a] Reference point on the chamber's axis, from the tip of a chamber.
[b] Nominal response.

## 3.2.3. Diamond detectors

Diamond detectors are solid-state detectors and their effective volume is built of a natural or synthetic diamond. They have excellent properties such as fast response due to high electron-hole mobility and tissue equivalence because of a low atomic number Z=6 and wide band gap of 5.4 eV. Consequently, they have been used in a field of high-energy physics, nuclear engineering and medical physics.[73] The operating principle is based on the high-resistivity diamond material sandwiched between two metal electrodes (Figure 17.). An external voltage provides an electric field across the device. Mobile charges produced by absorbed radiation drift in this electric field and generate a current in the external circuit.
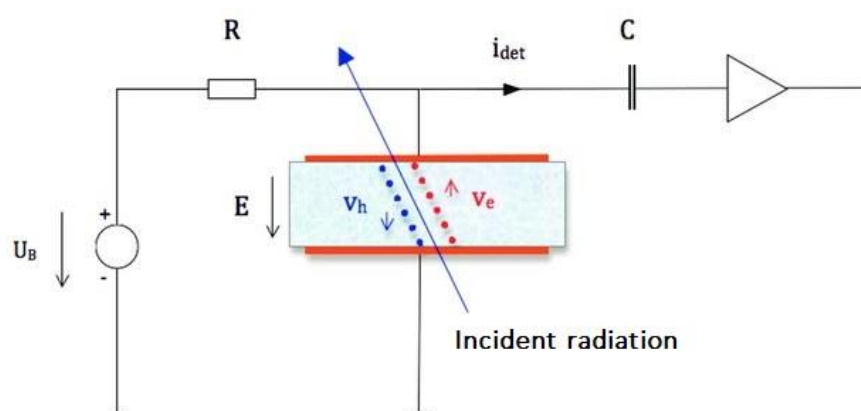


Figure 17. An operating principle of a synthetic diamond detector. The incident radiation generates charge carriers. These are separated by the electric field, thereby producing a signal

current that can be measured with an electrometer. Like silicon semiconductors, no external bias voltage is required. [74]

Diamond detectors do have disadvantages. They exhibit a substantial energy and dose rate dependence, so correction factors must be applied. In addition, although they have excellent long-term response stability, degradation of the detector's characteristic due to irradiation is inevitable.[29,41] The physical characteristic of a TW60019 microDiamond (PTW Freiburg, Germany) detector used in this research is stated in Table 6.

| | | microDiamond T60019 |
|---|---|---|
| **Specification** | **Reference point / mm [a]** | 1 |
| | **Response / nC/Gy [b]** | 1 |
| | **Bias voltage / V** | 0 |
| **Materials and measures** | **Window area density / mg/cm$^2$** | 101 |
| | **Dimensions** | Radius 1.1 mm Tick 1 μm |

Table 6. Physical characteristics of microDiamond detector.
[a] Reference point on the detector's axis, from the tip of a detector.
[b] Nominal response.

## 3.2.4. EBT3 radiochromic films

EBT3 radiochromic film alongside ionization chambers are some of the most widely available, trusted and studied detector in medical physics used for photon beam dosimetry. It is characterised by high resolution, tissue equivalence, independence of the energy and dose rate, with the possibility of 2D measurements.[75] In general, the field output factor and determination of dose profiles are in excellent agreement with the values obtained using Monte Carlo calculations.[17,24–26,30,46,60,75–77] Radiochromic EBT3 films are specially designed for the dosimetry of ionizing radiation and are particularly suited for dosimetry of high-energy photon beams. The EBT3 film is designed for best performance in the dose range from 0.2 to 10 Gy.

The EBT3 film is composed of an active monomer layer, nominally 28 μm tick, sandwiched between two 125 μm matte-polyester substrates. The active layer contains the active components, a marker dye, stabilizer and other components providing an almost energy-independent response.[42] After the film has been irradiated, an effect of polymerization takes place which results in the change of the film's optical density (OD). The polymerization process of a monomer unit is carried out in three steps: chain initiation, chain propagation and chain termination. This process takes up to 48 hours, and the film must be stored in a dark place at the appropriate temperature. The result of a polymerization effect is the darkening of the film, which increases with the absorbed dose.

Postirradiation processing in the determination of an absorbed dose starts with the film scanning in the red colour channel where it has a peak brightness at λ=636 nm regardless of an absorbed dose (Figure 18.).

A net optical density (netOD) is determined in the region of interest (ROI) as:

$$netOD = log \frac{PV_{unex} - PV_{bckg}}{PV_{exp} - PV_{bckg}} \qquad \textbf{3.2}$$

where, $PV_{unex}$ and $PV_{exp}$ are the pixel values (measure of pixels intensity) of an exposed and unexposed film respectively, and $PV_{bckg}$ is the pixel values of a background scan.
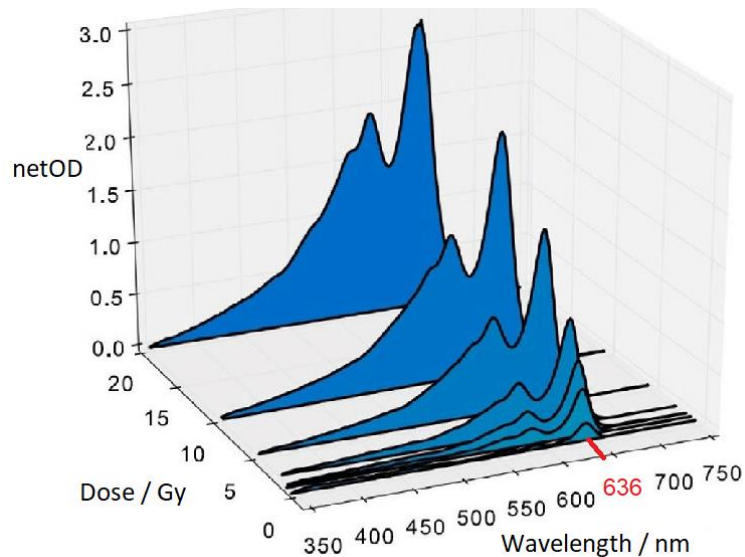
Figure 18. The visible absorption spectrum of seven EBT3 films at different absorbed doses ranging from 0 to 20 Gy after subtraction of a linear background in the range of 350-750 nm. The film has a peak net optical density at 636 nm.[77]

A calibration curve relates the absorbed dose with the film's net optical density. It can be obtained by fitting the Dević fit function to the net optical density determined from films irradiated with different absorbed doses:[76]

$$D\ (netOD) = a \cdot netOD + b \cdot netOD^n \qquad \text{3.3}$$

where, $D\ (netOD)$ is an absorbed dose as a function of a film's optical density, while $a$, $b$ and $n$ are fitting parameters. Some of EBT3's disadvantages include a limited lifespan and sensitivity to environmental factors like temperature, humidity and light which can affect the response. They are not intended for very high and low dose measurements. Static electricity can affect film causing them to stick to surfaces or attract dust. Signal to noise ratio in passive detectors such as EBT3 film is larger than in active detectors. In addition, every lot needs to have its own calibration curve. When handling the film, all the above-mentioned factors must be considered. A list of the main EBT3 film's characteristics is presented in Table 7.

| | |
|---|---|
| **Configuration** | The active layer (28 μm) sandwiched between 125 μm matte-surface polyester substrate |
| **Dose range** | 0.1 – 20 Gy |
| **Energy dependency** | <5 % difference in net optical density when exposed to 100 keV and 18 MeV |
| **Dose rate response** | <5% difference in net optical density for 10 Gy exposures at rates of 3.4 Gy/min and 0.034 Gy/min. |
| **Stability in light** | $< 5 \cdot 10^{-3}$ change in optical density per 1000 lux-day |
| **Stability in dark** | $< 5 \cdot 10^{-4}$ optical density change/day at 23°C and $< 2 \cdot 10^{-4}$ density change/day refrigerated |

Table 7. List of physical characteristics of EBT3 films as stated by the manufacturer.[42]

## 3.3. Ellipsoid absorbed dose model for Gamma Knife Icon

The ellipsoid absorbed dose model assumes that a single Gamma Knife isocentre absorbed dose delivery (i.e. shot) forms an ellipsoid in three-dimensional space.[78] To create a model the dose profiles along main spatial directions have to be fitted to an analytical expression:

$$D(k) = \sum_{i=1}^{n} A_i \cdot erf\left(\frac{k + a_i}{b_i}\right) + C_0 \qquad \textbf{3.4}$$

where $A_i$, $a_i$, $b_i$, and $C_0$ are fitting parameters, k is the off-axis distance on any of the major axes (x, y and z), erf is an error function. The error function with a complex variable (Gauss error function) is defined as:

$$erf(z) = \frac{2}{\sqrt{\pi}} \int_0^z e^{-t^2} dt \qquad \textbf{3.5}$$

For x and y-axis dose profiles of field sizes n=4 (Equation 3.4), for the z-axis of 16 mm and 8 mm dose profiles n=5, and n=2 for the 4 mm z-axis dose profile. When building the model it is assumed that dose profiles for all field sizes on the x and y-axis are symmetrical with respect to the z-axis i.e. f(x,y)=f(-x,-y). Consequently, only positive off-axis values were considered (Equation 3.4.) to fit dose profiles on the x and y-axis (only absolute values of k are allowed). This symmetry is due to the geometry of the collimating system in which Co-60 sources are symmetrically distributed around the z-axis. By contrast, sources are asymmetrically distributed around the x and y-axis, therefore, z-axis dose profiles are asymmetrical with respect to the XY plane and both positive and negative off-axis values must be considered when fitting. Asymmetry is most pronounced for the 16 mm field, and it is gradually reduced by decreasing the field down to 4 mm.

The ellipsoid absorbed dose model states that the dose can be considered as having individual components in each spatial direction which can be calculated as:

$$D_x \cdot cos\theta_x = f_x(|\vec{r_2} - \vec{r_1}|) \cdot (x_2 - x_1)/|\vec{r_2} - \vec{r_1}| \qquad \textbf{3.6}$$

$$D_y \cdot cos\theta_y = f_y(|\vec{r_2} - \vec{r_1}|) \cdot (y_2 - y_1)/|\vec{r_2} - \vec{r_1}| \qquad \textbf{3.7}$$

$$D_z \cdot cos\theta_z = f_z(\alpha \cdot |\vec{r_2} - \vec{r_1}|) \cdot (z_2 - z_1)/(|\vec{r_2} - \vec{r_1}|) \qquad \textbf{3.8}$$

where $\vec{r_1} = (x_1, y_1, z_1)$ are the coordinates of the absorbed dose distribution's centre, $\vec{r_2} = (x_2, y_2, z_2)$ are the coordinates of the point at which the absorbed dose is determined, $D_x$, $D_y$, and $D_z$ are the dose components on each major axis, and, $\Theta_x$, $\Theta_y$, and $\Theta_z$ are the angles between the displacement vector and the axis, finally, $\alpha$ is the sign of $(z_2 - z_1)$.

The absorbed dose $D(\vec{r})$ at any point $\vec{r_2} = (x_2, y_2, z_2)$ with shot focused at $\vec{r_1} = (x_1, y_1, z_1)$ is determined as:

$$D(\vec{r}) = \sqrt{\left(D_x \cdot \frac{x_2 - x_1}{|\vec{r_2} - \vec{r_1}|}\right)^2 + \left(D_y \cdot \frac{y_2 - y_1}{|\vec{r_2} - \vec{r_1}|}\right)^2 + \left(D_z \cdot \frac{z_2 - z_1}{|\vec{r_2} - \vec{r_1}|}\right)^2} \qquad \textbf{3.9}$$

Absorbed dose D, in the volume of interest V, can be calculated by integrating Equation 3.9., or numerically performing summation over the discrete values of dose-at-point inside the volume of interest (Equation 3.10.).

$$D_V = \int_V D(\vec{r}) \, d^3\vec{r} \approx \sum_{i=1}^{i \in V} D_i \Delta V \qquad \textbf{3.10}$$

In this work, an ellipsoid absorbed dose model is used for the determination of volume-averaging correction factors for different detectors listed in Table 1. Volume-averaging correction factors are determined using Equation 2.6. A comparison of accuracy in an absorbed dose predicted by the model and determined by the system for calculation and optimization of absorbed dose distributions, Leksell GammaPlan v.11.3.1 (LGP, Elekta, Stockholm), was performed for ellipsoids with different volumes starting at the centre of dose distribution and ending at different isodose values, eight different volumes in total for all field sizes, from 100% to 20% e.g. 100%– 90 %, 100% – 80%, …., 100% - 20%.  To do this, a single Gamma Knife shot was simulated by LGP with the shot's centre positioned at the centre of the Leksell coordinate system and a solid water phantom with an 80 mm radius and γ-angle set to 90°. A total of 1700, 783, and 378 points were extracted from LGP for 16 mm, 8 mm, and 4 mm fields, respectively. The selection of points was taken randomly for dose values ranging from 99% to 19% of the relative dose in all spatial directions. In MATLAB (TheMathWorks Inc.,

USA) an ellipsoid absorbed dose distribution was simulated using fitted normalized dose profiles (Equation 3.4.) for an ellipsoid absorbed dose model (Equation 3.9.). To simplify calculations dose distributions were shifted in a way that $\vec{r_1} = (0, 0, 0)$. An examination of the model's accuracy $R_v$ with respect to an absorbed dose distribution is done in a way that a set of points extracted from the LGP were entered in the model and an absorbed dose calculated by the LGP $D_{LGP}$ is compared against the model's $D_{model}$ for a different ellipsoid volume that spanned from the isocentre to a given isodose line (Equation 3.11.).

$$R_v = \frac{|D_{LGP} - D_{model}|}{D_{LGP}} \cdot 100\% \qquad \textbf{3.11}$$

# 3.4. Statistical analysis and uncertainty estimation of experimental data

Every measurement is susceptible to numerous external factors that need to be considered and properly corrected. There are two types of uncertainties. Type A uncertainty (statistical uncertainty) is determined using statistical analysis of a series of observations, while Type B uncertainty (non-statistical uncertainty) can be evaluated by means other than statistical analysis of a series of observations.[79] The pool of information for Type B uncertainty includes previously measured data, experience with or general knowledge of the behaviour and properties of relevant materials and instruments, manufacturer's specification or data provided in calibration and other certificates and uncertainty assigned to reference data taken from the handbook. IAEA TRS-483 CoP provides guidelines for the estimation of an uncertainties for different dosimetry procedures. These guidelines are an estimation based on the numerous studies performed and compiled together. However, for Gamma Knife, detailed instructions for Type B uncertainty are lacking.[10]

For EBT3 film dosimetry, the Type A uncertainty was calculated, while Type B uncertainty were not considered.

For dosimetry performed with the active detectors in Co-60 narrow photon beams, Type A uncertainty comes from:

- Detector short-term stability $\sigma_{sts}$ determined from multiple measurements i.e. standard deviation of repeated same measurements.
- Detector absorbed dose linearity $\sigma_{lin.}$ can be determined from the different irradiation times for the same field size. These measurements are performed in the msr field (16 mm) where perturbations related to the small field dosimetry are the smallest.
- Detector dose-rate linearity $\sigma_{dr.lin.}$ can be determined by irradiating detectors with different dose rates for the same time. On Gamma Knife, this can be achieved by switching off different sectors.
- Uncertainty due to the leakage $\sigma_l$ can be determined by collecting charge of detector when detector is not exposed to ionizing radiation.

Uncertainty in long-term detector stability is equal to a few percentages per year (for some detectors less than 1 %/year) and all measurements with a single detector have been performed over the period of few hours, therefore, for the purpose of this research the detector-long term stability has not been included in total uncertainty budget.[61,63–65]

Type B uncertainties in dosimetry with active detectors on Gamma Knife come from:

- Gamma Knife's geometrical uncertainty $\sigma_{PPS}$: uncertainty in the positioning of the detector's reference point at the isocentre i.e. the accuracy of PPS (Patient Positioning System). This can be estimated from the device's declared accuracy.[3,59]
- Uncertainty due to the electrometer stability $\sigma_{el}$. These values are determined from the electrometer specifications.[61–65,67]

Through this study, a formalism of the Joint Committee for Guides in Metrology (JCGM) was followed for estimations and calculations of uncertainties. This formalism is presented in the JCGM publication: Evaluation of Measurement Data – Guide to the Expression of Uncertainties in Measurements.[80]

## 3.4.1. Uncertainty in dosimetry with an EBT3 film

To estimate uncertainty $\sigma_{\left(D_{Q_0,Q_0}^{f_{clin},f_{msr}}\right)_{EBT3}}$ in the absorbed dose determined with EBT3 film, a modified Dević formalism was used.[76] The modifications were made with weighted fitting and included uncertainties in all fitting parameters as well as correlations between fitting parameters. The total uncertainty comes from the experimental uncertainty $\sigma_{D_{exp}}$ of determined netOD, uncertainty in the fitting parameters $\sigma_{D_{fit}}$ of a calibration curve and uncertainty due to the correlation of fitting parameters $\sigma_{corr}$.

$$\sigma_{D_{exp}} = \sqrt{(a + n \cdot b \cdot netOD^{n-1})^2 \cdot \sigma_{netOD}^2} \qquad \textbf{3.12}$$

$$\sigma_{D_{fit}} = \sqrt{netOD^2 \cdot \sigma_a^2 + netOD^{2n} \cdot \sigma_b^2 + 2b^2 netOD^2 \log(netOD)\sigma_n^2} \qquad \textbf{3.13}$$

$$\sigma_{corr} =$$

$$= \sqrt{2netOD^{n+1}(\sigma_{ab} + \sigma_{an}blog(netOD)) + 2\sigma_{bn}bnetOD^{2n}\log(netOD)} \qquad \textbf{3.14}$$

where $\sigma_a, \sigma_b, \sigma_N$ are uncertainties of fitting coefficients $a$, $b$, and $n$, $\sigma_{netOD}$ is the uncertainty of determined net optical density (Equation 3.3.), $\sigma_{ab}$, $\sigma_{an}$, $\sigma_{bn}$ are uncertainties in the correlation between fitting parameters and $D$ $(netOD)$ is dose determined at corresponding ROI with $netOD$.

Uncertainty in net optical density $\sigma_{netOD}$ can be calculated by applying uncertainty propagation formalism on the equation for determination of net optical density (Equation 3.2.):[76]

$$\sigma_{netOD} = \frac{1}{\ln 10}\sqrt{\frac{\sigma_{PV_{unex}}^2 + \sigma_{bckg}^2}{\left(PV_{unex} - PV_{bckg}\right)^2} + \frac{\sigma_{PV_{exp}}^2 + \sigma_{bckg}^2}{\left(PV_{exp} - PV_{bckg}\right)^2}} \qquad \textbf{3.15}$$

where, $\sigma_{I_{unex}}, \sigma_{I_{exp}}$ are uncertainties in the pixel values of an unexposed and exposed film, while $\sigma_{bckg}$ in uncertainty in the pixel value of a background scan.

Total percentage uncertainty for an absorbed dose determined with the EBT3 film $\sigma_{\left(D_{Q_0,Q_0}^{f_{clin},f_{msr}}\right)_{EBT3}}$, consisting of experimental uncertainty $\sigma_{D_{exp}}$, and uncertainty due to the fitting parameter $\sigma_{D_{fit}}$ is calculated as:

$$\sigma_{\left(D_{Q_0,Q_0}^{f_{clin},f_{msr}}\right)_{EBT3}} = \sqrt{\sigma_{D_{exp}}^2 + \sigma_{D_{fit}}^2 + \sigma_{corr}^2} \qquad \textbf{3.16}$$

Finally, since EBT3 film measurements are independent and uncorrelated, uncertainties in the field output factors determined with the EBT3 films are calculated by using Equation 3.17.[80]

$$\sigma_{\left(\Omega_{Q_0,Q_0}^{f_{clin},f_{msr}}\right)_{EBT3}} = \sqrt{\sum_{i=1}^{2}\left(\frac{\partial \Omega_{Q_0,Q_0}^{f_{clin},f_{msr}}}{\partial\left(\left(D_{Q_0,Q_0}^{f_{clin},f_{msr}}\right)_{EBT3}\right)_i}\sigma_{\left(\left(D_{Q_0,Q_0}^{f_{clin},f_{msr}}\right)_{EBT3}\right)_i}\right)^2}$$

$$== \sqrt{\left(\frac{1}{\left(D_{Q_0}^{f_{msr}}\right)_{EBT3}}\sigma_{\left(D_{Q_0}^{f_{clin}}\right)_{EBT3}}\right)^2 + \left(-\frac{\left(D_{Q_0}^{f_{clin}}\right)_{EBT3}}{\left(D_{Q_0}^{f_{msr}}\right)_{EBT3}^2}\sigma_{\left(D_{Q_0}^{f_{msr}}\right)_{EBT3}}\right)^2} \qquad \textbf{3.17}$$

### 3.4.2. Uncertainty in dosimetry with an active detector

The uncertainty of active detector comes from Type A uncertainty and uncertainty in the alignment of the detector's reference point at the isocentre and electrometer stability (Type B). The total uncertainty is determined as:

$$\sigma_{tot} = \sqrt{\sigma_{TypeA}^2 + \sigma_{TypeB}^2} \qquad \textbf{3.18}$$

To calculate uncertainties for field output factors $\sigma_{\Omega_{Q_0,Q_0}^{f_{clin},f_{msr}}}$ and volume-averaging correction factors $\sigma_{(k_{vol})_{Q_0}^{f_{msr},f_{clin}}}$ a Gaussian theory is used.[80] An uncertainty for field output factor can be determined as:

$$\sigma_{\Omega_{Q_0,Q_0}^{f_{clin},f_{msr}}} = \sqrt{\sum_{i=1}^{2}\left(\frac{\partial \Omega_{Q_0,Q_0}^{f_{clin},f_{msr}}}{\partial\left(M_{Q_0}^{f_{clin},f_{msr}}\right)_i}\left(\sigma_{tot}^{f_{clin},f_{msr}}\right)_i\right)^2} \qquad \textbf{3.19}$$

$$\sigma_{\Omega_{Q_0,Q_0}^{f_{clin},f_{msr}}} = \sqrt{\left(\frac{1}{M_{Q_0}^{,f_{msr}}}\sigma_{tot}^{f_{clin}}\right)^2 + \left(-\frac{M_{Q_0}^{,f_{clin}}}{\left(M_{Q_0}^{,f_{msr}}\right)^2}\sigma_{tot}^{f_{msr}}\right)^2} \qquad \textbf{3.20}$$

where $\sigma_{tot}^{f\,clin}$ and $\sigma_{tot}^{f\,msr}$ are total uncertainty (Type A and B) of a detected charge in the clinical and machine-specific reference field.

When estimating Type B uncertainties with active detectors the most important factor is the geometrical accuracy of the PPS e.g. alignment of the detector's effective point of measurement at the isocentre. The maximum allowed geometrical error is 0.3 mm[59], and to estimate the error of the detected signal a rectangular probability density function is assumed where all outcomes are equality likely to occur. To convert an uncertainty with a rectangular distribution to a standard deviation equivalent we have divided the estimated uncertainty $U_{PPS}$ by the square root of three.

$$\sigma_{PPS} = \frac{U_{PPS}}{\sqrt{3}} \qquad \textbf{3.21}$$

where $\sigma_{PPS}$ is the standard uncertainty and $U_{PPS}$ is the estimated uncertainty.

Additionally, electrometer uncertainty was determined from its specification. [81,82]

The combined standard uncertainty is multiplied by the coverage factor that indicated the level of confidence in the measurement result. This new value (combined standard uncertainty multiplied by the coverage factor) is expanded uncertainty:

$$\sigma_{exp} = k\sigma_{tot} \qquad \textbf{3.22}$$

where k is the coverage factor. The primary standard for all dosimetry quantities in medical physics uses k=2, corresponding to an interval with a 95% level of confidence.[80]

The detector-specific correction factor in different fields is determined by dividing the field output of a detector $\left(\Omega_{Q_0,Q_0}^{f\,clin,f\,msr}\right)_{detector}$ with the reference values such as EBT3 and Monte Carlo $\left(\Omega_{Q_0,Q_0}^{f\,clin,f\,msr}\right)_{MC,EBT3}$.

$$k_{Q_0,Q_0}^{f\,clin,f\,msr} = \frac{\left(\Omega_{Q_0,Q_0}^{f\,clin,f\,msr}\right)_{detector}}{\left(\Omega_{Q_0,Q_0}^{f\,clin,f\,msr}\right)_{MC,EBT3}} \qquad \textbf{3.23}$$

By using the same statistical analysis as before, an uncertainty for the detector-specific correction factor $\sigma_{k_{Q_0,Q_0}^{f_{clin},f_{msr}}}$ can be determined as:

$$\sigma_{k_{Q_0,Q_0}^{f_{clin},f_{msr}}} = \left( \left( \frac{1}{\left(\Omega_{Q_0,Q_0}^{f_{clin},f_{msr}}\right)_{detector}} \sigma_{\left(\Omega_{Q_0,Q_0}^{f_{clin},f_{msr}}\right)_{MC,EBT3}} \right)^2 + \left( -\frac{\left(\Omega_{Q_0,Q_0}^{f_{clin},f_{msr}}\right)_{MC,EBT3}}{\left(\left(\Omega_{Q_0,Q_0}^{f_{clin},f_{msr}}\right)_{detector}\right)^2} \sigma_{\left(\Omega_{Q_0,Q_0}^{f_{clin},f_{msr}}\right)_{detector}} \right)^2 \right)^{\frac{1}{2}} \qquad \textbf{3.24}$$

When calculating uncertainty for the detector specific correction factor, field output values obtained with the Monte Carlo $\sigma_{\left(\Omega_{Q_0,Q_0}^{f_{clin},f_{msr}}\right)_{MC}}$ were taken as absolute i.e. without uncertainty.

Uncertainties for volume-averaging $\sigma_{(k_{vol})_{Q_0}^{f_{msr},f_{clin}}}$ are determined similarly as for field output factors, by partially deriving an expression for volume-averaging (Equation 2.6.).

$$\sigma_{(k_{vol})_{Q_0}^{f_{msr},f_{clin}}} = \sqrt{\left( \frac{\partial (k_{vol})_{Q_0}^{f_{msr},f_{clin}}}{\partial D_{Q_0}^{f_{msr},f_{clin}}} \sigma_{D_{Q_0}^{f_{msr},f_{clin}}} \right)^2} \qquad \textbf{3.25}$$

Where $D_{Q_0}^{f_{msr},f_{clin}}$ is an absorbed dose over the detectors volume in clinical and msr field with beam quality $Q_0$. When derived (Equation 3.25.):

$$\sigma_{(k_{vol})_{Q_0}^{f_{msr},f_{clin}}} = \sqrt{\left( -\frac{V}{D_{Q_0}^{f_{msr},f_{clin}^2}} \sigma_{D_{Q_0}^{f_{msr},f_{clin}}} \right)^2} \qquad \textbf{3.26}$$

and by substituting $\sigma_{D_{Q_0}^{f_{msr},f_{clin}}} = D_{Q_0}^{f_{msr},f_{clin}} \cdot \overline{R_v}$,

$$\sigma_{(k_{vol})_{Q_0}^{f_{msr},f_{clin}}} = \sqrt{\left( -\frac{V}{D_{Q_0}^{f_{msr},f_{clin}}} \overline{R_v} \right)^2} = (k_{vol})_{Q_0}^{f_{msr},f_{clin}} \cdot \overline{R_v} \qquad \textbf{3.27}$$

where $\overline{R_v}$ is the mean uncertainty in determined absorbed dose within the detector effective volume and it is determined as an average value of difference between TPS and elliptical absorbed dose model for a given field.

## 3.5. Uncertainties with active detectors

There are three sources of uncertainness for which measurements with active detectors had to be conduct. This uncertainness come from leakage current which negatively affect the collected charge, detector's dose rate dependence and uncertainty in the linearity of detector's response with the absorbed dose. All three factors will affect the accuracy of final result and must be appropriately considered in the uncertainty budget.

Detector's leakage current refers to the current that flows through a detector even when it's not actively detecting any signal. In various electronic devices, especially in semiconductor-based detectors, this current can arise due to imperfections or impurities in the materials used to construct the detector. The magnitude of the detector leakage current depends on factors such as the type of detector, its operating conditions, and the quality of its construction. In some applications, minimizing detector leakage current is crucial to improve the sensitivity and accuracy of measurements.

To estimate leakage current uncertainty $\sigma_l$, a charge collected when detector is outside of the field is divided by the charge collected when detector is inside different fields.

$$\sigma_l = \frac{M_0}{M_{msr,clin}}$$  **3.28**

where, $M_0$ is the charge collected outside of the filed and $M_{msr, clin}$ is the charge collected in the clinical and machine-specific reference field.

Linearity in absorbed dose refers to the relationship between the dose of radiation delivered to a material and the response of the radiation detector used to measure that dose. In an ideal scenario, the response of the detector would be directly proportional to the absorbed dose received by the material being measured. This means that if you double the absorbed dose,

the detector's response would also double. This linear relationship simplifies calibration and interpretation of measurements. However, in reality, there can be deviations from perfect linearity. Maintaining linearity in absorbed dose measurements is important for ensuring the accuracy and reliability of radiation dose assessments in various applications, including medical radiation therapy, industrial radiography, and environmental monitoring. Calibration procedures and correction factors are often employed to account for any non-linearities and ensure accurate dose measurements across a wide range of dose levels.

Uncreating $\sigma_{lin}$ in the linearity of an absorbed dose can be determined from measurements as:

$$\sigma_{lin} = \sqrt{\frac{\sum_{i=1}^{n}\left(M_{observed} - M_{fitted}\right)^2}{n-2}} \qquad \textbf{3.29}$$

where $M_{observed}$ is the measured charge, $M_{fit}$ is the fitted value for the same measurement, and n is the number of measurements.

Finally, dose-rate linearity $\sigma_{dr.\ lin}$ refers to the relationship between the dose rate of radiation and the response of a radiation detector. In an ideal scenario, the detector's response would be directly proportional to the dose rate, meaning that if the dose rate doubles, the detector's response (such as the electrical signal it produces) would also double. Uncertainty in the dose rate linearity can be determined by using the Equation 3.29.

# 4. Experimental Setup and Measurements

## 4.1. Determination of field output and detector-specific correction factors

Determination of field output factors $\Omega_{Q_{clin},Q_{msr}}^{f_{clin},f_{msr}}$ is most important part of a small photon field dosimetry. In this research, field output factors were determined for thirteen detectors (seven ionization chambers, four semiconductor detectors, a diamond detector and EBT3 film) specified in Table 1.

### 4.1.1. Determination of field output factors using EBT3 films

Due to the properties of an EBT3 film it can be used as a reference detector to obtain a detector-specific correction factor $k_{Q_{clin},Q_{msr}}^{f_{clin},f_{msr}}$ for other detectors. In all measurements involving EBT3 film, the same protocol for an absorbed dose determination was used:[76]

- Irradiated films were wrapped with aluminium foil and stored for a minimum of 48 hours at a temperature of about 10°C so that optical density can saturate.

- Scanning was performed in transmission mode of EPSON EXPRESSION 10000XL (Epson America Inc., Long Beach) scanner in the red channel with a resolution of 150 dpi. Before the film scanning, the scanner was warmed up to ensure scanning stability.

- ImageJ software (National Institutes for Health, USA) was used for image processing and noise filtering. Filtering of noise was done by applying the filter within 3x3 pixel kernel.

- Region of interest (ROI) was placed at the centre of the film and its diameter equalled 4, 2, and 0.8 mm for 16 mm, 8 mm, and 4 mm beam sizes respectively. This ROI was used to maximise the number of points inside it and to improve the signal-to-noise ratio. The calibration curve for the film lot used in this research was created by irradiating a set of films in the XY plane using a 16 mm absorbed dose distribution with doses ranging from 0.4 to 8 Gy.

- Calibration curve was obtained by fitting the function (Equation 3.3.) to the net optical density of pixel values determined at the ROI placed at the centre of a films irradiated with different absorbed doses.

- For the calculation of field output factors, the average pixel value for all three beam sizes is determined at the ROI and related to the net optical density (netOD) (Equation 3.2.). Finally, the field output factors were calculated as a ratio of the dose in the clinical and machine-specific reference fields (Equation 2.10.).

Before irradiation, it was necessary to find the coordinates of the shot. Accurate positioning of the film inside the field is essential, especially for the 4 mm field whose dose plateau is very small, therefore it is crucial to position the film at the centre of a field. This problem is illustrated in Figure 19.
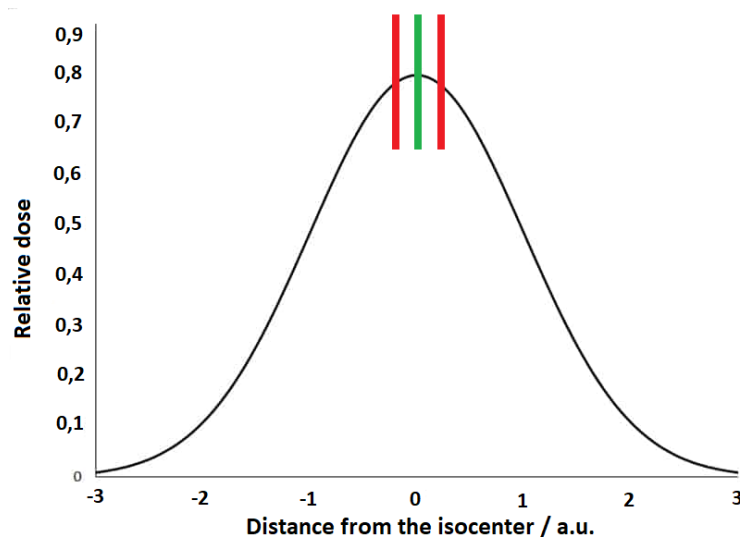


Figure 19. Illustration of the correct (green) and incorrect (red) positioning of the EBT3 film in the narrow photon beam.

To solve this, a test film (Figure 20.) was positioned inside the solid water phantom in the XY plane and a CBCT (Cone-Beam Computed Tomography) scanning was performed to find the coordinates of the centre of the film (in the z-direction). These coordinates were used for the determination of field output factors. All films for field output factor determination were irradiated in the XY plane with shot coordinates (100.2, 100.2, 99.4). Irradiation time was 2.69 minutes which corresponds to 6 Gy of an absorbed dose for a 16 mm field size.
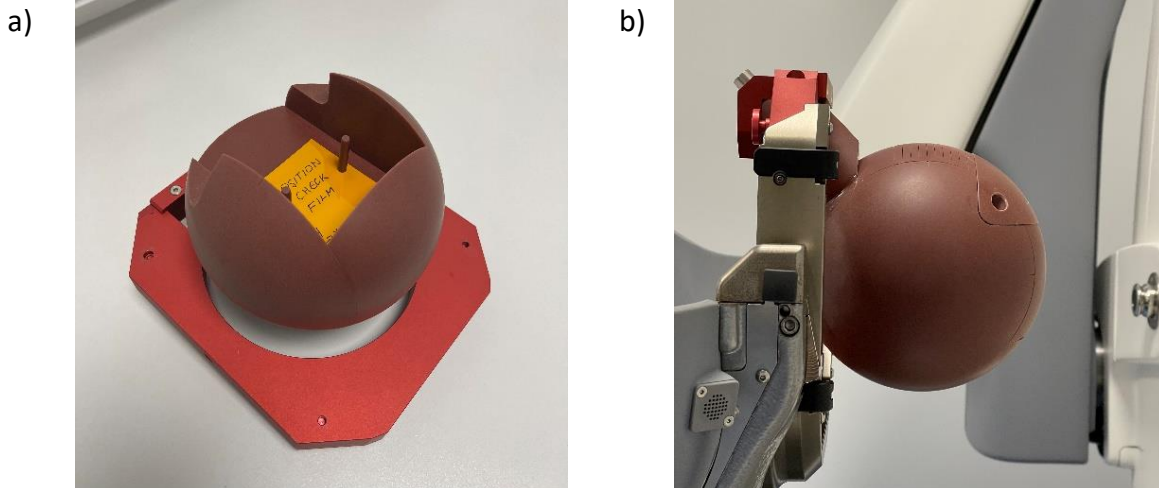
Figure 20. Open (a) and closed (b) solid water phantom with test film.

To determine field output factors with EBT3 film, a calibration curve was created by irradiating eighteen films with different doses from 0 Gy to 8 Gy. The field output factor is calculated as the ratio of absorbed doses in the clinical and machine-specific reference field as:

$$\Omega_{Q_0,Q_0}^{f_{clin},f_{msr}} = \frac{D_{Q_0}^{f_{clin}}}{D_{Q_0}^{f_{msr}}} \qquad \textbf{4.1}$$

## 4.1.2. Determination of field output factors using active detectors

Determination of field output factors $\Omega_{Q_{clin},Q_{msr}}^{f_{clin},f_{msr}}$ with the active detectors was performed in the solid water phantom with the long axis of a detector positioned in the z direction of the Leksell coordinate system (Figure 21.).
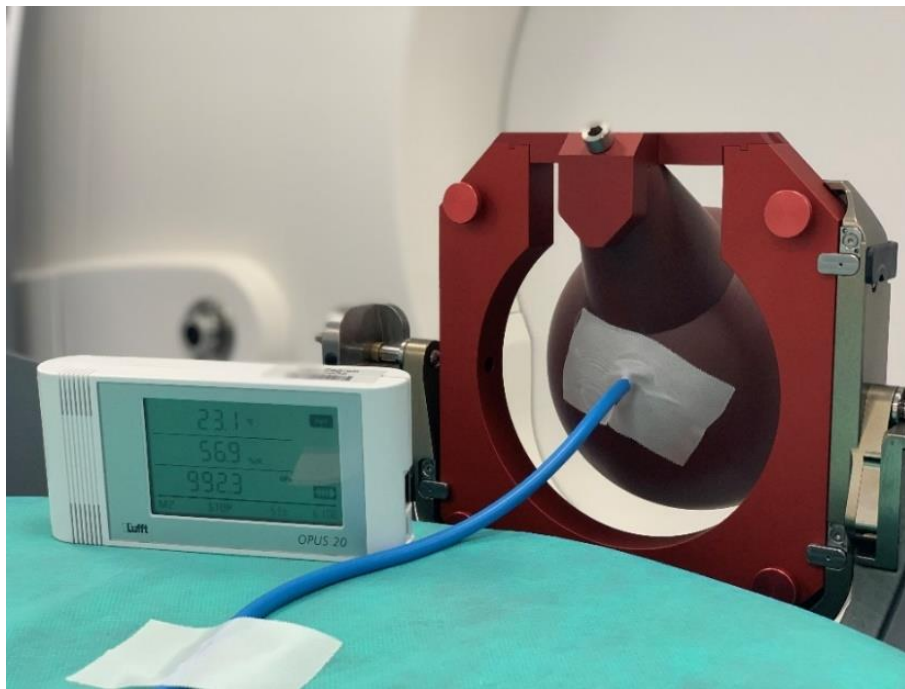


Figure 21. Experimental setup for field output factors determination using an ionization chamber.

Custom 3D-printed inserts were manufactured out of tissue-equivalent plastics for detectors that do not have inserts provided by the manufacturer. Also, any remaining air gaps were filled with tissue-equivalent gel. The presence of air gaps was checked with CBCT. Coordinates of reference point were determined firstly by performing a CBCT scan (Figure 22.) and manually positioning the detector at the shot centre along with additional adjustments according to measured dose profiles of three principal axes with the resolution of 0.5 mm and 15 seconds of signal acquisition M. For IBA's detectors, the DOSE 1 High Performance Reference Class Electrometer was used, and for the remaining detectors, the PTW UNIDOS E electrometer was used.[81,82]
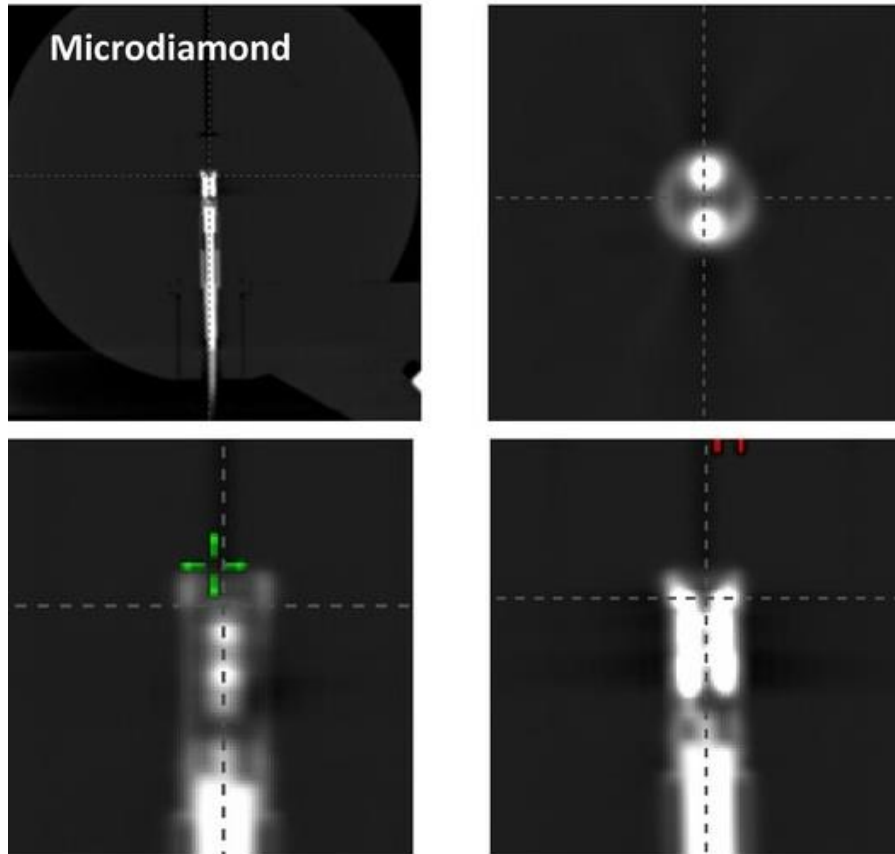
Figure 22. A CBCT scan of PTW microDiamond T60019 inside the solid water phantom. The image shows a coronal image of the entire phantom with detectors inside it, (top left), axial (top right), longitudinal (bottom left) and sagittal (bottom right) reconstruction.[83]

The x coordinate of a reference point can be determined as a weighted average of the detector position from dose profile measurements as:

$$x = \frac{\sum_{i=1}^{n} x_i M_i}{\sum_{i=1}^{n} M_i} \qquad \textbf{4.2}$$

where $x_i$ is the coordinate of a point on a profile's axis at which $M_i$ charge is determined. The same procedure was done for the y and z coordinates of the reference point. This is the most accurate method of detector positioning, and it assures that the detector's reference point is at the shot's centre (Table 8.).

| Detector | x / mm | y / mm | y / mm |
|---|---|---|---|
| Semiflex T31010 | 100.1 | 99.7 | 99.4 |
| Semiflex 3D T31021 | 100.2 | 99.7 | 99.8 |
| PinPoint T31014 | 100.1 | 99.7 | 99.8 |
| PinPoint 3D T31016 | 100.2 | 99.8 | 99.8 |
| RAZOR chamber | 100.2 | 99.6 | 100.4 |
| RAZORnano chamber | 100.3 | 99.7 | 99.4 |
| IBA CC04 | 100.3 | 99.8 | 102.5 |
| Diode P T60016 | 100.2 | 99.7 | 100.9 |
| Diode E T60017 | 100.2 | 99.6 | 100.2 |
| RAZOR diode | 100.4 | 99.8 | 99.5 |
| EDGE detector | 101.6 | 100.2 | 101.4 |
| microDiamond T60019 | 100.2 | 99.2 | 100.1 |
| EBT3 | 100.2 | 100.2 | 99.4 |

Table 8. Coordinates of the detector's effective point of measurement for field output factor determination on the Gamma Knife Icon.

To determine field output factors, ten measurements of response during 60 seconds of acquisition time were averaged for each beam size. Temperature and pressure were monitored when using air-vented ionization chambers.

Therefore, the response determined with vented ionization chambers must be corrected for pressure and temperature changes which affect field output factors (Equation 4.3.).

$$\Omega_{Q_0,Q_0}^{f_{clin},f_{msr}} = \frac{M_{Q_0}^{f_{clin}} \cdot \left(k_{t,p}\right)_{clin}}{M_{Q_0}^{f_{msr}} \cdot \left(k_{t,p}\right)_{msr}} \qquad \textbf{4.3}$$

Temperature and pressure were monitored with an OPUS 20 THI device (G. Luffi Mess – und Regeltechnik GmbG, Deutschland).[84] A detector-specific correction factor $k_{Q_0,Q_0}^{f_{clin},f_{msr}}$ for active detectors is determined by comparing the measured output with values obtained using Monte Carlo and EBT3 film. For clarity, the notation was changed from $Q_{msr}$ and $Q_{clin}$ to $Q_0$ to indicate the same beam quality in the machine-specific reference field and clinical field.

$$k_{Q_0,Q_0}^{f_{clin},f_{msr}} = \frac{\left(\Omega_{Q_0,Q_0}^{f_{clin},f_{msr}}\right)_{MC,EBT3}}{\left(\Omega_{Q_0,Q_0}^{f_{clin},f_{msr}}\right)_{detector}} \qquad \textbf{4.4}$$

To determine the difference in field output factors $\Omega_{Q_0,Q_0}^{f_{clin},f_{msr}}$ of active detectors from values obtained with the Monte Carlo and EBT3 film, a relative difference R$_{EBT3, MC}$ is calculated (Equation 4.5.). This value gives information on whether it is appropriate to use a detector in a given field size. Ideally, $R_{EBT3,MC} = 0$ %.

$$R_{EBT3,MC} = \frac{\left(\Omega_{Q_0,Q_0}^{f_{clin},f_{msr}}\right)_{detector} - \left(\Omega_{Q_0,Q_0}^{f_{clin},f_{msr}}\right)_{EBT3,MC}}{\left(\Omega_{Q_0,Q_0}^{f_{clin},f_{msr}}\right)_{EBT3,MC}} \cdot 100\% \qquad \textbf{4.5}$$

## 4.2. Volume-averaging correction factors

To determine a volume-averaging correction factor $(k_{vol})_{Q_0}^{f_{msr},f_{clin}}$ in clinical and machine-specific reference fields, an ellipsoid absorbed dose model was used for simulation of absorbed dose distribution along with geometries of different detectors. The formalism of an ellipsoid absorbed dose model of Gamma Knife Icon was explained in section 3.3., while simulation of that model in MATLAB was performed (Equation 3.9. ) with a fitted dose profile (Equation 3.4.).

The volume-averaging correction factor was determined by integrating the relative dose distribution over the detector's effective volume using numerical integration; the Simpson's method with hundred integration steps in each spatial direction e.g., the volume of the detector was divided into one million parts. The volume-averaging correction factor was determined as a ratio of the detector's effective volume with the value of a normalized field integrated over that volume (Equation 2.6.). When simulating the detector's geometry, detectors were positioned inside the field in a way that their reference point is placed at the centre of the Leksell coordinate system with coordinates (100, 100, 100) with the detector's long axis parallel with the z direction. The code written in MATLAB used for the determination of the volume-averaging correction factor is provided in Appendix B. A list of the examined detectors can be found in Table 1. To calculate the volume-averaging correction factor, it was necessary to know the detailed geometry of each detector and its position inside the different absorbed dose distributions. Detailed geometry implies data on the boundaries and shape of the effective volume and size of a central electrode, if any. This was determined using schematics provided by the manufacturers.[61,63–65] Since most detector's effective volumes are cylindrical, the integration in the cylindrical coordinate system was performed. Diamond and most of the semiconductor detectors have a cylindrical effective volume except for the EDGE detector which is rectangular. An illustration of different detector geometries can be seen in Figure 23. All investigated ionization chambers are cylindrical in shape with a curved top and cylindrical central electrode. Detailed schematics of ionization chambers can be found in Appendix A.
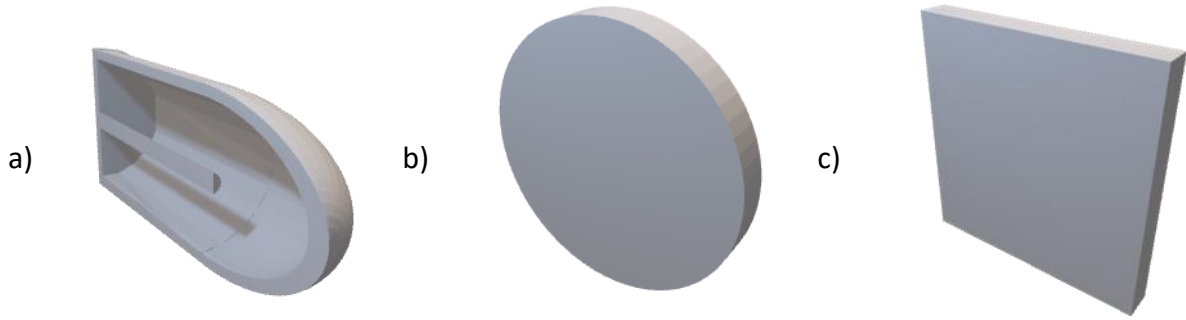
Figure 23. Illustration of the geometry of effective volume for studied detectors: a) ionization chambers, b) diamond, plastic scintillator and semiconductor detectors except, c) EDGE SunNuclear detector.

The design of an ionization chamber can be subdivided into three parts:

1. Cylindrical part from the bottom until the beginning of a cap
2. Cap on the top with the radius of curvature R, and
3. Cylindrical electrode.

To accurately calculate volume-averaging over the hemispherical part of an ionization chamber it was necessary to find the radius of curvature i.e. the equation for the curvature of a cap in cylindrical coordinates. For some ionization chambers, the top part was a spherical cap. Therefore, it was necessary to solve a system of equations (Equations 4.7. and 4.8.) to calculate the volume of a spherical cap. In general, for cylindrical ionization chambers the size of the effective volume is calculated as:

$$V = V_{cylin} + V_{cap} - V_{elec} \qquad \textbf{4.6}$$

where, $V_{cylin}$, $V_{cap}$ and $V_{elec}$ are the volumes of a cylinder, cap and electrode respectively.
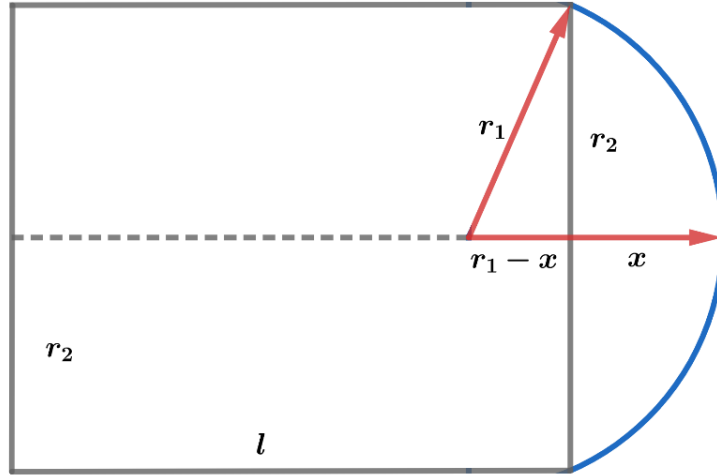
Figure 24. The geometry of an ionization chamber.

From Figure 24. it follows:

$$V = V_{cylin} + V_{cap} - V_{elec} = r_2^2 \pi l + \frac{\pi x^2}{3}(3r_1 - x) - V_{elec} \qquad \textbf{4.7}$$

$$r_2^2 - 2r_1 x + x^2 = 0 \qquad \textbf{4.8}$$

and by solving Equations 4.7. and 4.8., we can obtain $r_1$ and x values. An equation of a cap's curvature can be expressed in the cylindrical coordinate system as:

$$s^2 + (z + r_1 - x)^2 = r_1^2 \qquad \textbf{4.9}$$

where s and z are the coordinates in the cylindrical coordinate system. Dimensions of ionization chambers used in this research are listed in Table 9. Numerical calculations of volume-averaging correction factors for ionization chambers were done in three steps over three different chamber volumes:

1. Integral over the cylindrical part – $J_1$
2. Integral over the cap part – $J_2$
3. Integral over the volume of the electrode – $J_3$

The total integral value $J_{tot}$ of an ionization chamber, the denominator of Equation 2.6., is determined as:

$$J_{tot} = J_1 + J_2 - J_3 \qquad\qquad \textbf{4.10}$$

| Ionization chambers | $r_1$ / mm | $r_2$ / mm | l / mm | $r_1$ - x / mm |
|---|---|---|---|---|
| Semiflex T31010 | 2.50 | 2.75 | 4.00 | 0.00 |
| Semiflex 3D T31021 | 2.40 | 2.40 | 2.80 | 0.40 |
| PinPoint T31014 | 1.98 | 1.00 | 4.73 | 0.27 |
| PinPoint 3D T31016 | 1.58 | 1.45 | 1.94 | 0.96 |
| RAZOR chamber | 1.00 | 1.00 | 2.60 | 0.00 |
| CC04 | 2.00 | 2.00 | 1.60 | 0.10 |

Table 9. Dimensions of ionization chambers used for volume-averaging determination.

| Detectors | Length / μm | Radius / mm |
|---|---|---|
| Diode P T60016 | 30 | 0.56 |
| Diode E T60017 | 30 | 0.56 |
| EFD 3G-pSI | 80 | 1.60 |
| RAZOR diode | 20 | 0.30 |
| microDiamond | 1 | 1.10 |
| Exradin W2 1x1 | 1000 | 1.00 |
| Exradin W2 1x3 | 3000 | 1.00 |
| EDGE | 30 | 0.8 (square) |

Table 10. Dimensions of cylindrically shaped effective volumes of detectors used for volume-averaging determination. EDGE detector has s square effective volume.

A volume-averaging perturbation $(k_{vol})_{Q_0,Q_0}^{f_{msr},f_{clin}}$, a part of detector-specific field output correction factor $k_{Q_0,Q_0}^{f_{msr},f_{clin}}$, was determined as:

$$(k_{vol})_{Q_0,Q_0}^{f_{msr},f_{clin}} = \frac{(k_{vol})_{Q_0}^{f_{msr},clin}}{(k_{vol})_{Q_0}^{f_{msr}}} \qquad\qquad \textbf{4.11}$$

where $(k_{vol})_{Q_0}^{f_{msr},clin}$ is the volume-averaging correction factor in msr and clin field and $(k_{vol})_{Q_0}^{f_{msr}}$ is the volume averaging correction factor in msr (16 mm) field. The contribution of a volume-averaging to a field output correction factor as:

$$k_{\%vol} = \frac{(k_{vol})_{Q_0,Q_0}^{f_{msr},f_{clin}}}{k_{Q_0,Q_0}^{f_{msr},f_{clin}}} \cdot 100\% \qquad\qquad \textbf{4.12}$$

## 4.3. Gamma Knife's Perfexion dose profiles

Relative dose profile determination, also known as off-axis ratios, refers to the measurements of the absorbed dose or relative dose distribution along a particular axis. Dose profiles on Gamma Knife are typically measured along three principal axes due to the device's collimator system (Figure 6.).[85,86]

Dose profiles are usually obtained by moving a detector along the axis and measuring the response at various points. They can be also measured with planar detectors e.g., EBT3 or an array of detectors. On the other hand, active detectors such as diodes, and ionization chambers may average the response over the detectors' effective volume affecting the dose profiles (Figure 5.). Reference geometry for dose profile determination on Gamma Knife implies using a film detector placed inside a spherical phantom which is positioned at the isocentre. By contrast, in non-reference geometry the active detector is positioned in the phantom and moved along the desired axis to measure detector's response at various points. Choosing the right detector is a nontrivial task requiring a profound knowledge of the detector's performance and design, with volume-averaging usually being the main limiting factor. A detailed process of profile determination with film detectors on Gamma Knife is explained in the Report of the American Association of Physicists in Medicine (AAPM) Task Group 178 (TG 178).[86] The resulting data is used to create a graph of a measured detector's response as a function of distance from the isocentre on the principal axis of the Gamma Knife. Dose profiles can be used to verify photon beam shape and alignment of the beam's central axis with the target. According to the TG 178, the tolerance of all FWHM values of measured dose profiles is ±1 mm of the TPS data calculated by the Monte Carlo.

The dose profile, illustrated in Figure 25, is characterized by:

- full width at half maximum (FWHM).
- width of penumbra region; between 80% - 20% of isodose value.
- dose gradient – up to 70%/mm for 4 mm field. In this work, a mean dose gradient is calculated in the penumbra region.
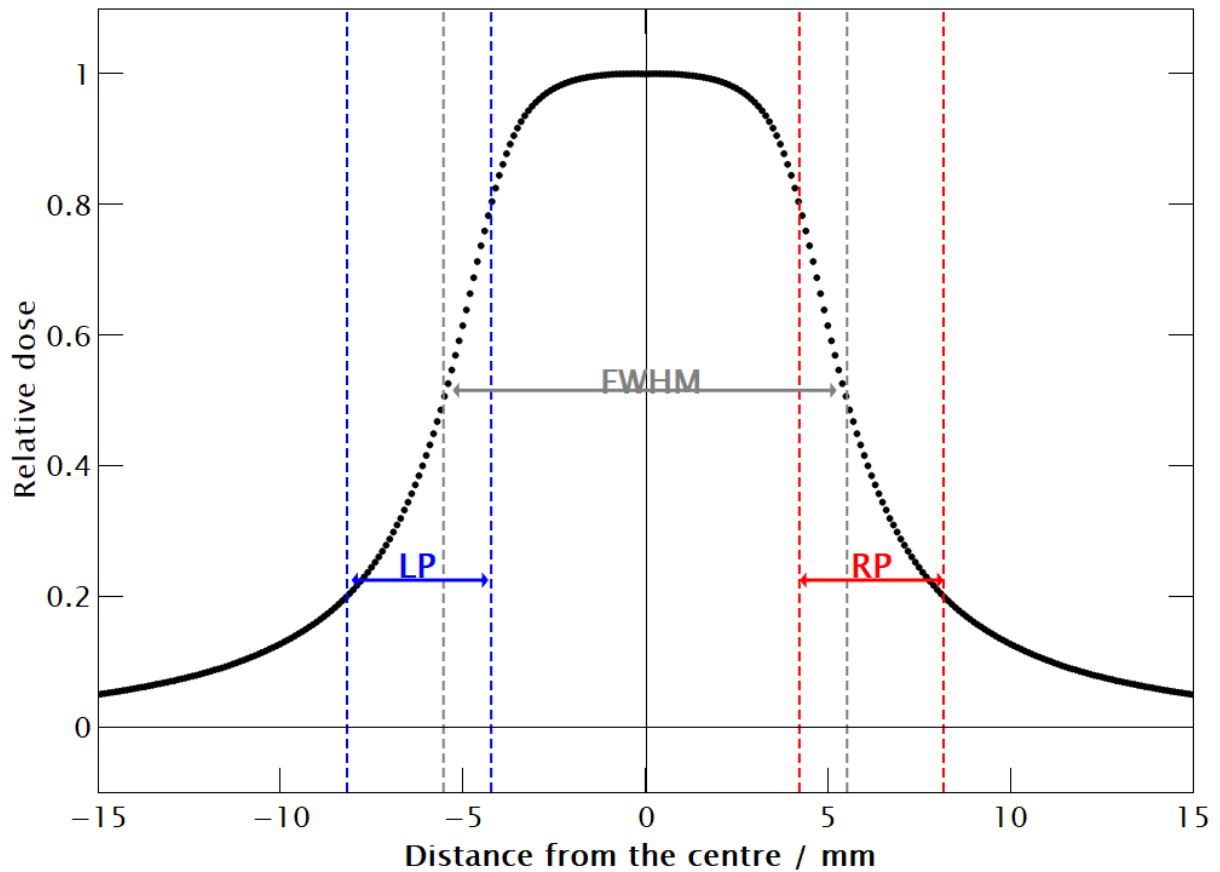
Figure 25. An illustration of a dose profiles with its main characteristics. LP and RP stands for the width of left and right penumbra, respectively.

Dose profiles were determined with active detectors (Table 1.) positioned in the spherical solid water phantom the same way as for the field output factor determination (Figure 21.).

Dose profiles were determined with resolution of 0.2 mm and 15 s of detector acquisition time for each spatial point. Afterwards, measured profiles are normalized to a maximum value of an absorbed dose and imported into CurveExpert Professional software where Savitzky – Golay smoothing is applied to the data points (Figure 26.).
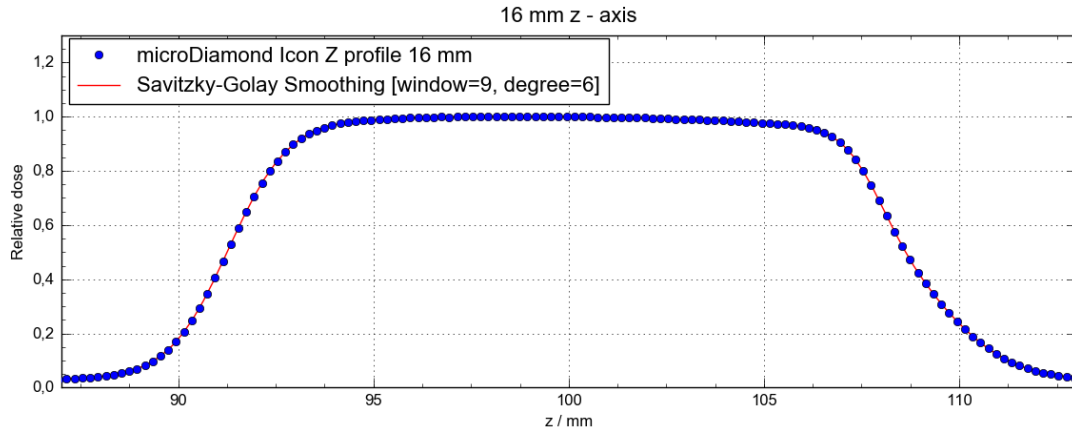
16 mm z - axis

Figure 26. Example of Savitzky - Golay smoothing (red line) for 16 mm z-axis dose profile measured with microDiamond T60019.

For the determination of dose profiles with EBT3 films, a total of six films were used, two for each collimator. Films were positioned at the XY and XZ plain and irradiated with the absorbed dose of 6 Gy at the maximum, for a 16 mm collimator. From previous experience, we found that two planes are enough to determine all three dose profiles. Piercing of the film is performed to create fiducial holes as references for profile determination in each plane. The same postprocessing procedure of EBT3 films for dose profile determination was followed as for the field output factor determination.
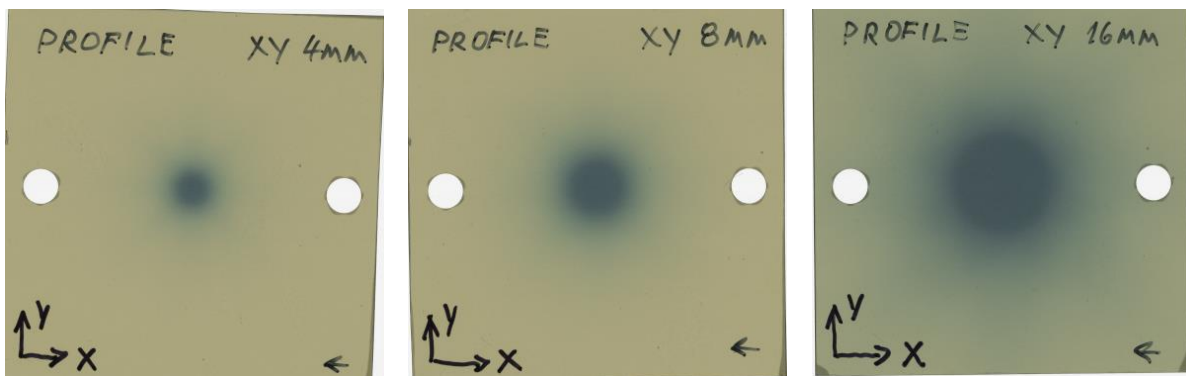


Figure 27. Example of EBT3 film irradiated in XY plane with fiducial holes for dose profile determination. All EBT3 films were scanned in the same direction (bottom right corner arrow) to eliminate variations in measured relative optical density due to film's orientation relative to the scanning direction.[87]

After saturation of the film's optical density, the scanning was performed and dose profiles were determined using ImageJ software with the help of fiducial points as a reference for each plane. The resulting optical density was normalized at the values 6 Gy, 5.334 Gy and 4.956 Gy for 16 mm, 8 mm and 4 mm field sizes respectively. An example of a 16 mm z-axis dose profile measured with EBT3 film is shown in Figure 28.
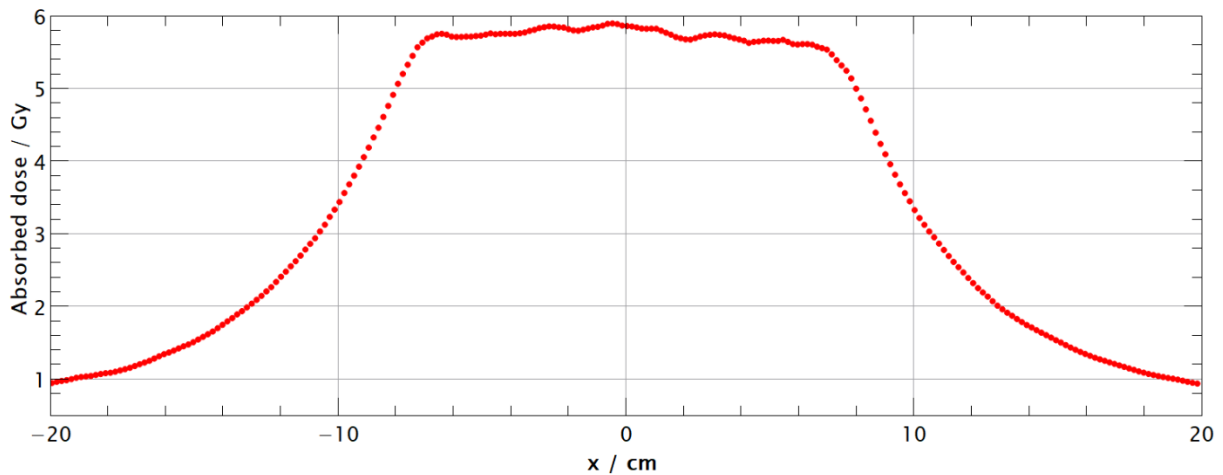


Figure 28. An example of an ImageJ filtered 16 mm x-axis dose profile determined with EBT3 film.

To find a centre of the film, Equation 4.2. was used only in the penumbra region as explained in TG 178.[88] From there, the film centre $x_{cent}$ was determined as:

$$x_{cent} = \frac{x_1 + x_2}{2} \qquad \text{4.13}$$

where $x_1$ and $x_2$ are the centres of the left and right penumbras respectively. Afterwards, the resulting profiles were imported into CurveExpert Professional and the same analysis is done as for the profiles obtained with active detectors.

# 5. Results and Discussion

## 5.1. Uncertainties in dosimetry of Co-60 narrow photon beams

| | Field size / mm | Value / % |
|---|---|---|
| **Uncertainty in netOD:** $\sigma_{netOD}$ | 16: $\sigma_{netOD_{16}}$ | 0.16 |
| | 8: $\sigma_{netOD_8}$ | 0.10 |
| | 4: $\sigma_{netOD_4}$ | 0.10 |
| **Combined uncertainties** | | |
| **Uncertainty in the absorbed dose for 16 mm, 8 mm and 4 mm field size:** $\sigma_{\left(D_{Q_0,Q_0}^{f_{msr},f_{clin}}\right)_{EBT3}}$ | 16: $\sigma_{\left(D_{Q_0}^{16}\right)_{EBT3}}$ | 3.17 |
| | 8: $\sigma_{\left(D_{Q_0}^{8}\right)_{EBT3}}$ | 2.99 |
| | 4: $\sigma_{\left(D_{Q_0}^{4}\right)_{EBT3}}$ | 2.91 |
| **Uncertainty in the field output factor:** $\sigma_{\left(\Omega_{Q_0,Q_0}^{f_{msr},f_{clin}}\right)_{EBT3}}$ | 16: $\sigma_{\left(\Omega_{Q_0}^{f_{16}}\right)_{EBT3}}$ | 4.49 |
| | 8: $\sigma_{\left(\Omega_{Q_0}^{f_8}\right)_{EBT3}}$ | 4.36 |
| | 4: $\sigma_{\left(\Omega_{Q_0}^{f_4}\right)_{EBT3}}$ | 4.31 |

Table 11. Uncertainty analysis for the dosimetry of Gamma Knife's Perfexion narrow photon beams with the EBT3 film (field output factors). Values are rounded to two significant digits.

In this section, the results of uncertainty analysis are presented for passive (Table 11.) and active detectors (Table 12.).

The determination of an absorbed dose with EBT3 film is subjected to uncertainties that come from three basic sources; from an experimental nature in determining dose using netOD $\sigma_{D_{exp}}$ using the fit function, from the fit process $\sigma_{fit}$, and from the correlation between fit parameters $\sigma_{corr}$.[76] The experimental uncertainty is primarily caused by the contribution from netOD measurement uncertainty $\sigma_{netOD}$ and less by other means (e.g. registration of a source with a film, uncertainty in the Gamma Knife calibration, mismatch in the temporal and thermal history of a film, the difference in mean response from one piece of a film to another etc.). For calculation of uncertainties in net optical density $\sigma_{netOD}$ an error propagation expression is used (Equation 3.15.). When examining uncertainty in the absorbed dose determined with the EBT3 film $\sigma_{\left(D_{Q_0,Q_0}^{f_{msr},f_{clin}}\right)_{EBT3}}$ the largest contribution is due to the uncertainty of the fitting

parameters $\sigma_{fit}$ (Table 11.). Experimental uncertainty in the dose determined $\sigma_{D_{exp}}$ can be reduced by irradiating more films. When combined, the uncertainty in the absorbed doses $\sigma_{\left(D_{Q_0,Q_0}^{f_{msr},f_{clin}}\right)_{EBT3}}$ are 3.17%, 2.98% and 8.91% for 16 mm, 8 mm, and 4 mm field size. Finally, as uncertainty propagate thorough calculations, the uncertainties in the field output factor $\sigma_{\left(\Omega_{Q_0,Q_0}^{f_{msr},f_{clin}}\right)_{EBT3}}$ are increased to 4.49%, 4.36%, and 4.31% for 16 mm, 8 mm, and 4 mm field, respectively.

From this analysis, one can see that although EBT3 film has desirable qualities such as tissue equivalence, energy and dose rate independence, it is burdened with relatively large uncertainties when used for absorbed dose determination. This uncertainty comes from the film's design, post-irradiation processing and experience in handling such detectors.[76] This is the main reasons why measurements obtained with an EBT3 film detector should always be compared against measurements with an active detector to ensure the best accuracy of the result.

| | Type A uncertainties | | | | | | | | Type B uncertainties | | | |
| --- | --- | --- | --- | --- | --- | --- | --- | --- | --- | --- | --- | --- |
| | Detector's short-term Stability $\sigma_{sts}$ / % | | | Linearity in absorbed dose $\sigma_{lin}$ / % | Dose-rate linearity $\sigma_{dr.\,lin}$ / % | Leakage $\sigma_l$ / % | | | Electrometer Stability / % | Detector and phantom Positioning $\sigma_{PPS}$ / % | | |
| Field size / mm  Detector name | 16 | 8 | 4 | All fields | All fields | 16 | 8 | 4 | All fields | 16 | 8 | 4 |
| Semiflex T31010 | 0.015 | 0.009 | 0.021 | 0.007 | 0.130 | 0.010 | 0.013 | 0.030 | 0.5 | 0.06 | 0.30 | 0.48 |
| Semiflex 3D T31021 | 0.011 | 0.020 | 0.019 | 0.120 | 0.130 | 0.019 | 0.022 | 0.042 | 0.5 | 0.06 | 0.30 | 0.48 |
| PinPoint T31014 | 0.008 | 0.029 | 0.011 | 0.024 | 0.094 | 0.077 | 0.088 | 0.120 | 0.5 | 0.06 | 0.30 | 0.48 |
| PinPoint 3D T31016 | 0.013 | 0.014 | 0.017 | 0.083 | 0.120 | 0.072 | 0.082 | 0.110 | 0.5 | 0.06 | 0.30 | 0.48 |
| RAZOR chamber | 0.033 | 0.066 | 0.057 | 0.160 | 0.150 | 0.270 | 0.300 | 0.370 | 0.2 | 0.06 | 0.30 | 0.48 |
| IBA CC04 | 0.025 | 0.025 | 0.050 | 0.044 | 0.180 | 0.091 | 0.110 | 0.160 | 0.2 | 0.06 | 0.30 | 0.48 |
| RAZORnano chamber | 0.480 | 0.200 | 0.260 | 0.310 | 0.610 | 0.048 | 0.053 | 0.059 | 0.2 | 0.06 | 0.30 | 0.48 |
| Diode P T60016 | 0.020 | 0.052 | 0.024 | 0.180 | 0.590 | 0.010 | 0.011 | 0.011 | 0.5 | 0.06 | 0.30 | 0.48 |
| Diode E T60017 | 0.037 | 0.046 | 0.017 | 0.099 | 0.620 | 0.028 | 0.031 | 0.033 | 0.5 | 0.06 | 0.30 | 0.48 |
| RAZOR diode | 0.190 | 0.053 | 0.051 | 0.059 | 0.210 | 0.046 | 0.052 | 0.055 | 0.5 | 0.06 | 0.30 | 0.48 |
| EDGE detector * | 0.026 | 0.026 | 0.032 | / | / | / | / | / | 0.5 | 0.06 | 0.30 | 0.48 |
| microDiamond T60019 | 0.055 | 0.041 | 0.017 | 0.480 | 0.210 | 0.053 | 0.060 | 0.065 | 0.5 | 0.06 | 0.30 | 0.48 |

Table 12. Results of an uncertainty analysis for the field output determined with active detectors. Values are rounded to two significant digits.
* Uncertainties of EDGE detector were not examined because of the unavailability of that detector.

| Field size / mm | $D\,(0, 0, 0)\,/\,a.u.$ | $D\,(0, 0, 0.3)\,/\,a.u.$ |
|:---:|:---:|:---:|
| 4 mm | 1.000 | 0.992 |
| 8 mm | 1.000 | 0.995 |
| 16 mm | 1.000 | 0.999 |

Table 13. Reduction in detected signal if the detector's reference point is misaligned by 0.3 mm from the isocentre in the z direction.

The main source of uncertainties in the relative dosimetry of Gamma Knife's narrow photon beams with active detectors comes from the uncertainty in the positioning of the detector's effective point of measurements at the isocentre (Type B uncertainty) (Table 12.). The assumption is made, that for every measurement, a detector's effective point of measurement was misaligned from the device's isocentre by 0.3 mm in the z direction. This displacement represents the maximum allowed geometrical error of the Gamma Knife Perfexion device and displacement in the z direction was assumed since maximum uncertainty is expected in that direction. It is shown that the difference in the detector's response is increasing with a decrease in the field size (Table 13.). Because 16 mm and 8 mm fields do have dose plateau, a displacement from the isocentre will affect the absorbed dose by 0.1% and 0.51% respectively. On the other hand, the dose plateau of the 4 mm field is non-existent therefore displacement from the field centre will result in the 0.83% reduction from the maximum absorbed dose. To calculate the uncertainty in the detector positioning $\sigma_{PPS}$ the uniform probability distribution was used (Equation 3.21.).

In the IAEA TRS-483 CoP it is stated that the selection of detectors for small field dosimetry should be such that its uncertainty in short-term stability, dose and dose-rate linearity and leakage current all should be lower than 0.1%.[10] From our data (Table 12.), detectors stability (Type A uncertainty) is, in general, higher for ionization chambers comparing to semiconductor or diamond detectors, with very few exceptions. Moreover, the short-term stability of an ionization chamber increases with the size of its effective volume. This can be noticed in the RAZORnano chamber with the smallest effective volume being a single detector that does not satisfy IAEA criteria on detector short-term stability (<0.1%) which is in line with the recent findings of multicentre experimental study.[89] Interestingly, detector stability i.e. measurement reproducibility, cannot be correlated with the field size, with a significant

number of detectors having the largest uncertainty in the 16 mm or 8 mm field size. In addition, detectors have shown a higher uncertainty in dose-rate dependence than in absorbed dose linearity.

Out of eleven investigated detectors in narrow Co-60 beams, five of them have values in linearity of absorbed dose higher than IAEA recommends (<0.1%), and ten have their values higher when it comes to the dose-rate linearity. In previous small field dosimetry study involving high energy X-rays, less than 50% of investigated detectors have satisfied IAEA criteria for linearity as well as dose-rate dependence. It has been shown that if 90% of investigated detectors were to satisfy criteria the tolerance level must be increased.[89] Relatively high values in the absorbed dose linearity in narrow Co-60 beams for microDiamond detector could be a symptom of the degradation of the detector's characteristic due to irradiation that these detectors are known for.[29,74] Values of leakage current are increasing with the decrease in the field size. This is expected since less charge is detected in smaller field therefore the relative contribution of leaked charge is increasing (Equation 3.28.). Out of thirty-three leakage current measurements, (eleven detectors in three fields), six are over 0.1% with four of them being in the smallest 4 mm field size (Table 12.), which is in line with the results of the multicentre experiment study.[89]

Finally, results of this study confirm previous findings involving detector's linearity and dose-rate dependence in high energy X-rays. Notably, the fact that the limit of 0.1% is too low for much of the investigated detectors. Therefore, the revision and increase of this limit in order to be achievable in experimental studies should be considered.[89]

Combined uncertainties were calculated as square root of quadratically added individual uncertainties (Equation 3.18.), and to calculate expanded uncertainty it was multiplied by the coverage factor (k=2) to ensure a confidence of 95% (Table 14.).[80]

| Detector name | Combined uncertainties / % | | | Expanded uncertainties (k=2) / % | | |
|---|---|---|---|---|---|---|
| Fields size / mm | 16 | 8 | 4 | 16 | 8 | 4 |
| Semiflex T31010 | 0.52 | 0.60 | 0.71 | 1.04 | 1.20 | 1.41 |
| Semiflex 3D T31021 | 0.53 | 0.61 | 0.72 | 1.07 | 1.22 | 1.43 |
| PinPoint T31014 | 0.52 | 0.60 | 0.71 | 1.04 | 1.20 | 1.42 |
| PinPoint 3D T31016 | 0.53 | 0.61 | 0.72 | 1.06 | 1.21 | 1.43 |
| RAZOR chamber | 0.41 | 0.52 | 0.68 | 0.81 | 1.05 | 1.35 |
| IBA CC04 | 0.29 | 0.42 | 0.58 | 0.59 | 0.84 | 1.15 |
| RAZORnano chamber | 0.86 | 0.80 | 0.90 | 1.72 | 1.59 | 1.79 |
| Diode P T60016 | 0.79 | 0.85 | 0.93 | 1.56 | 1.69 | 1.85 |
| Diode E T60017 | 0.81 | 0.86 | 0.94 | 1.62 | 1.72 | 1.88 |
| RAZOR diode | 0.58 | 0.63 | 0.73 | 1.16 | 1.25 | 1.46 |
| EDGE detector* | 0.50 | 0.58 | 0.69 | 1.01 | 1.17 | 1.39 |
| microDiamond T60019 | 0.73 | 0.79 | 0.87 | 1.46 | 1.57 | 1.74 |

Table 14. Combined and expanded uncertainty for the field output determined with active detectors. Values are rounded to the second significant digit.

*Calculated uncertainties of EDGE detector may be smaller than they actually are, since some uncertainties were not examined due to the unavailability of this detector.

## 5.2. Charged particle equilibrium for different detectors in narrow Co-60 beams used by Gamma Knife

In this section, investigated detectors are evaluated in different Gamma Knife's absorbed dose distributions with respect to the charged particle equilibrium. Tissue-phantom ratio $TPR_{20,\,10}$ for Co-60 ($k_Q$=1) is taken to be 0.56[48], and calculated lateral range of secondary electron $r_{LCPE}$ (Equation 2.1.) is 3.883 mm.

If charged particle equilibrium exists at the center of a detector's effective volume with detector's diameter $d$ placed inside absorbed dose distribution with dimensions $FWHM_{msr,clin}$ then $FWHM_{msr,clin} \geq 2r_{LCPE} + d$. $FWHM_{msr,clin}$ values are determined by the device's manufacturer with Monte Carlo simulations (Pegasos based system).

| | | Dose profile FWHM / mm | | | | | |
| --- | --- | --- | --- | --- | --- | --- | --- |
| | | 16 x | 16 z | 8 x | 8 z | 4 x | 4 z |
| Detector name | $2r_{LCPE} + d$ / mm | 21.75 | 17.44 | 11.06 | 9.80 | 6.16 | 5.04 |
| Semiflex T31010 | 14.67 | CPE | CPE | No CPE | No CPE | No CPE | No CPE |
| Semiflex 3D T31021 | 12.56 | CPE | CPE | No CPE | No CPE | No CPE | No CPE |
| PinPoint T31014 | 11.16 | CPE | CPE | No CPE | No CPE | No CPE | No CPE |
| PinPoint 3D T31016 | 12.01 | CPE | CPE | No CPE | No CPE | No CPE | No CPE |
| RAZOR ch. | 10.76 | CPE | CPE | No CPE | No CPE | No CPE | No CPE |
| IBA CC04 | 12.56 | CPE | CPE | No CPE | No CPE | No CPE | No CPE |
| RAZORnano ch. | 10.76 | CPE | CPE | CPE | No CPE | No CPE | No CPE |
| Diode P T60016 | 8.32 | CPE | CPE | CPE | CPE | No CPE | No CPE |
| Diode E T60017 | 8.32 | CPE | CPE | CPE | CPE | No CPE | No CPE |
| RAZOR diode | 8.36 | CPE | CPE | CPE | CPE | No CPE | No CPE |
| EDGE detector | 8.56 | CPE | CPE | CPE | CPE | No CPE | No CPE |
| microDiamond T60019 | 9.96 | CPE | CPE | CPE | No CPE | No CPE | No CPE |

Table 15. Results of CPE analysis for different detectors.

Absorbed dose distribution of Gamma Knife is ellipsoidal, therefore, to evaluate different detectors inside such distributions it is necessary to do it in two planes: XY and XZ. Moreover, the XY plane is circular while XZ and YZ planes are elliptical. Because of this, an evaluation of CPE for a given detectors in XY plane can be done with the respect to one dose profile (i.e. x-axis). On the other hand, to evaluate CPE in XZ plane, an evaluation must be done with the respect to z-axis dose profile. In addition, due to the difference in dimensions of dose profiles, if CPE is violated in XY plane it is also violated in XZ plain. Only detectors used for the field output factor determination are considered in this analysis, and their dimensions are determined from the detector's schematics.[61,63–65]

From CPE condition, the maximum allowed diameter of a detector for CPE to exist at the centre is: 9.674 and 2.034 mm for 16 mm an 8 mm field size respectively. So far, not a single detector can fulfil the CPE condition for a 4 mm field since the lateral range of secondary electrons is larger than the FWHM value.

## 5.3. Ellipsoid absorbed dose model of Gamma Knife Perfexion

In this section results of an ellipsoid absorbed dose model used for the determination of volume-averaging correction factor are presented. Normalized fitted dose profiles (Equation 3.4.) can be seen in Figure 29.
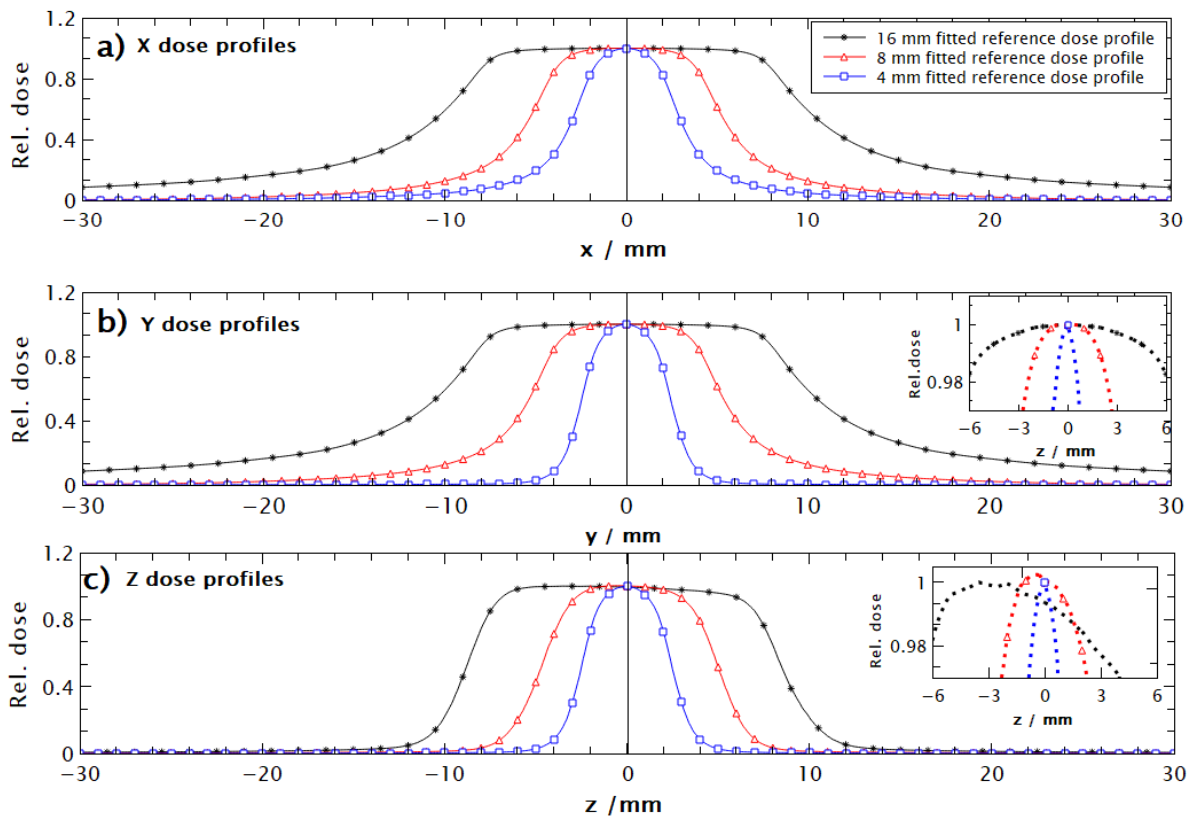


Figure 29. Normalized fitted dose profiles for a 16 mm, 8 mm and 4 mm field size on LGK Perfexion. Data were calculated using Monte Carlo calculation by the device's manufacturer for a shot at the centre of a spherical phantom with a radius of 80 mm. a) dose profile on the x–axis, b) dose profile on the y-axis with the insert showing symmetry in y dose profile, and c) dose profile on the z-axis with insert of enlarged centre of the profile showing asymmetry.

In MATLAB (TheMathWorks Inc, USA), using Equation 3.9., the visualization of different Gamma Knife's absorbed dose distributions was created as shown in Figure 30.
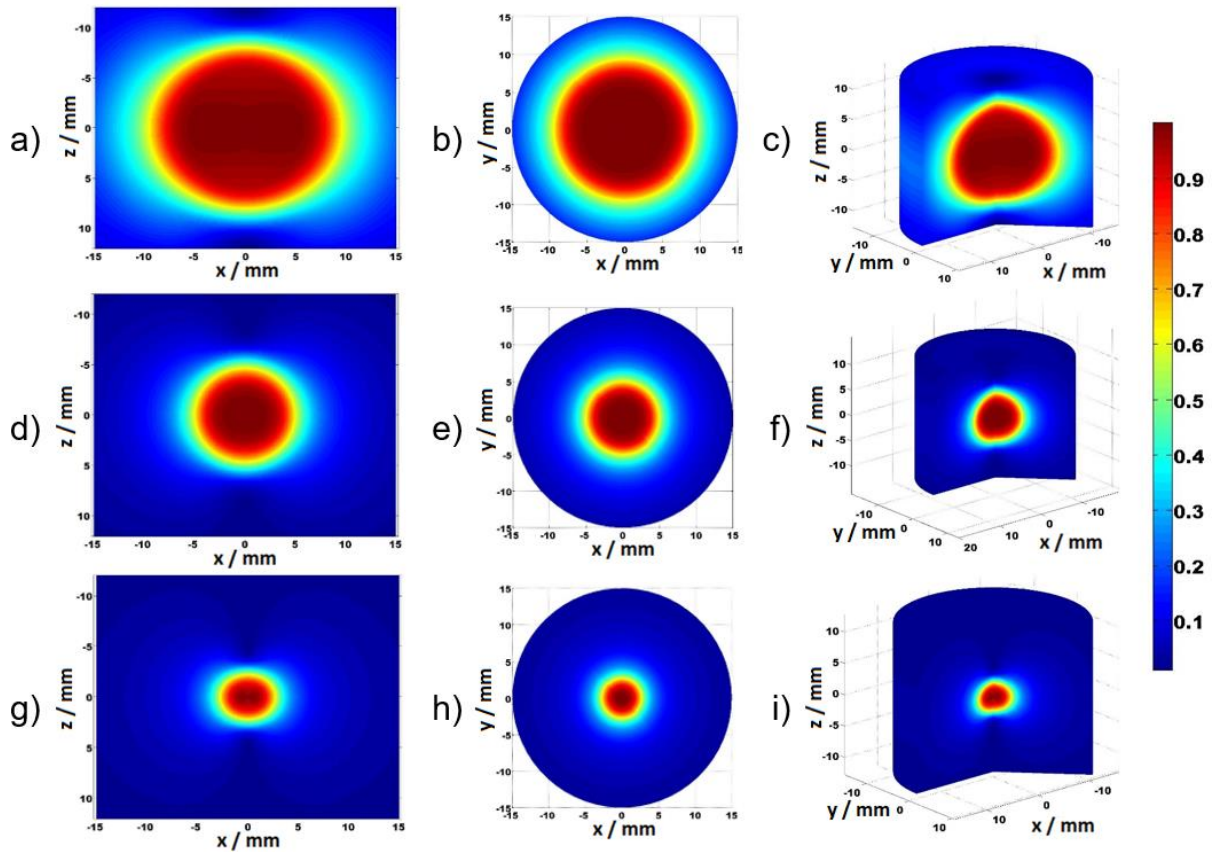
Figure 30. A Gamma Knife Perfexion field size simulation using the ellipsoid absorbed dose model. From a)-c): XZ, XY plane and 3D simulation of 16 mm absorbed dose distribution, from d)-f): XZ, XY plane and 3D simulation of 8 mm absorbed dose distribution, from g)-i): XZ, XY plane and 3D simulation of 4 mm absorbed dose distribution. For the XZ plane y=0, and z=0 for the XY plane.

An ellipsoid absorbed dose model accuracy was verified against the LGP for 1700, 783 and 378 points for 16 mm, 8 mm, and 4 mm field sizes ranging from 99% to 19% of the relative dose. The accuracy of a model with respect to an absorbed dose was the highest for the 4 mm field size, with the 16 mm field having the largest difference from the LGP (Figure 31.). For 4 mm field size the largest difference of all analysed points was around 0.5%. The difference in the absorbed doses for an 8 mm field size is 1.5% at the 80% isodose and it is gradually decreasing for lower isodoses. For 16 mm field size, the difference is the smallest at the 90% isodose volume and it is gradually increased to 2.25% for 30% isodose volume. Interestingly, the model displays an increase in accuracy with a decrease in the field size.[54] This can be contributed to the lower asymmetry of the 4 mm z-axis dose profile and consequently better fitting.
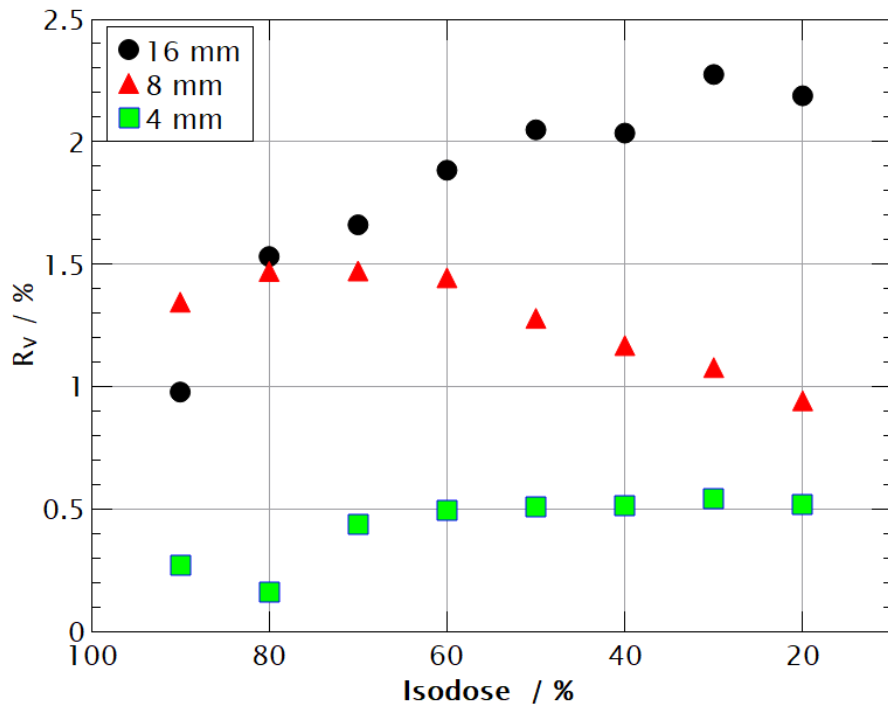
Figure 31. A difference in an absorbed dose between the LGP and the model for different ellipsoid volumes beginning at the isocentre and ending at the givens dose value.

It is beneficial that the model increases its accuracy with a decrease in the field size because the largest volume-averaging is expected in the smallest field sizes. In this analysis, we conclude that the ellipsoids absorbed dose model can be used for the determination of volume-averaging correction factors.

## 5.4. Volume-averaging correction factors

Volume-averaging correction factors $(k_{vol})_{Q_0}^{f_{msr,clin}}$ for detectors listed in Table 1. are calculated using the Equation 2.6. and are presented in Table 16. and Figure 32.[54] Mean uncertainties in the absorbed dose predicted by the model are 1.79%, 1.15% and 0.43% for 16 mm, 8 mm and 4 mm field size and corresponding to Type A uncertainties (Figure 31). Since volume-averaging correction is calculated using a mathematical model, and not measured, Type B uncertainties were not examined.

| Detector name | $(k_{vol})_{Q_0}^{f_{msr,clin}}$ | | |
| --- | --- | --- | --- |
| | 16 mm | 8 mm | 4 mm |
| Semiflex T31010 | 1.006±0.018 | 1.042±0.012 | 1.627±0.007 |
| Semiflex 3D T31021 | 1.005±0.018 | 1.019±0.012 | 1.304±0.006 |
| PinPoint T31014 | 1.005±0.018 | 1.011±0.012 | 1.181±0.005 |
| PinPoint 3D T31022 | 1.003±0.018 | 1.011±0.012 | 1.101±0.005 |
| Diode P T60016 | 1.001±0.018 | 1.001±0.012 | 1.008±0.004 |
| Diode E T60017 | 1.001±0.018 | 1.001±0.012 | 1.008±0.004 |
| microDiamond T60019 | 1.000±0.018 | 1.002±0.012 | 1.021±0.004 |
| RAZOR diode | 1.001±0.018 | 1.000±0.012 | 1.004±0.004 |
| EFD 3G-pSi | 1.001±0.018 | 1.001±0.012 | 1.018±0.004 |
| EDGE detector | 1.004±0.018 | 1.003±0.012 | 1.007±0.004 |
| RAZOR chamber | 1.003±0.018 | 1.006±0.012 | 1.074±0.005 |
| IBA CC04 | 1.007±0.018 | 1.014±0.012 | 1.156±0.005 |
| Exradin W2 1x1 | 1.003±0.018 | 1.002±0.012 | 1.010±0.004 |
| Exradin W2 1x3 | 1.005±0.018 | 1.005±0.012 | 1.042±0.004 |

Table 16. A result of volume-averaging correction factors $(k_{vol})_{Q_0}^{f_{msr,clin}}$ with uncertainties $\sigma_{(k_{vol})_{Q_0}^{f_{msr,clin}}}$ for different detectors in different fields of Gamma Knife Perfexion. Detectors whose volume-averaging correction factors are marked in red are not recommended by IAEA TRS-483 CoP for dosimetry at that field size.
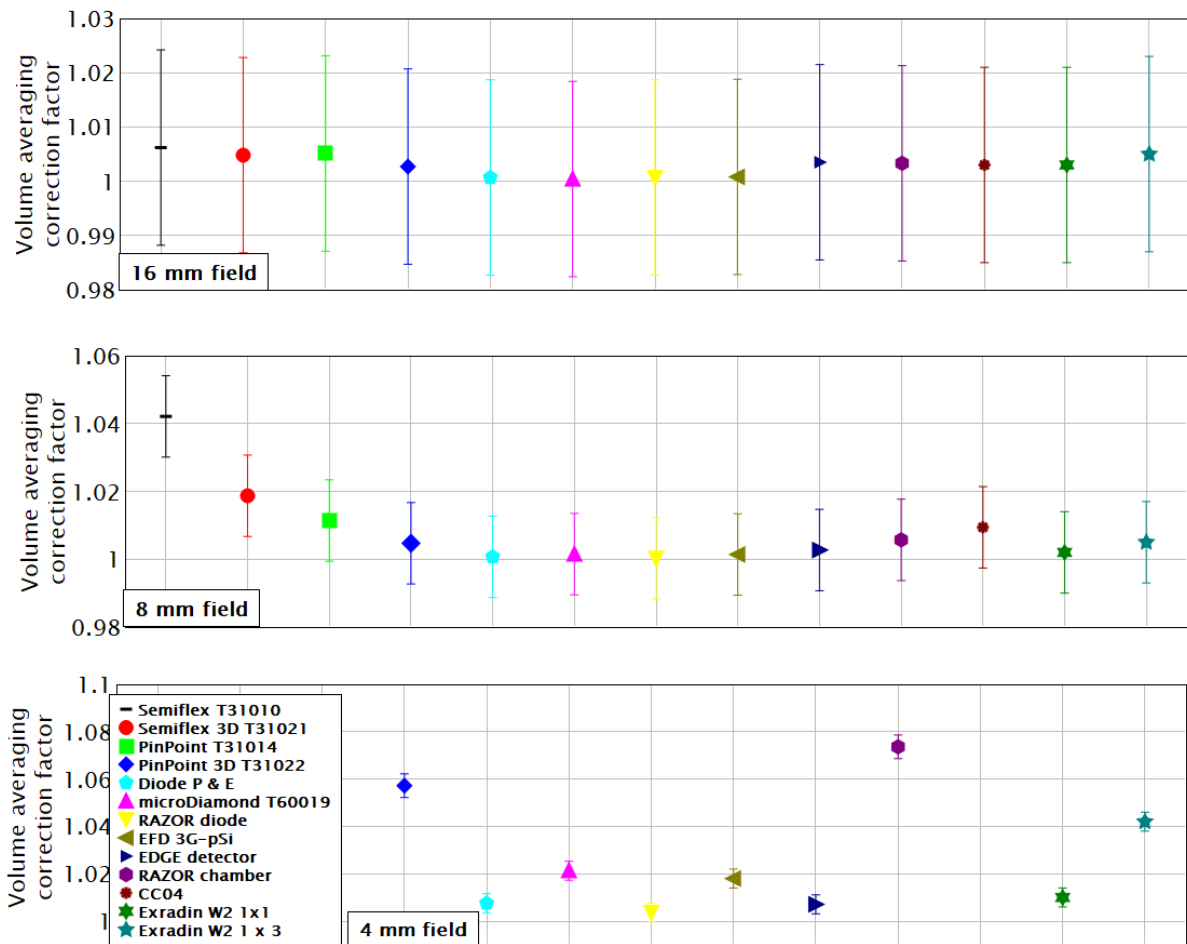
Figure 32. Volume-averaging correction factors $(k_{vol})_{Q_0}^{f_{msr,clin}}$ in msr and clin fields for a different detector with uncertainties $\sigma_{(k_{vol})_{Q_0}^{f_{msr,clin}}}$. Diode P T60016 and Diode E T60017 are represented by one data point since their effective volumes are identical. Detectors with volume-averaging correction factors larger than 1.1 are excluded from 4 mm field graph for better graph readability.

From the theory it is expected that for all detectors volume-averaging correction factor will decrease with the increase of the field size and any deviations from this are due to the imperfection in the ellipsoid absorbed dose model. This explains why Diode P T60016, Diode E T60017, microDiamond T60019, RAZOR diode, EDGE detector and Exradin W2 1x1 have larger volume-averaging correction factor for 16 mm field size than for 8 mm field (Table 16.). This increase in the volume-averaging for larger field size is rather small and can be neglected (Table 16.).

Presented results (Table 16. and Figure 32.) confirm that ionization chambers have a larger volume-averaging correction factor than other types of detectors due to the size of their effective volume. Semiflex T31010, a reference class ionization chamber, has the largest volume-averaging correction factor for all field sizes (V=125 mm$^2$), followed by Semiflex 3D T31021 (V=70 mm$^3$); 1.006, 1.042, 1.627, and 1.005, 1.019, 1.304 for 16 mm, 8 mm, and 4 mm field respectively. Although it has a larger volume, PinPoint 3D T31022 has lover volume-averaging correction than PinPoint T31014 (16 mm$^3$ vs. 15 mm$^3$) for all field sizes. This is due to the geometry of these chambers where PinPoint T31014 is longer and narrower, and PinPoint 3D T31022 is more compact. A length-to-diameter ratio R, is 2.5 and 1.23 for PinPoint and PinPoint 3D respectively. Positioning the detector with its long axis in the z direction makes it more influenced by the asymmetry, and dose gradient of the z-axis dose profile over its volume, therefore, increasing the volume-averaging correction factor (Figure 33.). Importantly, the z-dose profile also has the lowest FWHM value (Figure 29.). By contrast, at the radial dimensions of these chambers x, and y-axis dose profiles are identical, therefore they could not be the reason behind the difference in volume-averaging (Figure 34.). Moreover, the radius of examined chambers is similar therefore the difference in the volume-averaging must be because of the z-axis dose profile. The larger volume-averaging correction factor at the 16 mm field compared with the 8 mm field for some detectors is because of the lower accuracy of the model for that field size (Figure 31.) with a difference of around 0.1% (Table 16.). For a 4 mm field size, IBA CC04 has volume-averaging comparable with PinPoint although its effective volume is almost three times larger (Table 16.). Again, this is due to the longer effective volume in the z-direction of PinPoint T31014 than IBA CC04 (5 mm compared to 3.6 mm) as shown in Table 16. i.e., IBA CC04 is a more compact chamber with an active length-to-diameter ratio equal to 0.9. These results are in line with the similar findings of investigation on detector-specific correction factor with respect to different orientation in high-energy X-ray beams.[55]

RAZOR chamber is the most compact ionization chamber in this study with an effective volume of 10 mm$^3$ and, as a result, it has the smallest volume-averaging correction factor out of all ionization chambers, for all field sizes. RAZORnano chamber has a unique semi-spherical shape with 3 mm$^3$ of an effective volume. Modelling such geometry inside ellipsoid absorbed dose

model resulted in significant uncertainties in volume averaging correction factor, therefore, it was left out of this research.
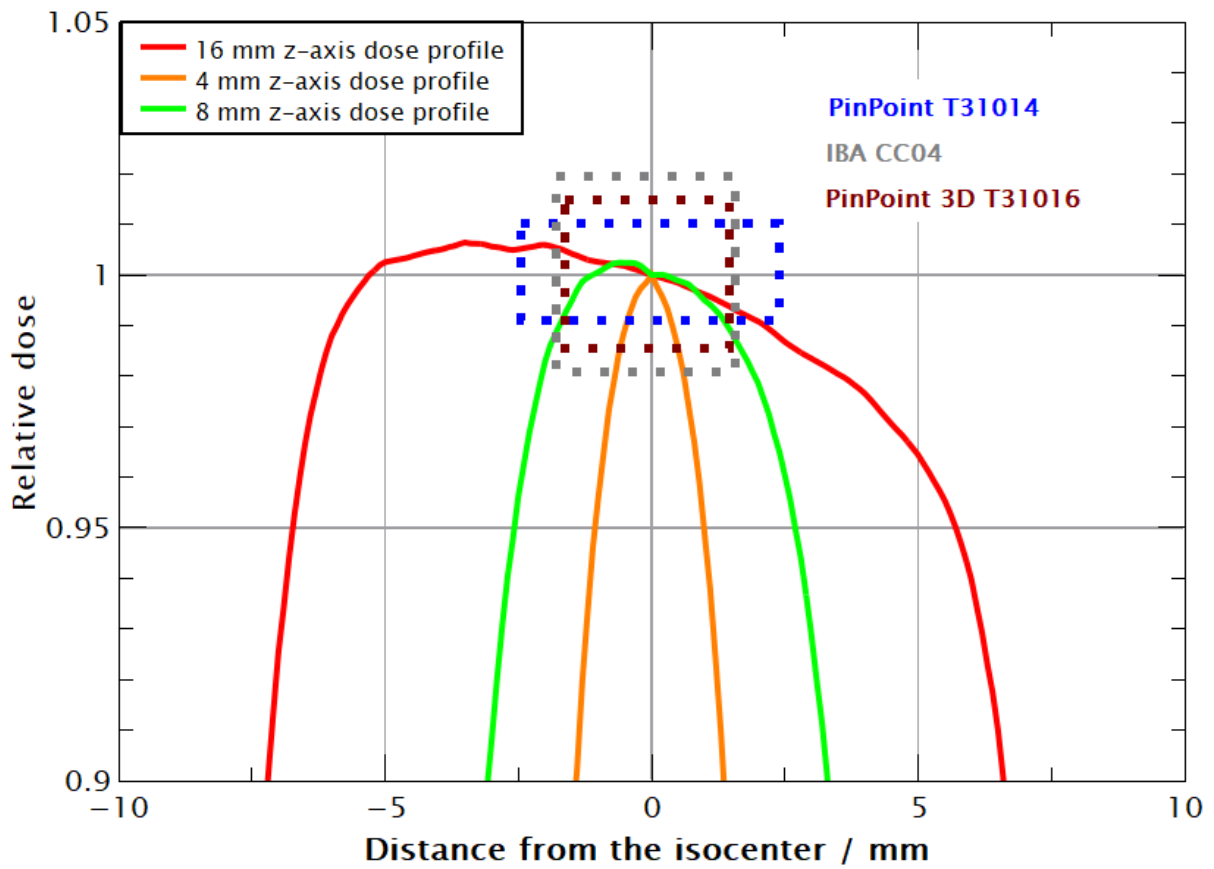


Figure 33. The relative dose profiles on the z-axis with geometries of three detectors. The gradient on the z-axis, for detectors that are longer, creates an increase in the volume-averaging correction factor. Dose profiles are normalized at z=0 mm.
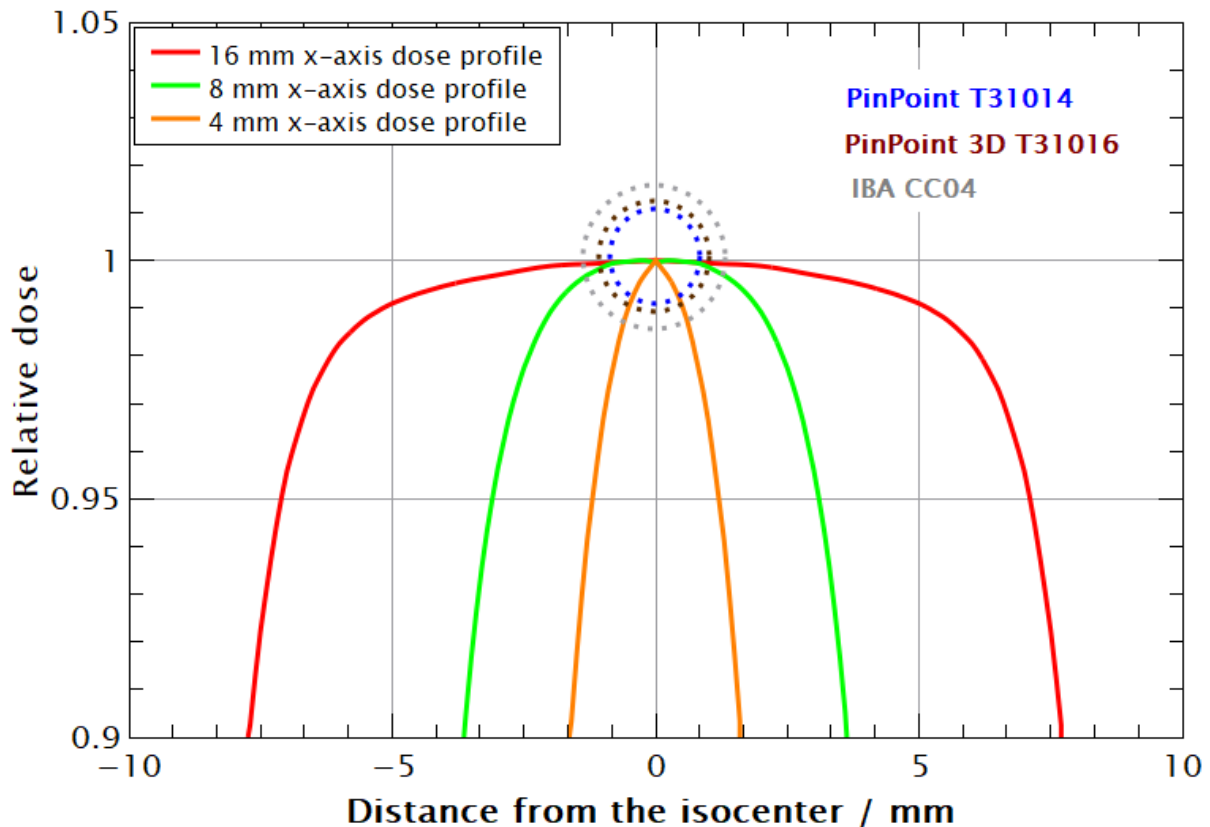
Figure 34. The relative dose profiles on the x-axis with geometries of three detectors. The gradient on the z-axis more influences detectors that are longer creating an increase in the volume-averaging correction factor. Dose profiles are normalized at x=0 mm.

There is an open issue whether the detectors should be placed in a phantom parallel or perpendicular to the x-axis when performing dosimetry of Gamma Knife's narrow photon beams. Therefore, an investigation related to the proper orientation of the detector in the phantom with respect to the volume-averaging should be performed. Since the z-axis dose profile contributes the most to volume-averaging, a detector orientation perpendicular to the z-axis should be considered to limit its influence. However, some studies using Monte Carlo simulations have calculated detector-specific correction factors for the ionization chambers that were placed parallel and perpendicular to the z-axis in the ABS and solid water phantom. Lower detector-specific correction factors were found in the parallel orientation.[90] Although relevant for the dosimetry in small fields, for dose profile measurements our research into volume-averaging indicated that positioning detectors perpendicular to the scanning dose profile is better since volume-averaging is the only effect influencing these types of

measurements. A difference in the geometries of the detector placement in the ABS and solid water phantom can be seen in Figure 35.
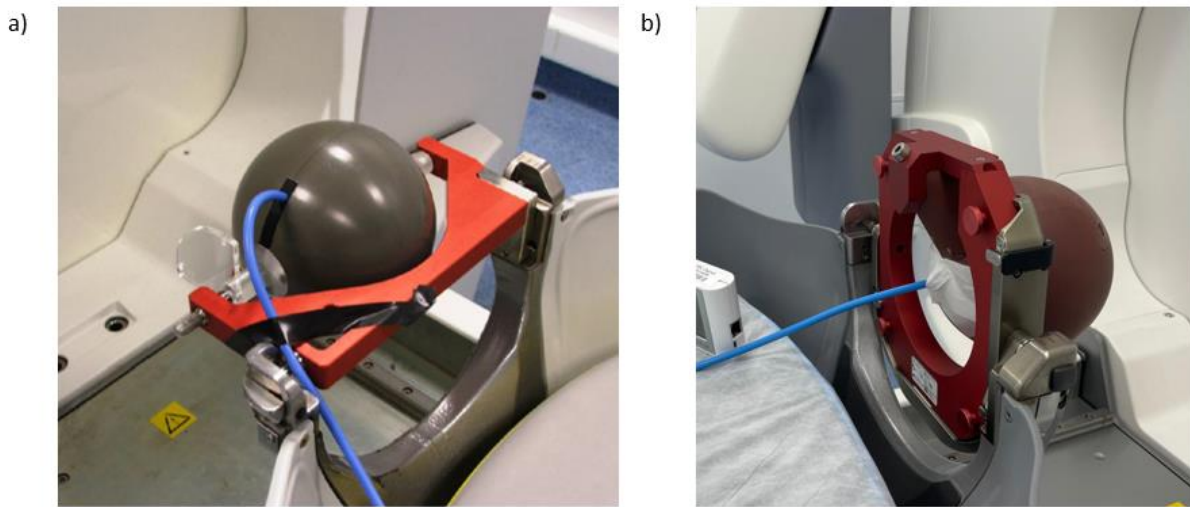


Figure 35. Measuring geometries on Gamma Knife a) dosimetry in ABS phantom with detector places in XY plane perpendicular to the z- axis, and, b) detector in solid water phantom positioned parallel to the z-axis.

Due to the small size of an effective volume and consequently smaller volume-averaging effect, semiconductor detectors are the ideal type of detectors for dosimetry in small fields.[20] This fact is supported by this study for a large majority of explored semiconductor detectors. The single exception is the EFD diode which has a relatively large volume (0.16 mm$^3$), therefore the correction factor for the 4 mm field size is 1.018. Diode E T60016 and Diode P T60017 have equal volume-averaging correction factors since their effective volumes are identical, and the only difference is shielding for the filtration of low-energy photons. The microDiamond T60019 is characterized by the smallest volume out of all studied detectors, however, its correction factor for the 4 mm field is relatively large being 1.021. This is due to the shape of its effective volume. It is unique in a way that it is a very thin (1 µm) disk with a large diameter of 2.2 mm. This design makes it more sensitive to dose gradients in the XY plane which starts to be noticeable at a 4 mm field increasing the correction for volume-averaging. From this, one can see that although the magnitude of the detector's effective volume is important, when it comes to dosimetry of GK narrow photon beams, the shape of that volume also has an important role. More precisely, the length-to-diameter ratio of a detector has s fundamental role in volume averaging correction factor[55]. The manufacturer denotes plastic

scintillator detectors Exradin W2 1x1 and 1x3 as perturbation-free detectors since they are tissue–equivalent. However, the effect of volume-averaging could not be neglected for them (Table 16.). In addition, following IAEA TRS-483 CoP we have selected detectors that are not suitable for dosimetry of Gamma Knife Perfexion photon beams according to their volume-averaging correction factor. Therefore, Semiflex T31010, Semiflex 3D T31021, PinPoint T31014, PinPoint 3D T31022, CC04, and RAZOR chamber are not recommended for dosimetry in 4 mm field since their volume-averaging correction factor is larger than 1.05 (Table 16.). Finally, we have calculated the contribution of the volume-averaging correction factor in the field output correction factor $k_{\%vol}$ for detectors listed in IAEA TRS-483 CoP. For all studied detectors, volume-averaging is a dominant perturbation (Table 18). For the semiconductor detectors, the volume-averaging contribution is larger than the total field output correction factor. This is expected since they over-respond to low energy scattered photons and their total correction factors are lower than 1.000 due to the fluence perturbations of these detectors.

A volume-averaging perturbation correction factor $(k_{vol})_{Q_0,Q_0}^{f_{msr},f_{clin}}$ calculated (Equation 4.11.) for the detectors that are listed in IAEA TRS-483 CoP and the results are shown in Table 17. As previously, detectors that are marked with red are not suitable for dosimetry at that field size.

| Detector name | $(k_{vol})_{Q_0,Q_0}^{f_{msr},f_{clin}}$ | | |
|---|---|---|---|
| | **16 mm** | **8 mm** | **4 mm** |
| **Semiflex T31010** | 1.000 | 1.036±0.022 | <span style="color:red">1.617±0.007</span> |
| **Semiflex 3D T31021** | 1.000 | 1.014±0.022 | <span style="color:red">1.298±0.006</span> |
| **PinPoint T31014** | 1.000 | 1.006±0.022 | <span style="color:red">1.175±0.005</span> |
| **PinPoint 3D T31022** | 1.000 | 1.001±0.022 | <span style="color:red">1.091±0.005</span> |
| **Diode P T60016** | 1.000 | 0.999±0.022 | 1.007±0.004 |
| **Diode E T60017** | 1.000 | 0.999±0.022 | 1.007±0.004 |
| **microDiamond T60019** | 1.000 | 1.001±0.022 | 1.020±0.004 |
| **RAZOR diode** | 1.000 | 0.999±0.022 | 1.003±0.004 |
| **EFD 3G-pSi** | 1.000 | 1.000±0.022 | 1.017±0.004 |
| **EDGE detector** | 1.000 | 0.999±0.022 | 1.004±0.004 |
| **RAZOR chamber** | 1.000 | 1.003±0.022 | <span style="color:red">1.071±0.005</span> |
| **IBA CC04** | 1.000 | 1.007±0.022 | <span style="color:red">1.147±0.005</span> |
| **Exradin W2 1x1** | 1.000 | 0.999±0.022 | 1.007±0.004 |
| **Exradin W2 1x3** | 1.000 | 1.000±0.022 | 1.037±0.004 |

Table 17. A result of a volume-averaging perturbation in clinical and machine-specific reference fields $(k_{vol})_{Q_0,Q_0}^{f_{msr},f_{clin}}$ for different detectors with uncertainties $\sigma_{(k_{vol})_{Q_0,Q_0}^{f_{msr},f_{clin}}}$. Investigated detectors marked in red are not recommended for dosimetry at that field size according to IAEA TRS-483 CoP guidelines for volume-averaging criteria.[10]

| Detector name | $k_{Q_0,Q_0}^{f_{msr},f_{clin}}$ | | | $k_{\%vol}/\%$ | | |
|---|---|---|---|---|---|---|
| | 16 mm | 8 mm | 4 mm | 16 mm | 8 mm | 4 mm |
| Semiflex T31010 | 1.004 | N.A. | N.A. | 99.6 | N.A. | N.A. |
| PinPoint T31014 | 1.000 | 1.030 | N.A. | 100.0 | 98.4 | N.A. |
| Diode P T60016 | 1.000 | 0.981 | 0.965 | 100.0 | 101.8 | 104.4 |
| Diode E T60017 | 1.000 | 0.996 | 0.985 | 100.0 | 100.3 | 102.2 |
| microDiamond T60019 | 1.000 | 1.005 | 0.993 | 100.1 | 99.6 | 102.9 |
| IBA CC04 | 1.021 | N.A. | N.A. | 97.9 | N.A. | N.A. |

Table 18. Field output correction factors $k_{Q_0,Q_0}^{f_{msr},f_{clin}}$ from IAEA TRS-483 CoP and contribution of volume-averaging perturbation to a total correction $k_{\%vol}$ for different detectors. N.A. stands for not available in IAEA TRS-483 CoP.

## 5.5. Field output factors and detector-specific correction factors

A set of EBT3 film irradiated in the XY plain with different doses using a 16 mm field size for creation of a calibration curve can be seen in Figure 36.
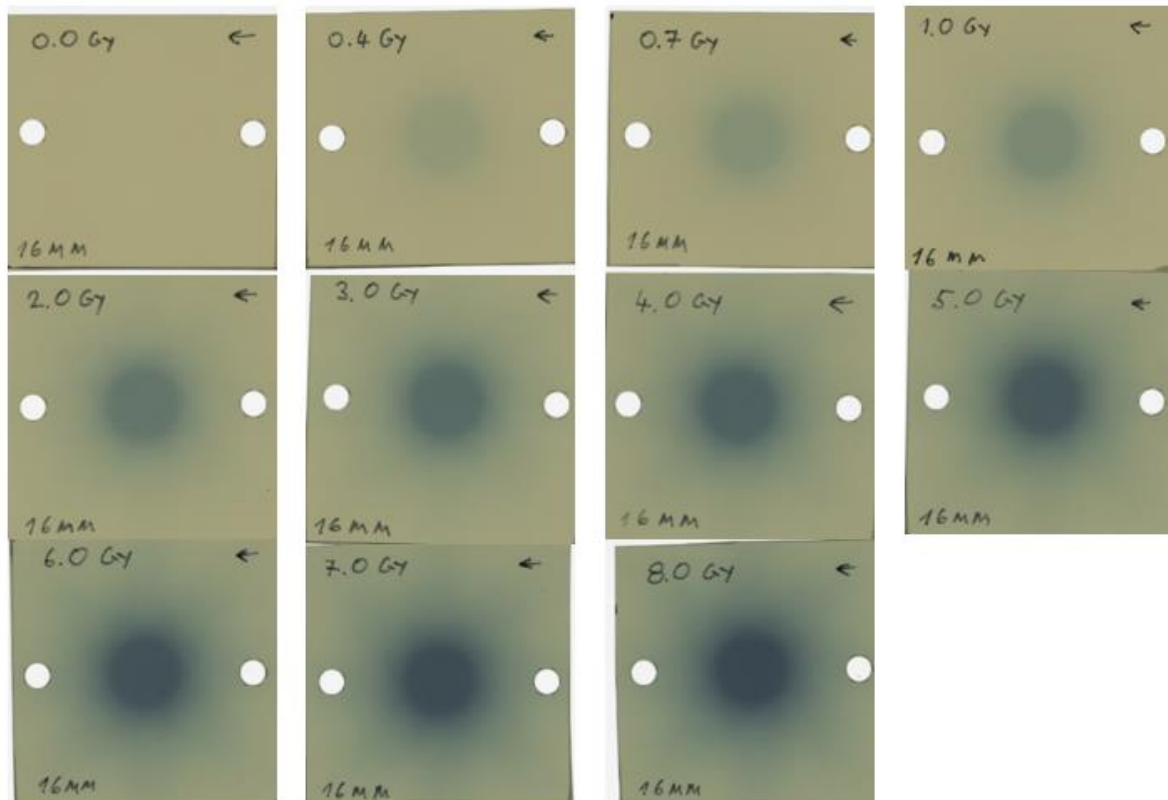


Figure 36. EBT3 films irradiated in the XY plane with different absorbed doses for creation of a calibration curve.

The calibration curve using Dević fit function relating netOD with an absorbed dose can be seen in Figure 37. with fit values in Table 19.
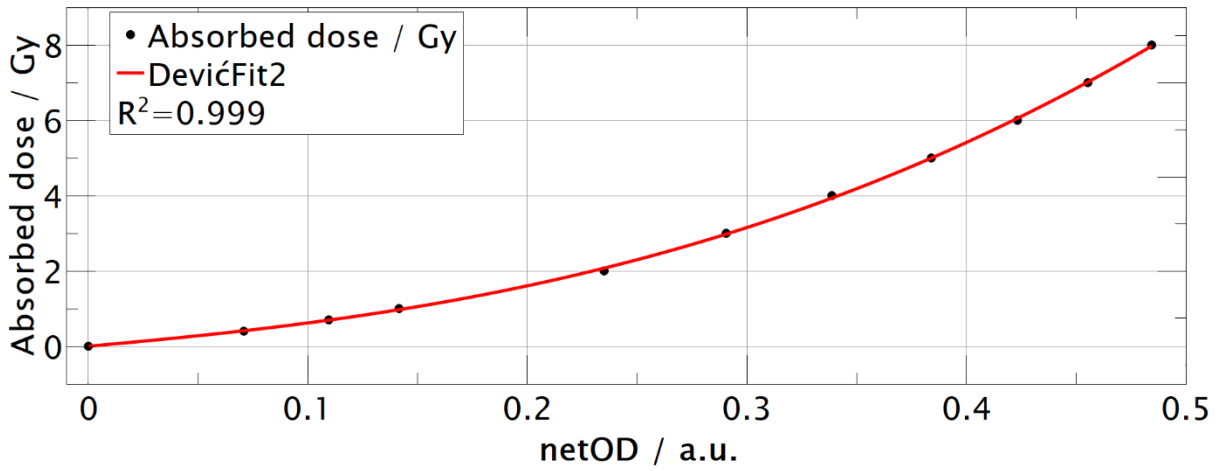
Figure 37. Calibration curve for EBT3 films.

| Coefficients | Value | Uncertainties |
|:---:|:---:|:---:|
| a | 5.17 | 0.20 |
| b | 35.30 | 2.17 |
| n | 2.514 | 0.088 |
| $D(netOD) = a \cdot netOD + b \cdot netOD^n$ | | |

Table 19. Fit coefficients for EBT3 calibration curve.

Films irradiated for the determination of field output factors are presented in Figure 38. Field output factor $\Omega_{Q_0,Q_0}^{f_{clin},f_{msr}}$ were determined on ROI: 4, 2, and 0.8 mm for 16 mm, 8 mm and 4 mm field size respectively. Since EBT3 film is considered perturbation free, the detector-specific correction factor is equal to one, field output factors were determined by converting the mean pixel value on ROI to absorbed dose and by dividing the absorbed dose in the clinical field with dose in msr field using $\Omega_{Q_0,Q_0}^{f_{clin},f_{msr}} = \dfrac{D_{w,Q_0}^{f_{clin}}}{D_{w,Q_0}^{f_{msr}}}$. Result of field output factors and its difference from Monte Carlo calculated values[20], values are presented in Table 20.
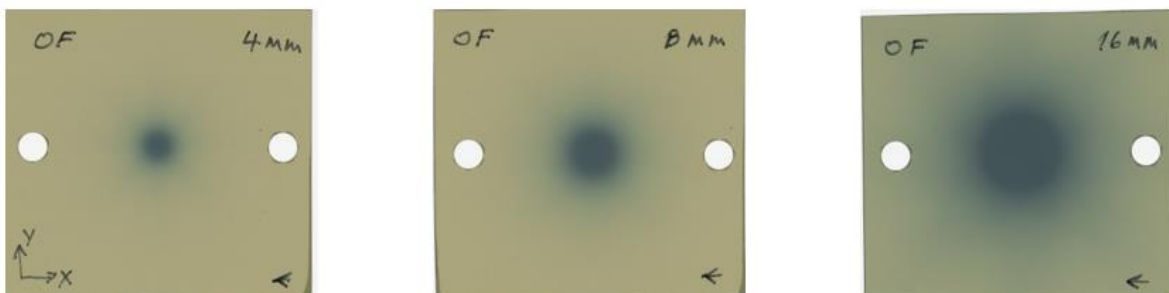


Figure 38. EBT3 films irradiated 2.69 minutes in XY plane for field output factor determination.

| Field size / mm | $\left(\Omega_{Q_0,Q_0}^{f_{clin},f_{msr}}\right)_{EBT3}$ | $\left(\Omega_{Q_0,Q_0}^{f_{clin},f_{msr}}\right)_{MC}$ | EBT3 diff. from MC / % |
|:---:|:---:|:---:|:---:|
| 4 | 0.826±0.064 | 0.814 | 1.474 |
| 8 | 0.889±0.053 | 0.900 | -1.222 |

Table 20. Field output factors $\Omega_{Q_0,Q_0}^{f_{clin},f_{msr}}$ determined using EBT3 film, Monte Carlo[20] simulations and difference of EBT3 values from Monte Carlo calculated values.

Field output factors determined using EBT3 film have shown a good agreement with the Monte Carlo calculated values, with a mean absolute difference of less than 2%. However, it should be pointed out that field output factors determined with the EBT3 film have uncertainty up to 6% due to the noise and postirradiation handling (Table 11.).[17,42,43,76]

To analyse the performance of different detectors in narrow Co-60 beams, field output factors are determined with twelve different detectors. The results of such measurements are presented in Table 21. Comparison analysis of field output factors obtained with the active detectors and the ones obtained with the EBT3 film and Monte Carlo is presented in Table 22., together with the calculated detectors specific field output correction factors $k_{Q_0,Q_0}^{f_{clin},f_{msr}}$.

| Detector name / Field size / mm | $M_{Q_0}^{f\,msr,clin} / nC$ | | | $\Delta M_{Q_0}^{f\,msr,clin} / nC$ | | | $\Omega_{Q_0,Q_0}^{f_{clin},f_{msr}} \pm \sigma_{\Omega_{Q_0,Q_0}^{f_{clin},f_{msr}}}$ | | |
|---|---|---|---|---|---|---|---|---|---|
| | 16 | 8 | 4 | 16 | 8 | 4 | 16 | 8 | 4 |
| Semiflex T31010 | 7.273 | 5.717 | 2.430 | 0.077 | 0.083 | 0.048 | 1.000 | 0.786±0.014 | 0.334±0.007 |
| Semiflex 3D T31021 | 3.669 | 3.131 | 1.645 | 0.040 | 0.046 | 0.032 | 1.000 | 0.854±0.016 | 0.449±0.010 |
| PinPoint T31014 | 0.913 | 0.799 | 0.580 | 0.010 | 0.012 | 0.011 | 1.000 | 0.877±0.016 | 0.636±0.014 |
| PinPoint 3D T31016 | 0.856 | 0.756 | 0.578 | 0.009 | 0.011 | 0.011 | 1.000 | 0.880±0.016 | 0.675±0.015 |
| RAZOR chamber | 0.596 | 0.528 | 0.433 | 0.005 | 0.007 | 0.008 | 1.000 | 0.885±0.014 | 0.726±0.015 |
| RAZORnano chamber | 0.208 | 0.187 | 0.170 | 0.034 | 0.031 | 0.026 | 1.000 | 0.900±0.022 | 0.815±0.023 |
| IBA CC04 | 1.972 | 1.716 | 1.140 | 0.001 | 0.002 | 0.003 | 1.000 | 0.870±0.012 | 0.578±0.011 |
| Diode P T60016 | 20.568 | 18.676 | 17.548 | 0.328 | 0.352 | 0.333 | 1.000 | 0.908±0.022 | 0.853±0.024 |
| Diode E T60017 | 21.428 | 19.131 | 18.139 | 0.348 | 0.365 | 0.420 | 1.000 | 0.893±0.022 | 0.847±0.024 |
| RAZOR diode | 7.549 | 6.774 | 6.397 | 0.088 | 0.102 | 0.127 | 1.000 | 0.897±0.017 | 0.847±0.020 |
| EDGE detector | 57.490 | 51.070 | 48.790 | 0.587 | 0.730 | 0.946 | 1.000 | 0.888±0.016 | 0.849±0.019 |
| microDiamond T60019 | 2.254 | 1.997 | 1.851 | 0.033 | 0.035 | 0.041 | 1.000 | 0.886±0.020 | 0.821±0.022 |

Table 21. Results of an average detector's response in clinical and machine-specific reference fields $M_{Q_0}^{f\,msr,clin}$, a calculated value of signal uncertainty $\Delta M_{Q_0}^{f\,msr,clin}$ (Table 14.), uncorrected field output factors $\Omega_{Q_0,Q_0}^{f_{clin},f_{msr}}$ with total uncertainties $\sigma_{\Omega_{Q_0,Q_0}^{f_{clin},f_{msr}}}$.
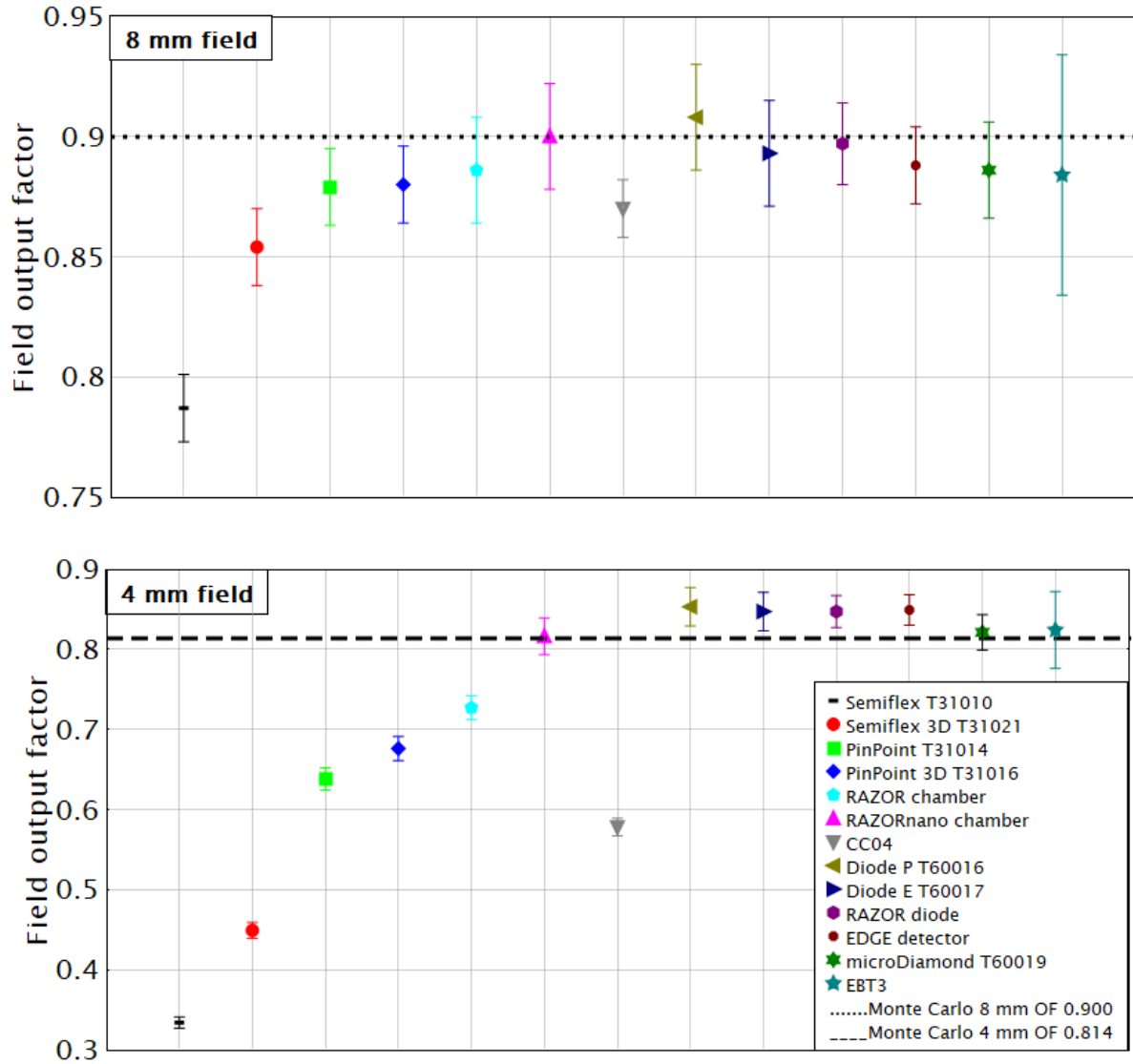
Figure 39. Results of uncorrected field output factors $\Omega_{Q_0,Q_0}^{f_{clin},f_{msr}}$ for all investigated detectors with uncertainties $\sigma_{\Omega_{Q_0,Q_0}^{f_{clin},f_{msr}}}$ in 8, and 4 mm field. Dotted and dashed lines represent Monte Carlo values for 8 mm field (0.900) and 4 mm field (0.814) respectively.

| Detector name | $\Omega_{Q_0,Q_0}^{f_{clin},f_{msr}}$ | | $\Omega_{Q_0,Q_0}^{f_{clin},f_{msr}}$ diff. from MC / % | | $\left(k_{Q_0,Q_0}^{f_{msr},f_{clin}}\right)_{MC} \pm \sigma_{\left(k_{Q_0,Q_0}^{f_{msr},f_{clin}}\right)_{MC}}$ | | $\Omega_{Q_0,Q_0}^{f_{clin},f_{msr}}$ diff. from EBT3 / % | | $\left(k_{Q_0,Q_0}^{f_{msr},f_{clin}}\right)_{EBT3} \pm \sigma_{\left(k_{Q_0,Q_0}^{f_{msr},f_{clin}}\right)_{EBT3}}$ | |
|---|---|---|---|---|---|---|---|---|---|---|
| Field size / mm | 8 | 4 | 8 | 4 | 8 | 4 | 8 | 4 | 8 | 4 |
| Semiflex T31010 | 0.786 | 0.334 | -12.6 | -58.9 | 1.145±0.021 | 2.436±0.054 | -11.5 | -59.6 | 1.131±0.054 | 2.470±0.130 |
| Semiflex 3D T31021 | 0.854 | 0.449 | -5.1 | -44.8 | 1.054±0.019 | 1.814±0.041 | -3.9 | -45.6 | 1.041±0.050 | 1.840±0.093 |
| PinPoint T31014 | 0.877 | 0.636 | -2.3 | -21.7 | 1.026±0.018 | 1.279±0.028 | -1.1 | -22.8 | 1.013±0.049 | 1.298±0.066 |
| PinPoint 3D T31016 | 0.880 | 0.675 | -2.2 | -17.0 | 1.023±0.019 | 1.205±0.027 | -1.0 | -18.2 | 1.010±0.049 | 1.223±0.062 |
| RAZOR chamber | 0.885 | 0.726 | -1.6 | -10.7 | 1.016±0.016 | 1.121±0.023 | -0.3 | -12.0 | 1.004±0.046 | 1.137±0.054 |
| RAZORnano chamber | 0.900 | 0.816 | 0 | 0.2 | 1.000±0.025 | 0.998±0.028 | 1.2 | -1.2 | 0.988±0.047 | 1.013±0.050 |
| IBA CC04 | 0.870 | 0.578 | -3.2 | -29.0 | 1.034±0.014 | 1.408±0.026 | -2.1 | -30.0 | 1.022±0.047 | 1.428±0.068 |
| Diode P T60016 | 0.908 | 0.853 | 0.9 | 4.8 | 0.991±0.024 | 0.954±0.027 | 2.1 | 3.3 | 0.979±0.047 | 0.968±0.049 |
| Diode E T60017 | 0.893 | 0.847 | -0.8 | 4.0 | 1.008±0.025 | 0.962±0.027 | 0.4 | 2.5 | 0.996±0.048 | 0.976±0.050 |
| RAZOR diode | 0.897 | 0.847 | -0.3 | 4.1 | 1.003±0.019 | 0.961±0.022 | 0.9 | 2.5 | 0.991±0.048 | 0.975±0.050 |
| EDGE detector | 0.888 | 0.849 | -1.3 | 4.3 | 1.013±0.018 | 0.959±0.021 | -0.1 | 2.8 | 1.001±0.048 | 0.973±0.050 |
| microDiamond T60019 | 0.886 | 0.821 | -1.6 | 0.9 | 1.016±0.023 | 0.991±0.026 | -0.3 | -0.6 | 1.003±0.048 | 1.006±0.051 |

Table 22. Results in difference in uncorrected field output factors $\Omega_{Q_0,Q_0}^{f_{clin},f_{msr}}$ and detector-specific field output correction factor $k_{Q_0,Q_0}^{f_{msr},f_{clin}}$ with their uncertainties for different detectors when compared with Monte Carlo and EBT3 film values. Result are rounded to the second significant digit.

For the discussion of data from Table 22., detectors will be subdivided into two groups; firstly, ionization chambers will be discussed and then the remaining detectors. Similarly, the results of the field output factors for the 4 mm field will be discussed first since all perturbation effects are noticeable at that field size, afterwards, the results for the 8 mm field will be examined. Differences in field output factors determined using active detectors from values determined with the EBT3 film and Monte Carlo are due to three effects that add up, these are: lack of lateral charged particle equilibrium, over-response/under-response of high/low Z material, and volume-averaging effect.

## 5.5.1. Field output factors of Gamma Knife's 4 mm field

Results of a field output factors $\Omega_{Q_0,Q_0}^{f_{clin},f_{msr}}$, for 4 mm field, obtained with the ionization chambers; Semiflex T31010 (V=125 mm$^3$), Semiflex 3D T31021 (V=70 mm$^3$), PinPoint T31014 (V=15 mm$^3$), PinPoint 3D T31016 (V=16 mm$^3$), RAZOR chamber (V=10 mm$^3$) and CC04 (V=40 mm$^3$) shown a substantial difference both from the Monte Carlo and EBT3 values (Table 18.). For all mentioned detectors field output factors are underestimated in a range of -60% for Semiflex T31010 to -12% for the RAZOR chamber. Moreover, the underestimation of a response is directly proportional to the size of a chamber with RAZORnano chamber, with the smallest volume (V=3 mm$^3$), having the best result. For these detectors, in 4 mm field size, all the abovementioned perturbations have a part in the resulting underestimation of field output factors. Loss of charged particle equilibrium is one of those reasons. Presented data (Table 15.) shows that the field must expand at least 3.883 mm from the chamber's edges (Figure 7.) to preserve CPE in water for C0-60 beams. For all studded detectors, in 4 mm field, this condition in not fulfilled. The second perturbation is the significant volume-averaging effect $(k_{vol})_{Q_0,Q_0}^{f_{msr},f_{clin}}$ (Table 17.) All ionization chambers, except the RAZORnano chamber, have large effective volumes relative to the size of a 4 mm field. Because of this, the detector will average its signal over the volume, resulting in a decrease in measured detector response. This is most noticeable for the largest chambers such as Semiflex, Semiflex 3D and CC04 with differences of -58.9%, -44.8% and -29.0% respectively, compared to the Monte Carlo values. They have the largest detector-specific correction factors $k_{Q_0,Q_0}^{f_{msr},f_{clin}}$ and volume-averaging is

one of the main reasons behind this difference (Table 17.). Ionization chambers presented in this study, except RAZORnano, are not recommended for dosimetry of Gamma Knife's 4 mm field because of the extreme perturbations that they demonstrate. RAZORnano chamber is the best performing one with 0.2% and -1.2% difference from field output factor determined with Monte Carlo and EBT3 films respectively (Table 22.). This is expected since it has the smallest effective volume which will result in lower volume averaging regardless of the loss of CPE (Table 15.).

The next group of detectors include remaining semiconductor detectors as well as a diamond detector. For these detectors, volume-averaging is negligible due to its small volume. Volume-averaging correction factors $(k_{vol})_{Q_0,Q_0}^{f_{msr},f_{clin}}$ calculated for these detectors and are given in Table 16. In addition, in the 4 mm field size, loss of CPE is present for semiconductor and diamond detectors and should be taken into consideration (Table 15.) However, due to the smaller dimensions of an effective volumes of these detectors one can expect that loss of CPE is not significant as with ionization chambers. It should be emphasised that all semiconductor detectors and diamond detector show a better agreement with the field output factor $\Omega_{Q_0,Q_0}^{f_{clin},f_{msr}}$ determined with the EBT3 film than with the Monte Carlo determined values. Similar studies support these conclusions.[20] Moreover, all semiconductor detectors over-responded in a 4 mm field. This is due to the high atomic number of silica Z=14, compared with the effective atomic number of the water Zeff=7.42. Furthermore, semiconductor detectors will additionally over-respond to the low energy scattered photon (Figure 16.). This effect is not emphasized as much in narrow beam geometries of Gamma Knife's collimating system due to the lack of low energy photons, however, it is the reason behind the difference in field output factors between Diode P and E (0.966 and 0.973). They are identical detectors, except for the fact that Diode P has a high density shielding of its effective volume that filters out the low-energy photons. Therefore, Diode P will overrespond by 4.8% and 3.3%, and Diode E by 4.0% and 2.5% when the field output values are compared with the Monte Carlo and EBT3 film for 4 mm field size. In general, Diode E is better suited for the dosimetry of narrow photon beams used by Gamma Knife. Unshielded RAZOR diode and EDGE detector have their detector-specific correction factors close to the ones obtained with Diode E (0.973 and 0.971).

From all detectors used for dosimetry of 4 mm field size, the microDiamond detector has shown the best agreement with the Monte Carlo and EBT3 film results. It is characterised by the small effective volume, high dose-response and tissue equivalence. Therefore, it has the lowest perturbation of all detectors resulting in the detector-specific correction factor being close to unity (Table 22.).[16] From these results, we can conclude that microDiamond T60019 is the best-performing detector in dosimetry of 4 mm Gamma Knife's field.

## 5.2.2. Field output factors of Gamma Knife's 8 mm field.

The results of field output factors $\Omega_{Q_0,Q_0}^{f_{clin},f_{msr}}$ determined for the 8 mm field are presented in Table 22. All investigated ionization chambers have loss of charged particle equilibrium (Table 15.) and high volume-averaging (Table 16.). CPE is not violated for semiconductor detectors. Diamond detectors violets CPE only if positioned perpendicular to the device's z-axis due to large diameter of its effective volume. Volume-averaging correction $(k_{vol})_{Q_0,Q_0}^{f_{msr},f_{clin}}$ for semiconductor and diamond detector in an 8 mm field is negligible. The result of field output factors obtained with the ionization chambers still show a significant difference from the reference values. On the other hand, for small-volume chambers this difference is low, so they can be used for dosimetry of such field sizes. Semiflex T31010 and Semiflex 3D T31021 still have large differences from the Monte Carlo values and are underestimating field output factors by 12.6% and 5.1%, respectively. They are not suited for the dosimetry in an 8 mm field size.  On the other hand. PinPoint, PinPoint 3D and RAZOR chamber have shown a good agreement with the EBT3 film with all underestimating field output factor by less than 1.1%. CC04 has a difference in field output factor values of -3.2% and -1.1% from Monte Carlo and EBT3 film values. All ionization chambers have better agreement with the EBT3 film than with the Monte Carlo, except for the RAZORnano chamber, which over-responded by 1.2% when compared with the EBT3 film.

Field output factors determined with Diode P and RAZOR diode are closer in value to Monte Carlo values, while the remaining semiconductor detectors are more consistent with the EBT3 film results. Overresponse of Diode P and RAZOR diode is due to high density shielding of its effective volume. This can explain why they are ones of the few detectors with their values

closer to Monte Carlo results. Diode E and EDGE have similar values of detector-specific correction factor $k_{Q_0,Q_0}^{f_{msr},f_{clin}}$, when compared to the EBT3 film, being 0.996 and 1.001, respectively. For 8 mm field, ionization chambers have their field output factors in better agreement with the Monte Carlo values. As previously, microDiamond has shown a good agreement with reference EBT3 film values with a correction factor close to unity, 1.003, for 8 mm field.

In this study of field output factor determination, one can see how different detector types behave in different field sizes. Ionization chambers are well-established detectors with an excellent signal-to-noise ratio, however, most of them are not suitable for the dosimetry of small fields.[12,13,20,26,33] This is due to loss of charged particle equilibrium (Table 15.) and high volume-averaging effect in such fields (Table 16.). Semiconductor detectors are a good selection for small field dosimetry, however, they do have perturbations that must be appropriately considered.[13,16,17]. The diamond detector has outperformed all detectors with values closest to the reference ones due to its properties.[17,27,73] Furthermore, most of the detectors agree better in results with the EBT3 films than with the Monte Carlo values. One should keep in mind that uncertainties in the field output factors determined with the EBT3 film are larger than with the active detectors (Table 11. and Table 12.).

## 5.6. Gamma Knife's Perfexion dose profiles

Different detector will provide dose profile data which may differ significantly. The main cause is the volume-averaging. An increase in detector volume-averaging with a decrease in the size of a dose profile can be seen on all z-axis dose profiles when compared with the dose profiles on x and y - axis for a given field size. The effect is more emphasized as field is decreased down to 4 mm. It is obvious from the Figure 40. to Figure 48. that the relative dose is underestimated in the region of 100-50% of the relative dose and overestimated for the rest of the profile. This is because the volume averaging is proportional to the second derivative of a dose profile. Where a second derivative of dose profile is lower than zero, the detector will underestimate absorbed dose. Similarly, if the value of a second derivative is large than zero, the detector will overestimate the absorbed dose. In inflection points, there is no volume averaging.[51]

The plotted dose profiles determined with different detectors are shown from Figure 40. to Figure 48. Results of an analysis of determined dose profile with different detectors are shown from Table 23. to Table 26., and from Figure 49. to Figure 51.

| Detector | Profile | LP / mm | RP / mm | FWHM / mm | LP diff. from MC / mm | RP diff. from MC / mm | FWHM diff. from MC / mm | Mean dose gradient LP / % per mm | Mean dose gradient RP / % per mm |
|---|---|---|---|---|---|---|---|---|---|
| Monte Carlo | 16 x | 9.02 | 9.03 | 21.75 | | | | 6.65 | 6.65 |
| | 16 y | 9.02 | 9.02 | 21.75 | | | | 6.65 | 6.65 |
| | 16 z | 2.30 | 2.83 | 17.48 | | | | 26.13 | 21.24 |
| | 8 x | 3.95 | 3.95 | 11.06 | | | | 15.20 | 15.20 |
| | 8 y | 3.95 | 3.95 | 11.06 | | | | 15.20 | 15.19 |
| | 8 z | 2.36 | 2.21 | 9.80 | | | | 25.47 | 27.11 |
| | 4 x | 2.82 | 2.82 | 6.16 | | | | 21.25 | 21.25 |
| | 4 y | 2.82 | 2.82 | 6.16 | | | | 21.25 | 21.25 |
| | 4 z | 1.49 | 1.54 | 5.04 | | | | 40.30 | 39.06 |
| PinPoint T31014 | 16 x | 9.05 | 9.00 | 21.29 | 0.02 | -0.03 | -0.46 | 6.63 | 6.67 |
| | 16 y | 9.45 | 9.39 | 21.49 | 0.43 | 0.37 | -0.26 | 6.35 | 6.39 |
| | 16 z | 3.87 | 4.16 | 17.53 | 1.57 | 1.34 | 0.05 | 15.52 | 14.41 |
| | 8 x | 4.67 | 4.63 | 10.62 | 0.72 | 0.69 | -0.43 | 12.86 | 12.95 |
| | 8 y | 4.69 | 4.65 | 10.67 | 0.74 | 0.70 | -0.39 | 12.79 | 12.90 |
| | 8 z | 3.76 | 3.77 | 9.77 | 1.41 | 1.56 | -0.03 | 15.95 | 15.90 |
| | 4 x | 3,74 | 3.72 | 6.23 | 0.91 | 0.90 | 0.070 | 16.06 | 16.13 |
| | 4 y | 3.76 | 3.72 | 6.29 | 0.93 | 0.90 | 0.13 | 15.97 | 16.12 |
| | 4 z | 2.89 | 2.83 | 5.98 | 1.40 | 1.29 | 0.95 | 20.78 | 21.20 |
| PinPoint 3D T31016 | 16 x | 9.27 | 9.30 | 21.66 | 0.25 | 0.28 | -0.10 | 6.47 | 6.450 |
| | 16 y | 9.25 | 9.23 | 21.53 | 0.22 | 0.21 | -0.22 | 6.49 | 6.50 |
| | 16 z | 3.25 | 3.61 | 17.37 | 0.95 | 0.78 | -0.11 | 18.48 | 16.64 |
| | 8 x | 4.72 | 4.68 | 10.92 | 0.77 | 0.73 | -0.13 | 12.71 | 12.84 |
| | 8 y | 4.72 | 4.70 | 10.92 | 0.78 | 0.76 | -0.13 | 12.71 | 12.76 |
| | 8 z | 3.27 | 3.26 | 9.54 | 0.92 | 1.04 | -0.26 | 18.34 | 18.42 |
| | 4 x | 3.72 | 3.67 | 6.49 | 0.90 | 0.85 | 0.33 | 16.14 | 16.34 |
| | 4 y | 3.68 | 3.71 | 6.48 | 0.86 | 0.89 | 0.32 | 16.29 | 16.16 |
| | 4 z | 2.54 | 2.49 | 5.24 | 1.05 | 0.95 | 0.20 | 23.67 | 24.14 |

Table 23. Results of Gamma Knife's Perfexion dose profile measurements obtained with Monte Carlo simulations, PinPoint T31014 and PinPoint 3D T31016 chambers for FWHM, LP (left penumbra) and RP (right Penumbra) values and their difference from Monte Carlo values as well as mean dose gradients in the penumbra region. Values are rounded to one hundredth of a millimetre.

| Detector | Profile | LP / mm | RP / mm | FWHM / mm | LP diff. from MC / mm | RP diff. from MC / mm | FWHM diff. from MC / mm | Mean dose gradient LP / % per mm | Mean dose gradient RP / % per mm |
|---|---|---|---|---|---|---|---|---|---|
| Diode E T60016 | 16 x | 8.72 | 8.55 | 21.62 | -0.30 | -0.48 | -0.13 | 6.88 | 7.02 |
| | 16 y | 9.08 | 9.04 | 21.81 | 0.05 | 0.01 | 0.06 | 6.61 | 6.64 |
| | 16 z | 2.16 | 2.72 | 17.44 | -0.14 | -0.11 | -0.03 | 27.78 | 22.07 |
| | 8 x | 3.89 | 3.83 | 11.05 | -0.06 | -0.12 | -0.01 | 15.44 | 15.67 |
| | 8 y | 3.88 | 3.89 | 11.06 | -0.07 | -0.06 | 0.01 | 15.46 | 15.44 |
| | 8 z | 2.17 | 2.09 | 9.80 | -0.19 | -0.12 | 0.01 | 27.65 | 28.72 |
| | 4 x | 2.72 | 2.66 | 6.20 | -0.10 | -0.17 | 0.04 | 22.06 | 22.59 |
| | 4 y | 2.70 | 2.72 | 6.20 | -0.13 | -0.11 | 0.03 | 22.25 | 22.10 |
| | 4 z | 1.28 | 1.36 | 5.01 | -0.21 | -0.18 | -0.03 | 46.86 | 44.28 |
| Diode P T60017 | 16 x | 8.72 | 8.55 | 21.62 | -0.30 | -0.48 | -0.13 | 6.88 | 7.02 |
| | 16 y | 9.08 | 9.04 | 21.81 | 0.05 | 0.01 | 0.06 | 6.61 | 6.64 |
| | 16 z | 2.16 | 2.72 | 17.44 | -0.14 | -0.11 | -0.03 | 27.78 | 22.07 |
| | 8 x | 3.89 | 3.83 | 11.05 | -0.06 | -0.12 | -0.01 | 15.44 | 15.67 |
| | 8 y | 3.88 | 3.89 | 11.06 | -0.07 | -0.06 | 0.01 | 15.46 | 15.44 |
| | 8 z | 2.17 | 2.09 | 9.80 | -0.19 | -0.12 | 0.01 | 27.65 | 28.72 |
| | 4 x | 2.72 | 2.66 | 6.20 | -0.10 | -0.17 | 0.04 | 22.06 | 22.59 |
| | 4 y | 2.70 | 2.72 | 6.20 | -0.13 | -0.11 | 0.03 | 22.25 | 22.10 |
| | 4 z | 1.28 | 1.36 | 5.01 | -0.21 | -0.18 | -0.03 | 46.86 | 44.28 |
| EFD 3G-pSi | 16 x | 8.81 | 8.83 | 21.63 | -0.21 | -0.19 | -0.12 | 6.81 | 6.79 |
| | 16 y | 8.96 | 8.82 | 21.67 | -0.06 | -0.20 | -0.08 | 6.70 | 6.80 |
| | 16 z | 2.29 | 2.82 | 17.44 | -0.00 | -0.00 | -0.04 | 26.18 | 21.24 |
| | 8 x | 3.98 | 3.98 | 11.06 | 0.03 | 0.04 | 0.00 | 15.07 | 15.06 |
| | 8 y | 4.00 | 3.96 | 11.03 | 0.05 | 0.01 | -0.03 | 14.99 | 15.15 |
| | 8 z | 2.31 | 2.25 | 9.76 | -0.05 | 0.03 | -0.03 | 26.01 | 26.71 |
| | 4 x | 2.86 | 2.84 | 6.24 | 0.04 | 0.01 | 0.08 | 20.96 | 21.15 |
| | 4 y | 2.85 | 2.86 | 6.23 | 0.02 | 0.04 | 0.07 | 21.09 | 20.98 |
| | 4 z | 1.39 | 1.49 | 4.99 | -0.10 | -0.05 | -0.05 | 43.18 | 40.35 |

Table 24. Results of Gamma Knife's Perfexion dose profile measurements obtained with Diode E T60016, Diode P T60017 and EFD 3G-pSi detectors for FWHM, LP (left penumbra) and RP (right Penumbra) values and their difference from Monte Carlo value as well as mean dose gradients in the penumbra regions. Values are rounded to one hundredth of a millimetre.

| Detector | Profile | LP / mm | RP / mm | FWHM / mm | LP diff. from MC / mm | RP diff from MC / mm | FWHM diff. from MC / mm | Mean dose gradient LP / % per mm | Mean dose gradient RP / % per mm |
|---|---|---|---|---|---|---|---|---|---|
| IBA CC04 | 16 x | 9.53 | 9.45 | 21.68 | 0.50 | 0.43 | -0.08 | 6.30 | 6.35 |
| | 16 y | 9.56 | 9.56 | 21.72 | 0.55 | 0.53 | -0.03 | 6.28 | 6.28 |
| | 16 z | 3.64 | 3.95 | 17.31 | 1.34 | 1.12 | -0.17 | 16.49 | 15.20 |
| | 8 x | 5.05 | 5.04 | 10.88 | 1.10 | 1.09 | -0.18 | 11.89 | 11.90 |
| | 8 y | 5.06 | 5.07 | 10.86 | 1.12 | 1.12 | -0.19 | 11.85 | 11.84 |
| | 8 z | 3.63 | 3.68 | 9.44 | 1.27 | 1.46 | -0.35 | 16.53 | 16.32 |
| | 4 x | 4.09 | 4.06 | 7.03 | 1.27 | 1.24 | 0.87 | 14.67 | 14.77 |
| | 4 y | 4.07 | 4.09 | 7.02 | 1.25 | 1.27 | 0.86 | 14.72 | 14.66 |
| | 4 z | 2.93 | 2.71 | 5.65 | 1.45 | 1.17 | 0.61 | 20.45 | 22.18 |
| RAZORnano chamber | 16 x | 8.70 | 8.78 | 21.42 | -0.32 | -0.24 | -0.33 | 6.90 | 6.83 |
| | 16 y | 9.23 | 9.19 | 21.68 | 0.20 | 0.17 | -0.07 | 6.50 | 6.53 |
| | 16 z | 3.04 | 2.66 | 17.38 | 0.75 | -0.16 | -0.10 | 19.73 | 22.55 |
| | 8 x | 4.23 | 4.29 | 10.94 | 0.28 | 0.34 | -0.12 | 14.19 | 13.99 |
| | 8 y | 4.28 | 4.43 | 10.95 | 0.33 | 0.48 | -0.10 | 14.01 | 13.56 |
| | 8 z | 2.58 | 2.79 | 9.72 | 0.23 | 0.58 | -0.08 | 23.23 | 21.52 |
| | 4 x | 3.27 | 3.24 | 6.13 | 0.45 | 0.42 | -0.03 | 18.34 | 18.50 |
| | 4 y | 3.16 | 3.18 | 6.16 | 0.33 | 0.36 | -0.01 | 19.01 | 18.86 |
| | 4 z | 1.97 | 1.80 | 4.93 | 0.48 | 0.26 | -0.11 | 30.44 | 33.37 |
| RAZOR chamber | 16 x | 9.13 | 9.20 | 21.50 | 0.10 | 0.17 | -0.25 | 6.57 | 6.52 |
| | 16 y | 9.24 | 9.24 | 21.53 | 0.22 | 0.22 | -0.22 | 6.49 | 6.49 |
| | 16 z | 3.30 | 3.69 | 17.51 | 1.01 | 0.87 | 0.04 | 18.16 | 16.25 |
| | 8 x | 4.44 | 4.44 | 10.83 | 0.49 | 0.49 | -0.23 | 13.53 | 13.51 |
| | 8 y | 4.45 | 4.47 | 10.81 | 0.50 | 0.52 | -0.25 | 13.50 | 13.43 |
| | 8 z | 3.26 | 3.28 | 9.72 | 0.90 | 1.06 | -0.08 | 18.42 | 18.30 |
| | 4 x | 3.44 | 3.45 | 6.08 | 0.62 | 0.63 | -0.08 | 17.44 | 17.38 |
| | 4 y | 3.43 | 3.47 | 6.09 | 0.61 | 0.65 | -0.08 | 17.47 | 17.29 |
| | 4 z | 2.50 | 2.57 | 5.41 | 1.01 | 1.04 | 0.37 | 24.00 | 23.32 |

Table 25. Results of Gamma Knife's Perfexion dose profile measurements obtained with CC04, RAZORnano and RAZOR chambers for FWHM, LP (left penumbra) and RP (right Penumbra) values and their difference from Monte Carlo values as well as mean dose gradients in the penumbra regions. Values are rounded to one hundredth of a millimetre.

| Detector | Profile | LP / mm | RP / mm | FWHM / mm | LP diff. from MC / mm | RP diff. from MC / mm | FWHM diff. from MC / mm | Mean dose gradient LP / % per mm | Mean dose gradient RP / % per mm |
|---|---|---|---|---|---|---|---|---|---|
| RAZOR diode | 16 x | 8.95 | 8.90 | 21.70 | -0.08 | -0.13 | -0.05 | 6.70 | 6.74 |
| | 16 y | 8.93 | 8.92 | 21.68 | -0.09 | -0.10 | -0.07 | 6.72 | 6.73 |
| | 16 z | 2.34 | 2.85 | 17.46 | 0.04 | 0.02 | -0.01 | 25.67 | 21.08 |
| | 8 x | 3.97 | 3.95 | 11.00 | 0.02 | 0.00 | -0.06 | 15.12 | 15.19 |
| | 8 y | 3.99 | 3.99 | 10.98 | 0.04 | 0.04 | -0.08 | 15.04 | 15.05 |
| | 8 z | 2.32 | 2.27 | 9.80 | -0.04 | 0.06 | 0.00 | 25.86 | 26.42 |
| | 4 x | 2.78 | 2.76 | 6.19 | -0.04 | -0.07 | 0.03 | 21.56 | 21.77 |
| | 4 y | 2.77 | 2.79 | 6.19 | -0.06 | -0.03 | 0.02 | 21.70 | 21.51 |
| | 4 z | 1.40 | 1.48 | 5.08 | -0.09 | -0.06 | 0.04 | 42.87 | 40.64 |
| microDIamond T60019 | 16 x | 8.78 | 8.73 | 21.64 | -0.25 | -0.30 | -0.11 | 6.84 | 6.87 |
| | 16 y | 9.17 | 9.16 | 21.85 | 0.15 | 0.14 | 0.10 | 6.54 | 6.55 |
| | 16 z | 2.23 | 2.72 | 17.38 | -0.07 | -0.10 | -0.10 | 26.92 | 22.02 |
| | 8 x | 4.09 | 4.02 | 11.11 | 0.14 | 0.07 | 0.05 | 14.69 | 14.93 |
| | 8 y | 4.03 | 4.07 | 11.09 | 0.08 | 0.12 | 0.04 | 14.88 | 14.74 |
| | 8 z | 2.28 | 2.18 | 9.70 | -0.07 | -0.03 | -0.10 | 26.27 | 27.52 |
| | 4 x | 2.93 | 2.88 | 6.25 | 0.11 | 0.05 | 0.09 | 20.45 | 20.87 |
| | 4 y | 2.90 | 2.96 | 6.27 | 0.07 | 0.12 | 0.11 | 20.70 | 20.36 |
| | 4 z | 1.39 | 1.46 | 4.92 | -0.10 | -0.07 | -0.12 | 43.02 | 40.92 |
| EBT3 film | 16 x | 8.39 | 8.52 | 21.24 | -0.63 | -0.51 | -0.51 | 7.15 | 7.05 |
| | 16 y | 8.75 | 8.70 | 21.73 | -0.28 | -0.33 | -0.02 | 6.86 | 6.90 |
| | 16 z | 2.35 | 2.90 | 17.52 | 0.05 | 0.08 | 0.05 | 25.54 | 20.68 |
| | 8 x | 3.94 | 3.96 | 10.86 | -0.01 | 0.01 | -0.20 | 15.25 | 15.16 |
| | 8 y | 4.12 | 4.02 | 11.02 | 0.17 | 0.07 | -0.02 | 14.58 | 14.93 |
| | 8 z | 2.53 | 2.42 | 9.07 | 0.17 | 0.21 | -0.73 | 23.72 | 24.79 |
| | 4 x | 2.86 | 2.79 | 5.95 | 0.04 | -0.04 | -0.21 | 20.95 | 21.55 |
| | 4 y | 2.77 | 2.79 | 6.18 | -0.06 | -0.02 | 0.02 | 21.70 | 21.48 |
| | 4 z | 1.62 | 1.61 | 5.04 | 0.13 | 0.08 | 0.00 | 36.96 | 37.20 |

Table 26. Results of Gamma Knife's Perfexion dose profile measurements obtained with RAZOR diode, microDiamond and EBT3 film for FWHM, LP (left penumbra) and RP (right Penumbra) values and their difference from Monte Carlo values as well as mean dose gradients in the penumbra regions. Values are rounded to one hundredth of a millimetre.
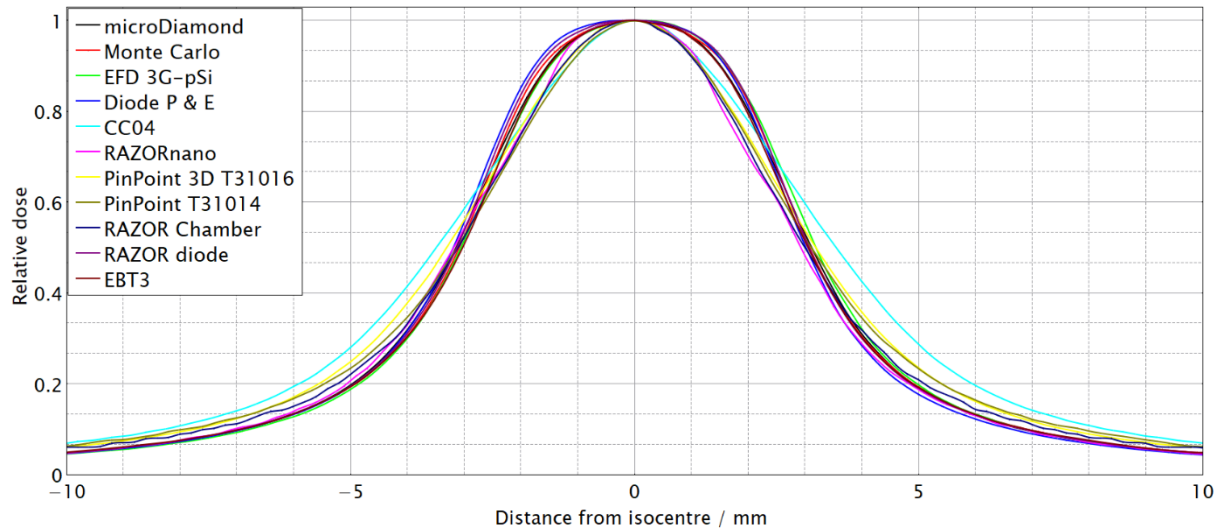
Figure 40. 4 mm x - axis dose profile determined with Monte Carlo, microDiamond, EFD 3G-pSi, Diode P & E, CC04 chamber, RAZORnano, PinPoint, PinPoint 3D, RAZOR chamber, RAZOR diode and EBT3 film.
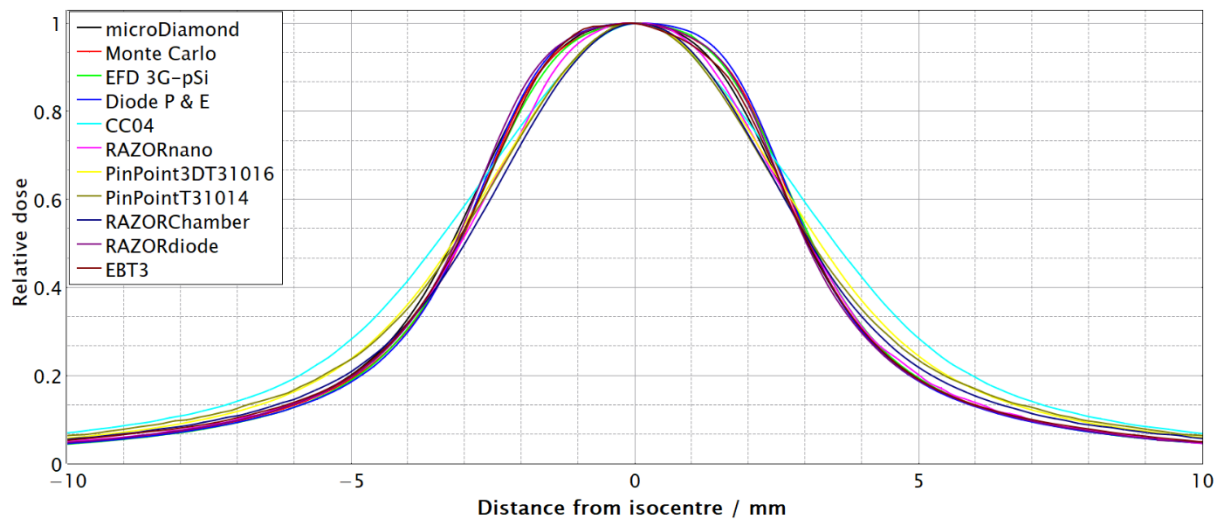


Figure 41. 4 mm y - axis dose profile determined with Monte Carlo, microDiamond, EFD 3G-pSi, Diode P & E, CC04 chamber, RAZORnano, PinPoint, PinPoint 3D, RAZOR chamber, RAZOR diode and EBT3 film.
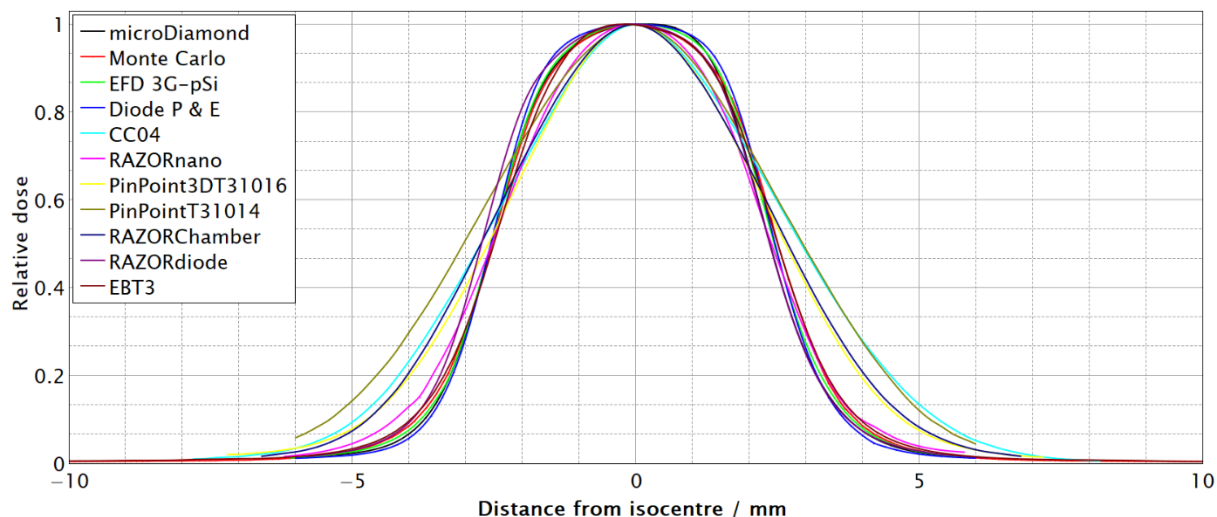
Figure 42. 4 mm z - axis dose profile determined with Monte Carlo, microDiamond, EFD 3G-pSi, Diode P & E, CC04 chamber, RAZORnano, PinPoint, PinPoint 3D, RAZOR chamber, RAZOR diode and EBT3 film.
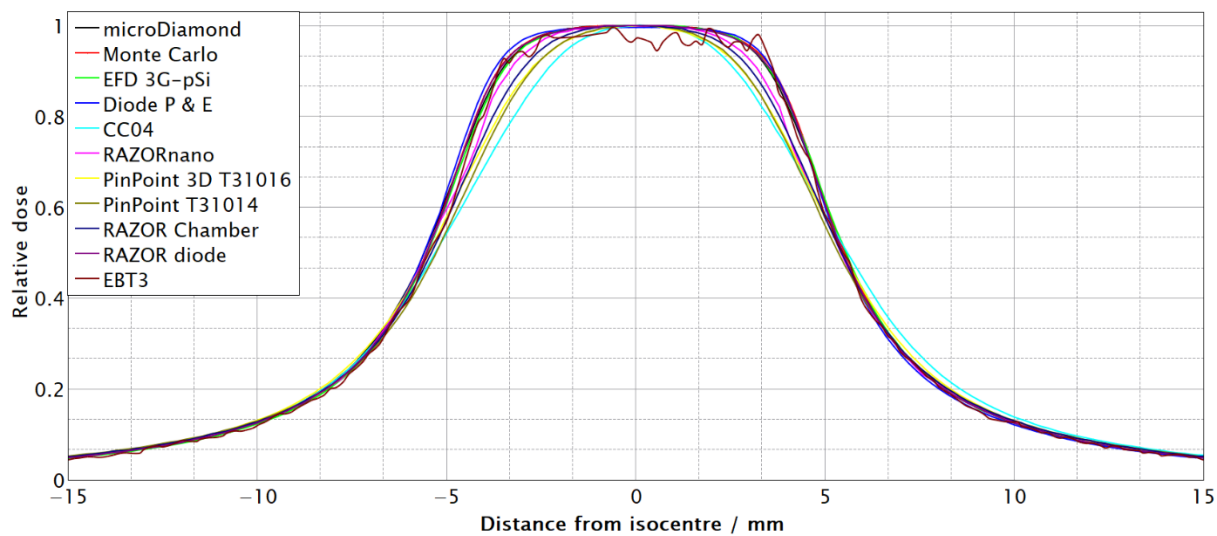


Figure 43. 8 mm x - axis dose profile determined with Monte Carlo, microDiamond, EFD 3G-pSi, Diode P & E, CC04 chamber, RAZORnano, PinPoint, PinPoint 3D, RAZOR chamber, RAZOR diode and EBT3 film.
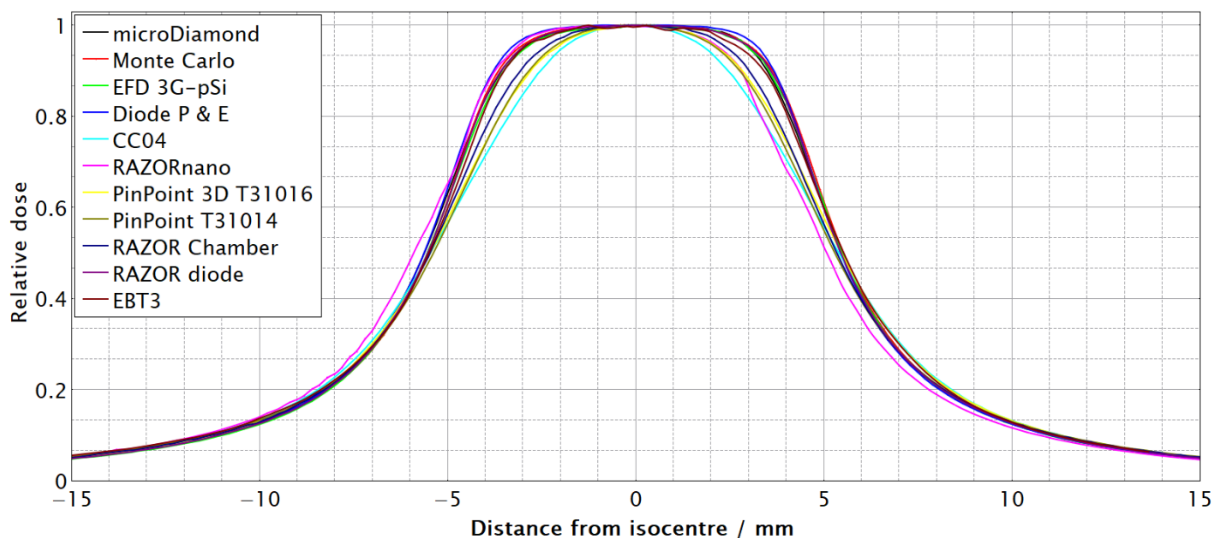
Figure 44. 8 mm y - axis dose profile determined with Monte Carlo, microDiamond, EFD 3G-pSi, Diode P & E, CC04 chamber, RAZORnano, PinPoint, PinPoint 3D, RAZOR chamber, RAZOR diode and EBT3 film.
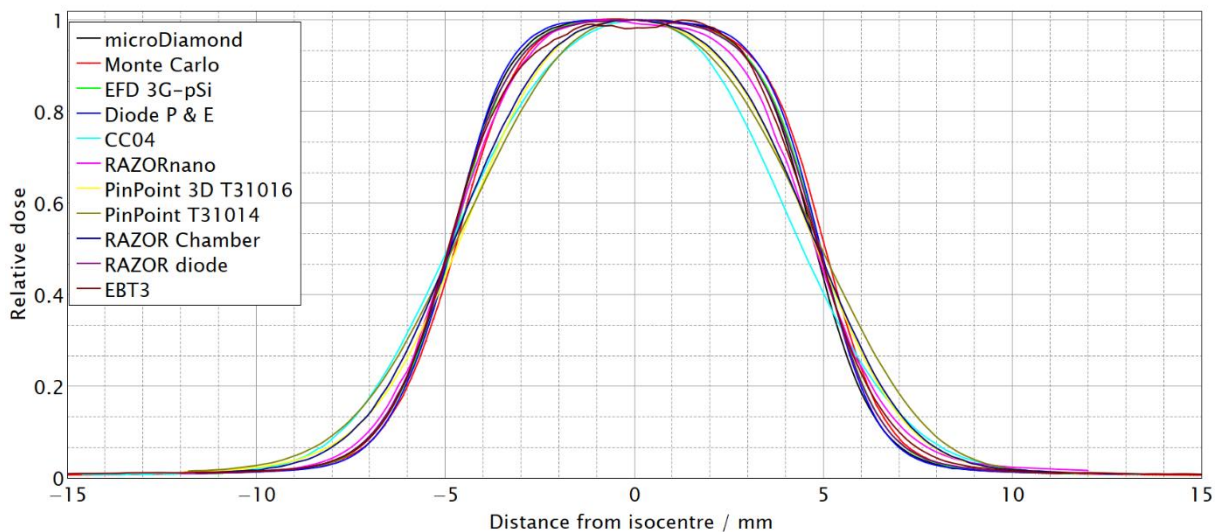


Figure 45. 8 mm z - axis dose profile determined with Monte Carlo, microDiamond, EFD 3G-pSi, Diode P & E, CC04 chamber, RAZORnano, PinPoint, PinPoint 3D, RAZOR chamber, RAZOR diode and EBT3 film.
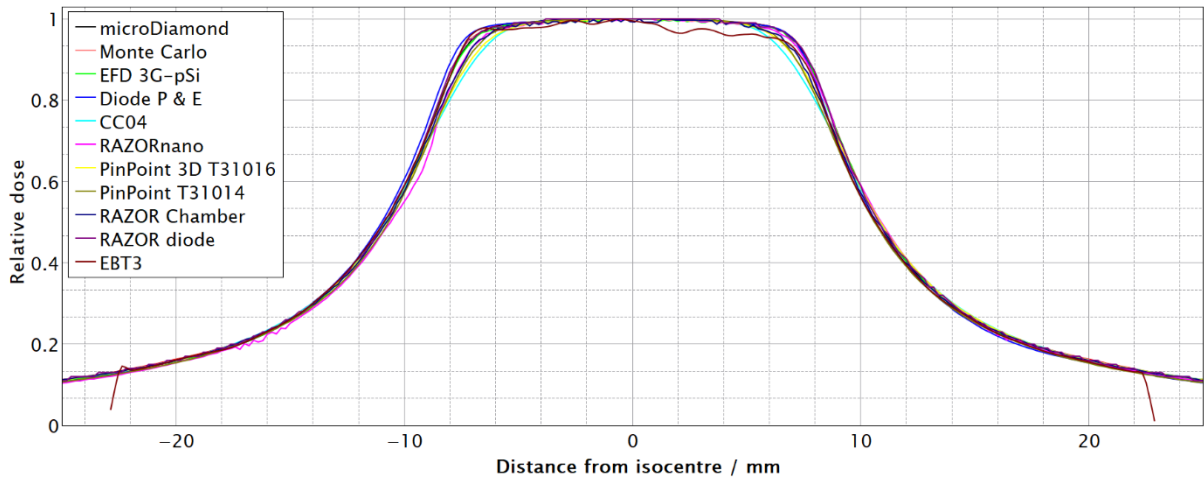
Figure 46. 16 mm x - axis dose profile determined with Monte Carlo, microDiamond, EFD 3G-Si, Diode P & E, CC04 chamber, RAZORnano, PinPoint, PinPoint 3D, RAZOR chamber, RAZOR diode and EBT3 film.
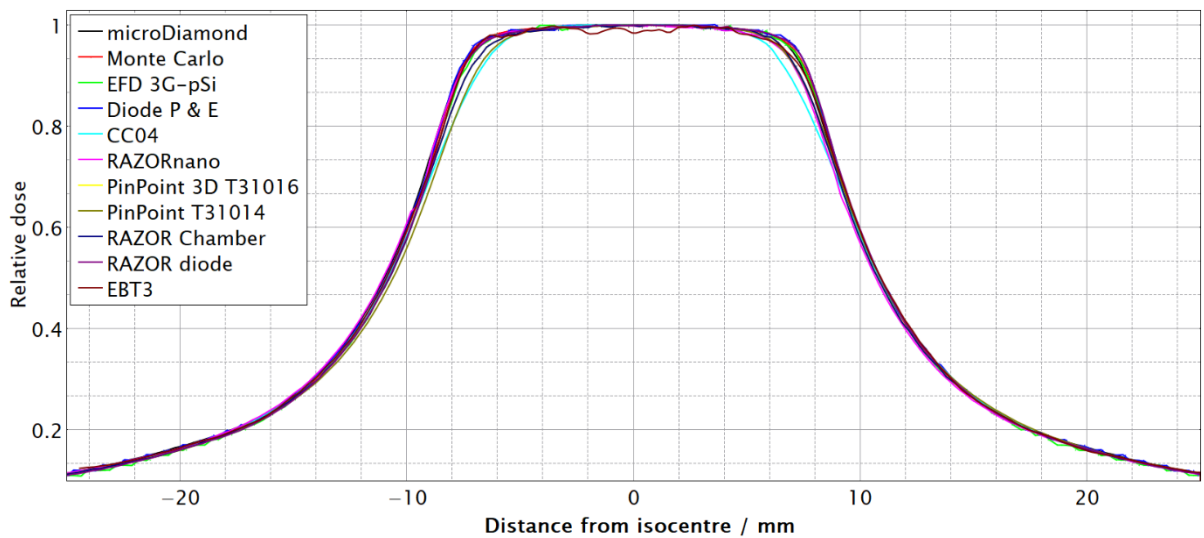


Figure 47. 16 mm y - axis dose profile determined with Monte Carlo, microDiamond, EFD 3G-pSi, Diode P & E, CC04 chamber, RAZORnano, PinPoint, PinPoint 3D, RAZOR chamber, RAZOR diode and EBT3 film.
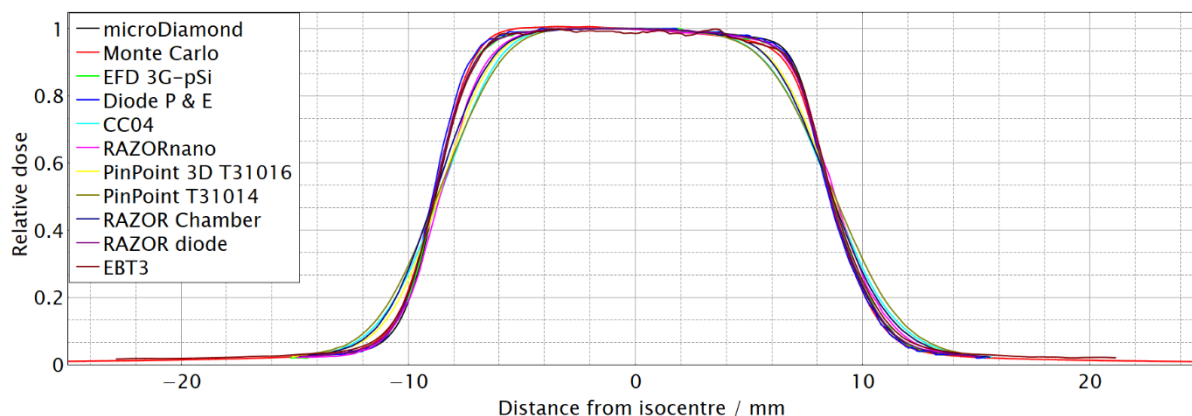
Figure 48. 16 mm z - axis dose profile determined with Monte Carlo, microDiamond, EFD 3G-pSi, Diode P & E, CC04 chamber, RAZORnano, PinPoint, PinPoint 3D, RAZOR chamber, RAZOR diode and EBT3 film.

In Figure 49. and Figure 50. the difference from the Monte Carlo values in the width of the left and right penumbra for all dose profiles is presented. All ionization chambers have a larger difference from Monte Carlo values than semiconductor or diamond detectors due to the more dominant volume-averaging effect (Table 16.). RAZORnano chamber, ionization chamber with the smallest volume (V=3 mm$^3$), is in between these two groups of detectors, therefore, one can expect its volume-averaging correction factor to be the smallest of all ionization chambers. A spike in the difference of ionization chambers at the z-axis dose profile for all field sizes is noticeable while the difference for the x and y -axis is not as pronounced. This can be explained by the difference in the length of these profiles, increasing the volume-averaging i.e. z-axis dose profile is shorter than the x and y-axis. One should keep in mind that detectors were placed parallel with the z-axis of the device because of the phantom default geometry making them more influenced by the z-axis dose gradient. This effect is noticeable for RAZORnano chamber as well, being spherical in shape. Although the PinPoint T31014 chamber is not the largest (V=15 mm$^3$), its difference in the width of the penumbras from the Monte Carlo values is the largest for the z-axis dose profile. This can be explained by the volume-averaging correction factors previously calculated (Table 16.). Because of the shape of the PinPoint T31014 chamber and its position with the long axis parallel to the z-axis dose profile while scanning the profile, it is more influenced by the gradient of the z–axis dose profile, increasing volume-averaging and flattening the dose profile. Both CC04 and PinPoint 3D T31016 chambers have larger volumes than PinPoint, however, they are more compact

reducing therefore their volume-averaging (the length-to-diameter ratio is closer to one). The differences from the Monte Carlo results on the x and y – axis dose profile are largest for the CC04 because of its volume (V=40 mm$^3$), followed by the PinPoint 3D (V=16 mm$^3$), PinPoint (V=15mm$^3$), RAZOR chamber (V=10 mm$^3$) and RAZORnano chamber (V=3 mm$^3$) (Figure 49. and Figure 50.). This supports previous findings that the z-axis dose profile plays a fundamental role in volume-averaging on Gamma Knife and that besides volume, the shape of the detector has an important role as well as explained in section 5.4. From this study, we conclude that the semiconductor and diamond detector, alongside EBT3 film are a better option for dose profile determination than ionization chambers.
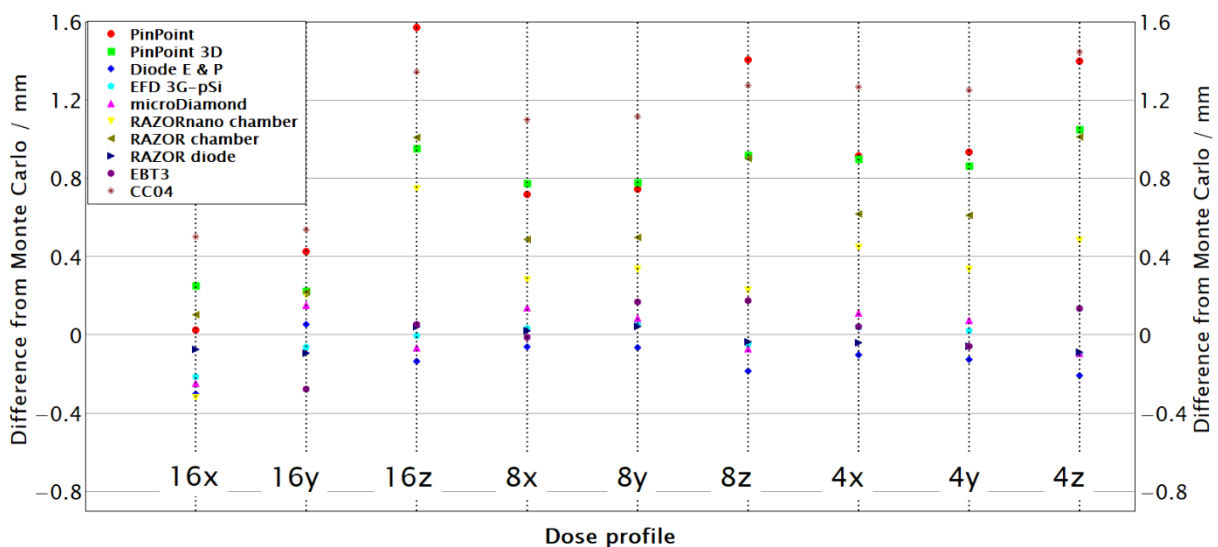


Figure 49. The difference from Monte Carlo results in the widths of left penumbra (LP) measured with different detectors.

The semiconductor detector, microDiamond and EBT3 films have much smaller differences in the width of left and right penumbras from Monte Carlo values compared with the ionization chambers (Figure 49. and Figure 50.). This is, again, due to its volume which is several orders of magnitude smaller than the ionization chamber's one, therefore, minimizing the volume-averaging effect. The spike at the z-axis dose profile is smaller since the spatial dimensions of the detector in that direction are small limiting the influence of the z-axis dose gradient. Due to the small thickness of these detectors many of them show a decrease in the difference from Monte Carlo values when scanning z -the axis dose profile and an increase in the x and y direction. However, these differences are not as pronounced as they are for ionization

118

chambers and when performing dose profile measurements, they should be the detectors of choice.
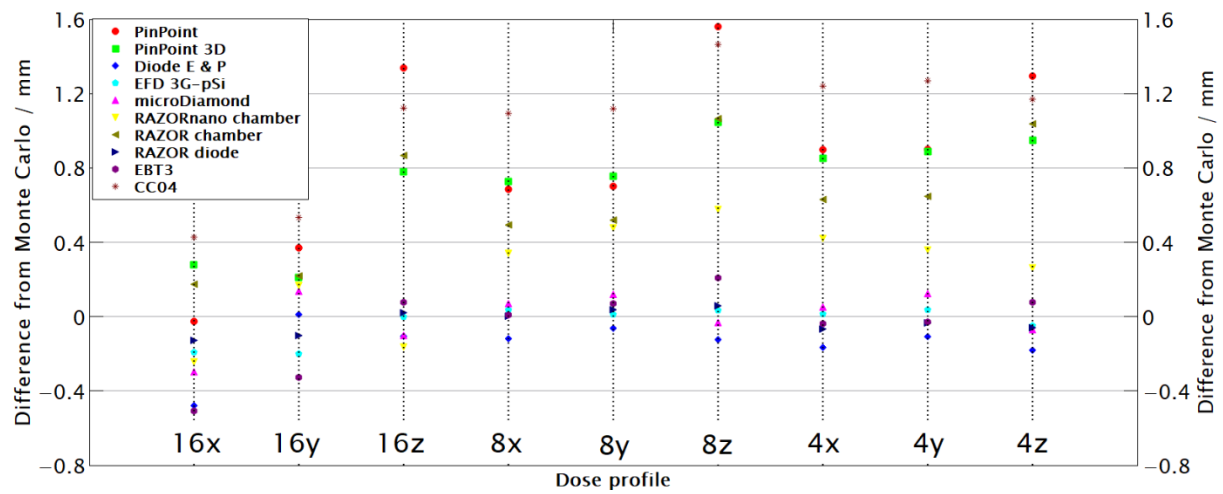


Figure 50. Difference from Monte Carlo in the widths of right penumbra (RP) measured with different detectors.

The results of an analysis for FWHM value can be seen in Figure 51. The difference from Monte Carlo values is smaller than it is for the width of penumbra regions. This is expected since volume-averaging should not impact the FHWM values. It can be seen from Figure 40. to Figure 48., that the measured dose profile passes through or nearby the point of 50% isodose value resulting in a minimal difference in FWHM value. The exceptions are CC04 and PinPoint chambers which show a substantial increase at 4 mm field size.
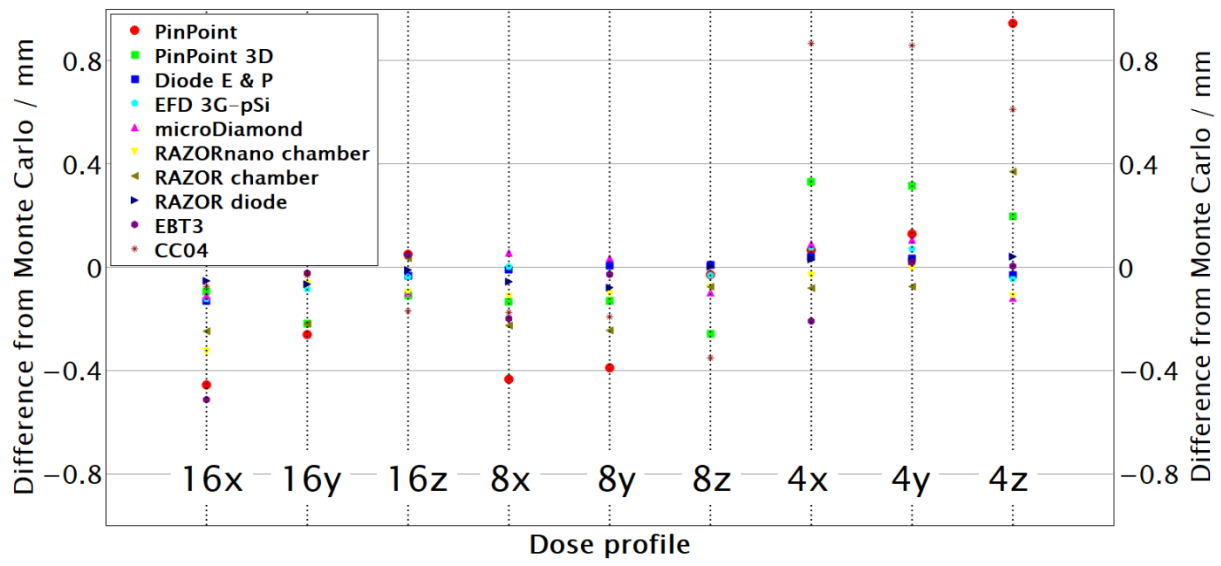
Figure 51. The difference from Monte Carlo results in the FWHM value measured with different detectors.

# 6. Conclusion

A first hypothesis of this dissertation is directed towards the problem of finding the suitable detector for dosimetry of Gamma Knife's narrow photon beams. Therefore, field output factors $\Omega_{Q_0,Q_0}^{f_{clin},f_{msr}}$ were determined with: seven ionization chambers, four semiconductor detectors, and diamond detectors. Detector's data were compared against Monte Carlo and EBT3 film values. Additionally, a detectors-specific correction factors $k_{Q_0,Q_0}^{f_{clin},f_{msr}}$ were determined for investigated detectors, all widely used for relative dosimetry.

EBT3 film overestimated the field output factor for the smallest 4 mm field by 1.4% and underestimated the 8 mm field by 1.2%. As shown in this research EBT3 film does have disadvantages such as the low signal-to-noise ratio, demanding handling and postirradiation processing. Most importantly, the uncertainty of the absorbed dose determined with the EBT3 film detector can be substantial. Ionization chambers have consistently underestimated field output factors due to perturbation which are more emphasized in smaller fields. Large ionization chambers such as Semiflex T31010, Semiflex 3D T31021, PinPoint T31014, PinPoint 3D T31016, RAZOR chamber and CC04, are not suitable for dosimetry in the smallest 4 mm field. The exception is RAZORnano chamber. Semiconductor and diamond detector have performed better than ionization chambers in the 4 mm field size and have substantially lower detector-specific correction factors. This is primarily due to smaller volume-averaging effect. It has been shown that not a single investigated detector can fulfil the CPE condition in the 4 mm field (Table 15.).

All ionization chambers have shown better agreement of their field output factors with the reference values in the 8 mm field. This is due to the preservation of lateral charged particle equilibrium (Table 15.) and decrease of volume-averaging effect (Table 16.). Large ionization chambers (e.g., Semiflex and Semiflex 3D) have significant perturbations, thus, they are not recommended for the dosimetry of 8 mm field. CC04 has underestimated the doze by 3.2%. Remaining ionization chambers have their detector-specific correction factors within 1% from reference values. Semiconductor detectors have shown better agreement with field output factors determined with the Monte Carlo calculations and EBT3 film than ionization chambers in the 4 mm field due to their small volume and high sensitivity. On the other hand, all of them

over-responded because of the high atomic numbers of silicon. The microDiamond detector has proven to be the best active detector with values of field output factors within 1.6% for all field sizes. Uncertainty analysis has shown that EBT3 film, although tissue-equivalent, has large uncertainty (Table 11.). Active detectors are more stable with lower uncertainties, but they require correction factors (Table 12.).

Given the fact that there is a small number of detectors with the detectors-specific correction factors for narrow Co-60 beams reported in the IAEA TRS-483 CoP, this research can be considered as a valuable supplement to the results of previous investigations[12,15–18,20,24,31,39,90,91] already published and complied as IAEA TRS-483 CoP dataset. [10]

Our second hypothesis is aimed towards the problem of accurate determination of volume-averaging correction factor in the narrow Co-60 beams of Gamma Knife. It is assumed that volume-averaging correction factors $(k_{vol})_{Q_0,Q_0}^{f_{msr},f_{clin}}$ can be calculated by simulating the ellipsoid absorbed dose model and the detector geometries inside it. Applying numerical integration of the absorbed dose distribution over the detector's volume, a volume-averaging correction factor is calculated in all fields for: seven ionization chambers, four semiconductor detectors and a diamond detector.[54] To the best of our knowledge, no volume averaging correction factors for clinically used detectors in different Gamma Knife absorbed dose distributions have been previously reported in the literature.

It is confirmed that the volume-averaging correction factor is inversely proportional to the field size, and in general, it increases with the detector's size. It can be noticed that some detectors have more prominent correction, although smaller in volume. The reason for this is the z-axis dose profile which is asymmetrical and shorter compared with the x and y-axis. Placing the detectors with the long axis in the z-direction makes them more influenced by the asymmetry of the shortest z-axis dose profile. Consequently, the larger change of a dose gradient over their effective volume will result in increased volume-averaging. Because of this, an ionization chamber such as PinPoint T31014 has higher correction than CC04 for the smallest 4 mm field although is almost three times smaller in volume. It can be concluded that although the size of an effective volume of the detector is important the shape of the detectors plays an important role as well. These findings are supported by previous studies

involving dosimetry of high-energy X-rays with detectors positioned in parallel and perpendicular orientations.[55]

Additionally, it has been shown that volume-averaging is the dominant perturbation in the narrow Co-60 beams used by Gamma Knife for the detectors that have their detector-specific correction factor reported in the IAEA TRS-483 CoP (Table 17.). Presented volume-averaging data can be considered as valuable supplement to the literature.

Finally, third hypothesis aimed at the problem of dose profile determination on Gamma Knife and finding the suitable detectors for such measurements. In this research, Gamma Knife's dose profiles are determined with EBT3 film and ten active detectors; five ionization chambers, four semiconductor and diamond detector. Obtained results are compared with Monte Carlo calculated values. Some detectors were excluded from this study due to their large volume while others were unavailable (Table 16). The difference in the widths of penumbras and FWHM values for different detectors was examined. Since volume-averaging is the only effect influencing the dose profile, ionization chambers with large volumes are not suitable for these types of measurements. They significantly underestimate the absorbed dose in the region of 100%-50% of relative value, and overestimate for the remaining dose profile. Results of smaller ionization chamber, e.g. RAZORnano, agree better with Monte Carlo calculated profiles. Moreover, it is noticed that large ionization chambers have a spike in difference for the z-axis dose profile. Reasons for this can be found in the shorter length (FWHM) of the z-axis dose profile and detector's position. Semiconductor detectors, and diamond detectors due to their small size have results in better agreement with the Monte Carlo calculated profiles. They, together with the EBT3 film should be the detectors of choice for dose profile determination.

# References

1. Andreo P. The physics of small megavoltage photon beam dosimetry. *Radiotherapy and Oncology*. 2018;126(2):205-213. doi:10.1016/j.radonc.2017.11.001

2. ICRU. ICRU REPORT 91: Prescribing, Recording, and Reporting of Stereotactic Treatments with Small Photon Beams. *J ICRU*. 2014;14(2):1-1. doi:10.1093/JICRU_NDX009

3. Elekta. Gamma Knife Surgery | Radiosurgery Treatment Process | Elekta. Accessed February 23, 2023. https://www.elekta.com/patients/gamma-knife-treatment/

4. The National Centre for Stereotactic Radiosurgery. What is a Gamma Knife. Accessed July 20, 2023. https://www.gammaknife.org.uk/sheffield-centre/what-is-gamma-knife

5. The World Health Organization. Cancer. Accessed February 23, 2023. https://www.who.int/health-topics/cancer#tab=tab_1

6. Siegel RL, Miller KD, Fuchs HE, Jemal A. Cancer statistics, 2022. *CA Cancer J Clin*. 2022;72(1):7-33. doi:10.3322/CAAC.21708

7. National Cancer Institute. Cancer Statistics - NCI. Accessed February 23, 2023. https://www.cancer.gov/about-cancer/understanding/statistics

8. Das IJ, Morales J, Francescon P. Small field dosimetry: What have we learnt? *AIP Conf Proc*. 2016;1747(June 2016). doi:10.1063/1.4954111

9. Das IJ, Ding GX, Ahnesjö A. Small fields: nonequilibrium radiation dosimetry. *Med Phys*. 2008;35(1):206-215. doi:10.1118/1.2815356

10. International Atomic Energy Agency. *Dosimetry of Small Static Fields Used in External Beam Radiotherapy, Technical Reports Series No. 483*.; 2017. http://www-ns.iaea.org/standards/

11. Alfonso R, Andreo P, Capote R, et al. A new formalism for reference dosimetry of small and nonstandard fields. *Med Phys*. 2008;35(11):5179-5186. doi:10.1118/1.3005481

12. Mack A, Scheib SG, Major J, et al. Precision dosimetry for narrow photon beams used in radiosurgery - Determination of Gamma Knife® output factors. *Med Phys*. 2002;29(9):2080-2089. doi:10.1118/1.1501138

13. Das I, Downes MB, Kassaee A. Choice of Radiation Detector in Dosimetry of Stereotactic Radiosurgery-Radiotherapy. *Journal of Radiosurgery*. 2000;3(4):177-186. doi:10.1023/A:1009594509115

14. Azangwe G, Grochowska P, Georg D, et al. Detector to detector corrections: A comprehensive experimental study of detector specific correction factors for beam output measurements for small radiotherapy beams. *Med Phys*. 2014;41(7). doi:10.1118/1.4883795

15. Zoros E, Pappas EP, Moutsatsos A, et al. Monte carlo determination of correction factors for dosimetric measurements in gamma knife perfexion small fields. *Physica Medica*. 2016;32:237. doi:10.1016/j.ejmp.2016.07.494

16. Barrett JC, Knill C. Monte Carlo calculated correction factors for the PTW microDiamond detector in the Gamma Knife-Model C. *Med Phys*. 2016;43(3):1035-1044. doi:10.1118/1.4940790

17.	Medjadj T, Ksenofontov AI, Klimanov VA, Dalechina A V., Kirpichev YS. Experimental Validation of Monte Carlo Simulation for the Leksell Gamma Knife Perfexion Using Gafchromic EBT3 Dosimetry Film and Diamond Detector T60019 PTW. *Instruments and Experimental Techniques*. 2021;64(1):146-152. doi:10.1134/S0020441221010292

18.	Mirzakhanian L, Benmakhlouf H, Tessier F, Seuntjens J. Determination of kQmsr,Q0fmsr,fref factors for ion chambers used in the calibration of Leksell Gamma Knife Perfexion model using EGSnrc and PENELOPE Monte Carlo codes. *Med Phys*. 2018;45(4):1748-1757. doi:10.1002/mp.12821

19.	Donya H, Seniwal B, Darwesh R, Fonseca TCF. Prospective Monte Carlo Simulation for Choosing High Efficient Detectors for Small-Field Dosimetry. In: *Theory, Application, and Implementation of Monte Carlo Method in Science and Technology (Working Title)*. IntechOpen; 2019. doi:10.5772/intechopen.89150

20.	Benmakhlouf H, Johansson J, Paddick I, Andreo P. Monte Carlo calculated and experimentally determined output correction factors for small field detectors in Leksell Gamma Knife Perfexion beams. *Phys Med Biol*. 2015;60(10):3959-3973. doi:10.1088/0031-9155/60/10/3959

21.	Andreo P. Monte Carlo simulations in radiotherapy dosimetry. *Radiation Oncology*. 2018;13(1):1-15. doi:10.1186/S13014-018-1065-3/FIGURES/8

22.	Klawikowski SJ, Yang JN, Adamovics J, Ibbott GS. PRESAGE 3D dosimetry accurately measures Gamma Knife outputfactors. *Phys Med Biol*. 2014;59(23):N211-N220. doi:10.1088/0031-9155/59/23/N211

23.	Casar B, Gershkevitsh E, Mendez I, Jurković S, Huq MS. A novel method for the determination of field output factors and output correction factors for small static fields for six diodes and a microdiamond detector in megavoltage photon beams. *Med Phys*. 2019;46(2):944-963. doi:10.1002/mp.13318

24.	Ekstrand KE, Bourland JD. *A Film Technique for the Determination of Output Factors and End Effect Times for the Leksell Gamma Knife INSTITUTE OF PHYSICS PUBLISHING PHYSICS IN MEDICINE A Film Technique for the Determination of Output Factors and End Effect Times for the Leksell Gamma Knife*. Vol 46.; 2001. http://iopscience.iop.org/0031-9155/46/3/306

25.	Massillon-JL G, Cueva-Prócel D, Díaz-Aguirre P, Rodríguez-Ponce M, Herrera-Martínez F. Dosimetry for Small Fields in Stereotactic Radiosurgery Using Gafchromic MD-V2-55 Film, TLD-100 and Alanine Dosimeters. *PLoS One*. 2013;8(5). doi:10.1371/journal.pone.0063418

26.	Calcina CSG, De Oliveira LN, De Almeida CE, De Almeida A. Dosimetric parameters for small field sizes using Fricke xylenol gel, thermoluminescent and film dosimeters, and an ionization chamber. *Phys Med Biol*. 2007;52(5):1431-1439. doi:10.1088/0031-9155/52/5/014

27.	A Chalkley, G Heyes. Evaluation of a synthetic single-crystal diamond detector for relative dosimetry measurements on a CyberKnife. *Br J Radiol*. 2014;87(1035):20130768. doi:10.1259/BJR.20130768

28.	Papaconstadopoulos P, Archambault L, Seuntjens J. Experimental investigation on the accuracy of plastic scintillators and of the spectrum discrimination method in small photon fields. *Med Phys*. 2017;44(2):654-664. doi:10.1002/MP.12064

29.    Parwaie W, Refahi S, Ardekani MA, Farhood B. Different Dosimeters/Detectors Used in Small-Field Dosimetry: Pros and Cons. *J Med Signals Sens*. 2018;8(3):195. doi:10.4103/JMSS.JMSS_3_18

30.    Ralston A, Liu P, Warrener K, McKenzie D, Suchowerska N. Small field diode correction factors derived using an air core fibre optic scintillation dosimeter and EBT2 film. *Phys Med Biol*. 2012;57(9):2587-2602. doi:10.1088/0031-9155/57/9/2587

31.    Veselsky T, Novotny J, Pastykova V. Assessment of basic physical and dosimetric parameters of synthetic single-crystal diamond detector and its use in Leksell Gamma Knife and CyberKnife small radiosurgical fields. *International Journal of Radiation Research*. 2018;16(1):7-16. doi:10.18869/acadpub.ijrr.16.1.7

32.    Sibatal CH, Mota HC, Beddar § A S, Higginsjl PD, Shin KH. *Influence of Detector Size in Photon Beam Profile Measurements Influence of Detector Size in Photon Beam Profile Measurements"*. Vol 36.; 1991. http://iopscience.iop.org/0031-9155/36/5/005

33.    Hršak H, Majer M, Grego T, Bibić J, Heinrich Z. Correction of measured Gamma-Knife output factors for angular dependence of diode detectors and PinPoint ionization chamber. *Physica Medica*. 2014;30(8):914-919. doi:10.1016/j.ejmp.2014.09.002

34.    Papaconstadopoulos P. *On the Detector Response and the Reconstruction of the Source Intensity Distribution in Small Photon Fields*. Doctoral Thesis. McGill University; 2016. Accessed February 15, 2023. https://escholarship.mcgill.ca/concern/theses/df65vb396

35.    Junios J, Irhas I, Novitrian N, et al. Characterization of Gamma Knife Perfexion™ source based on Monte Carlo simulation. *Radiol Phys Technol*. 2020;13(4):398-404. doi:10.1007/S12194-020-00590-3

36.    Benmakhlouf H, Johansson J, Paddick I, Andreo P. Monte Carlo calculated and experimentally determined output correction factors for small field detectors in Leksell Gamma Knife Perfexion beams. *Phys Med Biol*. 2015;60(10):3959-3973. doi:10.1088/0031-9155/60/10/3959

37.    Papaconstadopoulos P, Tessier F, Seuntjens J. On the correction, perturbation and modification of small field detectors in relative dosimetry. *Phys Med Biol*. 2014;59(19):5937-5952. doi:10.1088/0031-9155/59/19/5937

38.    Das IJ, Ding GX, Ahnesjö A. Small fields: Nonequilibrium radiation dosimetry. *Med Phys*. 2008;35(1):206-215. doi:10.1118/1.2815356

39.    Somigliana A, Cattaneo GM, Fiorino C, et al. Dosimetry of Gamma Knife and linac-based radiosurgery using radiochromic and diode detectors. *Phys Med Biol*. 1999;44(4):887-897. doi:10.1088/0031-9155/44/4/006

40.    Sibatal CH, Mota HC, Beddar § A S, Higginsjl PD, Shin KH. *Influence of Detector Size in Photon Beam Profile Measurements Influence of Detector Size in Photon Beam Profile Measurements"*. Vol 36.; 1991. http://iopscience.iop.org/0031-9155/36/5/005

41.    Sauer OA, Wilbert J. Measurement of output factors for small photon beams. *Med Phys*. 2007;34(6):1983-1988. doi:10.1118/1.2734383

42.    GAFCHROMIC ™ DOSIMETRY MEDIA. *EBT3 Specification and User Guide*. Accessed March 8, 2023. http://www.gafchromic.com/gafchromic-film/radiotherapy-films/EBT/index.asp

43.     Sharma M, Singh R, Dutt S, Tomar P, Trivedi G, Robert N. Effect of absorbed dose on post-irradiation coloration and interpretation of polymerization reaction in the Gafchromic EBT3 film. *Radiation Physics and Chemistry*. 2021;187. doi:10.1016/j.radphyschem.2021.109569

44.     Mancosu P, Reggiori G, Stravato A, et al. Evaluation of a synthetic single-crystal diamond detector for relative dosimetry on the Leksell Gamma Knife Perfexion radiosurgery system. *Med Phys*. 2015;42(9):5035-5041. doi:10.1118/1.4927569

45.     Kim TH, Yang HJ, Jeong JY, Schaarschmidt T, Kim YK, Chung HT. Feasibility of isodose-shaped scintillation detectors for the measurement of gamma knife output factors. *Med Phys*. 2022;49(3):1944-1954. doi:10.1002/mp.15469

46.     Massillon-JL G, Cueva-Prócel D, Díaz-Aguirre P, Rodríguez-Ponce M, Herrera-Martínez F. Dosimetry for small fields in stereotactic radiosurgery using gafchromic MD-V2-55 film, TLD-100 and alanine dosimeters. *PLoS One*. 2013;8(5). doi:10.1371/JOURNAL.PONE.0063418

47.     Kim TH, Yang HJ, Jeong JY, Schaarschmidt T, Kim YK, Chung HT. Feasibility of isodose-shaped scintillation detectors for the measurement of gamma knife output factors. *Med Phys*. 2022;49(3):1944-1954. doi:10.1002/mp.15469

48.     International Atomic Energy Agency. Absorbed Dose Determination in External Beam Radiotherapy An International Code of Practice for Dosimetry Based on Standards of Absorbed Dose to Water.

49.     Aspradakis MM, Byrne JP, Palmans H, et al. *IPEM Report 103 Small Field MV Photon Dosimetry*.; 2010. Accessed February 20, 2023. https://www.ipem.ac.uk/resources/books/report-103-small-field-mv-photon-dosimetry/

50.     Andreo P. The physics of small megavoltage photon beam dosimetry. *Radiotherapy and Oncology*. 2018;126(2):205-213. doi:10.1016/j.radonc.2017.11.001

51.     Wuerfel JU. Dose measurements in small fields. *Medical Physics International Journal*. 2013;1(1):81-90. Accessed February 13, 2023. http://www.mpijournal.org/pdf/2013-01/MPI-2013-01-p081.pdf

52.     Papaconstadopoulos P, Tessier F, Seuntjens J. On the correction, perturbation and modification of small field detectors in relative dosimetry. *Phys Med Biol*. 2014;59(19):5937-5952. doi:10.1088/0031-9155/59/19/5937

53.     Kawachi T, Saitoh H, Inoue M, Katayose T, Myojoyama A, Hatano K. Reference dosimetry condition and beam quality correction factor for CyberKnife beam. *Med Phys*. 2008;35(10):4591-4598. doi:10.1118/1.2978228

54.     Šegedin N, Hršak H, Babić SD, Jurković S. Determination of volume averaging correction factors using an elliptical absorbed dose model for Gamma Knife Perfexion. *J Appl Clin Med Phys*. Published online 2023:e14109. doi:10.1002/ACM2.14109

55.     Casar B, Gershkevitsh E, Mendez I, Jurković S, Saiful Huq M. Output correction factors for small static fields in megavoltage photon beams for seven ionization chambers in two orientations — perpendicular and parallel. *Med Phys*. 2020;47(1):242-259. doi:10.1002/mp.13894

56.     De Almeida CE, Salata C. *Absolute, Reference, and Relative Dosimetry in Radiotherapy*. Vol 1.; 2021. doi:10.5772/intechopen.98044

57.    Lindquist C, Paddick I. The Leksell Gamma knife Perfexion and comparision with its predecessors. *OPERATIVE NEUROSURGERY*. 2007;61. doi:10.1227/01.NEU.0000279989.86544.B6

58.    Xu AY, Bhatnagar JP, Bednarz G, et al. SU-E-T-578: Dose Differences Between the Three Dose Calculation Algorithms in Leksell GammaPlan. *Med Phys*. 2013;40(6):338. doi:10.1118/1.4815006

59.    Lindquist C, Paddick I. The Leksell Gamma Knife Perfexion and comparisons with its predecessors. *Neurosurgery*. 2007;61(3 Suppl). doi:10.1227/01.NEU.0000289726.35330.8A

60.    GAFchromic. Garchromic EBT Films - GAFchromic™. Accessed March 3, 2023. http://www.gafchromic.com/gafchromic-film/radiotherapy-films/EBT/index.asp

61.    IBA Dosimetry. *Detectors For Relative and Absolute Dosimetry Ionization Chambers and Diode Detectors Iba-Dosimetry.Com*.; 2018.

62.    Sun Nuclear Corporation. *EDGE Detector ™ User Guide Scanning Diode for Water Tank Phantoms*.; 1118. www.sunnuclear.com

63.    PTW-Freiburg. *Ionizing Radiation Detectors Including Codes of Practice*. PTW The Dosimetry Company; 2012. Accessed March 6, 2023. https://www.ptwdosimetry.com/en/

64.    PTW-Freiburg. *Radiation Medicine QA Solutions*. PTW The dosimetry Company; 2019. Accessed March 6, 2023. https://www.ptwdosimetry.com/en/

65.    PTW-Freiburg. *Ionizing Radiation Detectors Including Codes of Practice*. PTW The Dosimetry Company; 2019. Accessed March 6, 2023. https://www.ptwdosimetry.com/en/

66.    Standard Imaging. Exradin® W2 Scintillator | Standard Imaging. Accessed April 14, 2023. https://www.standardimaging.com/exradin-detectors/scintillators

67.    Sun Nuclear. EDGE Detector™ - Sun Nuclear. Accessed March 13, 2023. https://www.sunnuclear.com/products/edge-detector

68.    Exradin® W2 Scintillator | Standard Imaging. Accessed March 29, 2023. https://www.standardimaging.com/exradin-detectors/scintillators

69.    Radiology Key. Ionization chamber | Radiology Key. Accessed March 6, 2023. https://radiologykey.com/ionization-chamber/

70.    Kim YK, Park SH, Kim HS, et al. Polarity effect of the thimble-type ionization chamber at a low dose rate. *Phys Med Biol*. 2005;50(21):4995-5003. doi:10.1088/0031-9155/50/21/003

71.    Crop F. The influence of small field sizes, penumbra, spot size and measurement depth on perturbation factors for microionization chambers. Published online 2009. doi:10.1088/0031-9155/54/9/024

72.    Dalla Betta GF, Ye J. Silicon Radiation Detector Technologies: From Planar to 3D. *Chips*. 2023;2(2):83-101. doi:10.3390/chips2020006

73.    Shimaoka T, Koizumi S, J. H., Kaneko. Recent progress in diamond radiation detectors. *Functional Diamond*. 2021;1(1):205-220. doi:10.1080/26941112.2021.2017758

74.    Kania DR, Landstrass MI, Piano MA, Pan LS, Han S. *Diamond Radiation Detectors*. Vol 2.; 1993.

75. Hršak H. *Dozimetrija Uskih Fotonskih Snopova u Stereotaktičkoj Neuroradiokirurgiji Gama Nožem*. Prirodoslovno - matematički fakultet; 2015.

76. Devic S, Seuntjens J, Hegyi G, et al. Dosimetric properties of improved GafChromic films for seven different digitizers. *Med Phys*. 2004;31(9):2392-2401. doi:10.1118/1.1776691

77. Niroomand-Rad A, Chiu-Tsao ST, Grams MP, et al. Report of AAPM Task Group 235 Radiochromic Film Dosimetry: An Update to TG-55. *Med Phys*. 2020;47(12):5986-6025. doi:10.1002/MP.14497

78. Phaisangittisakul N, Ma L. An empirical model for independent dose verification of the Gamma Knife treatment planning. *Med Phys*. 2002;29(9):1991-1997. doi:10.1118/1.1501139

79. Farrance I, Frenkel R. Uncertainty of Measurement: A Review of the Rules for Calculating Uncertainty Components through Functional Relationships. *Clin Biochem Rev*. 2012;33.

80. JCGM. Evaluation of measurement data-Guide to the expression of uncertainty in measurement Évaluation des données de mesure-Guide pour l'expression de l'incertitude de mesure. Published online 2008. Accessed July 18, 2023. www.bipm.org

81. PTW - FREIBURG. *User Manual, UNIDOS E PTW-Universal Dosimeter*.; 2014. doi:545.131.00/06

82. IBA Dosimetry. DOSE 1 High Performance Reference Class Electrometer Significantly exceeds IEC 60731 and AAPM ADCL Recommendations.

83. Rudek B, Bernstein K, Osterman S, Qu T. Replacing gamma knife beam-profiles on film with point-detector scans. *J Appl Clin Med Phys*. 2022;23(3):e13522. doi:10.1002/ACM2.13522

84. G. Lufft Mess- und Regeltechnik GmbH Fellbach. *Technical Data OPUS 20 THI*.; 2023.

85. Clements JB, Baird CT, de Boer SF, et al. AAPM medical physics practice guideline 10.a.: Scope of practice for clinical medical physics. *J Appl Clin Med Phys*. 2018;19(6):11-25. doi:10.1002/ACM2.12469

86. Petti PL, Rivard MJ, Alvarez PE, et al. Recommendations on the practice of calibration, dosimetry, and quality assurance for gamma stereotactic radiosurgery: Report of AAPM Task Group 178. *Med Phys*. 2021;48(7):e733-e770. doi:10.1002/MP.14831

87. Butson MJ, Cheung T, Yu PKN. Scanning orientation effects on Gafchromic EBT film dosimetry. *Australas Phys Eng Sci Med*. 2006;29.

88. Petti PL, Rivard MJ, Alvarez PE, et al. Recommendations on the practice of calibration, dosimetry, and quality assurance for gamma stereotactic radiosurgery: Report of AAPM Task Group 178. *Med Phys*. 2021;48(7):e733-e770. doi:10.1002/MP.14831

89. Casar B, Mendez I, Gershkevitsh E, et al. On dosimetric characteristics of detectors for relative dosimetry in small fields: a multicenter experimental study. *Phys Med Biol*. Published online December 13, 2023. doi:10.1088/1361-6560/AD154C

90. Ager WH¨, Kaveckyte V, Benmakhlouf H. Experimental investigation of TRS-483 reference dosimetry correction factors for Leksell Gamma Knife ® Icon ™ beams. Published online 2020. doi:10.1002/mp.14561

91. Cyriac SL, Liu J, Calugaru E, Chang J. A novel and effective method for validation and measurement of output factors for Leksell Gamma Knife® Icon™ using TRS 483 protocol. *J Appl Clin Med Phys*. 2020;21(10):80-88. doi:10.1002/ACM2.13011

# Appendix A

Detector schematics presented in this Appendix are relevant to the calculation of volume-averaging and are presented only for fallowing detectors:

- PTW Semiflex T31010
- PTW Semiflex 3D T31021
- PTW PinPoint T31014
- PTW PinPoint 3D T31016
- RAZOR chamber
- RAZORnano chamber
- CC04 chamber

These schematics are kindly provided by the PTW Freiburg, Germany as well as IBA Dosimetry Schwarzenbruck. The remaining detectors have simpler geometers being disk (cylinder) or rectangular shaped. For these detectors data provided in Table 10. are sufficient.
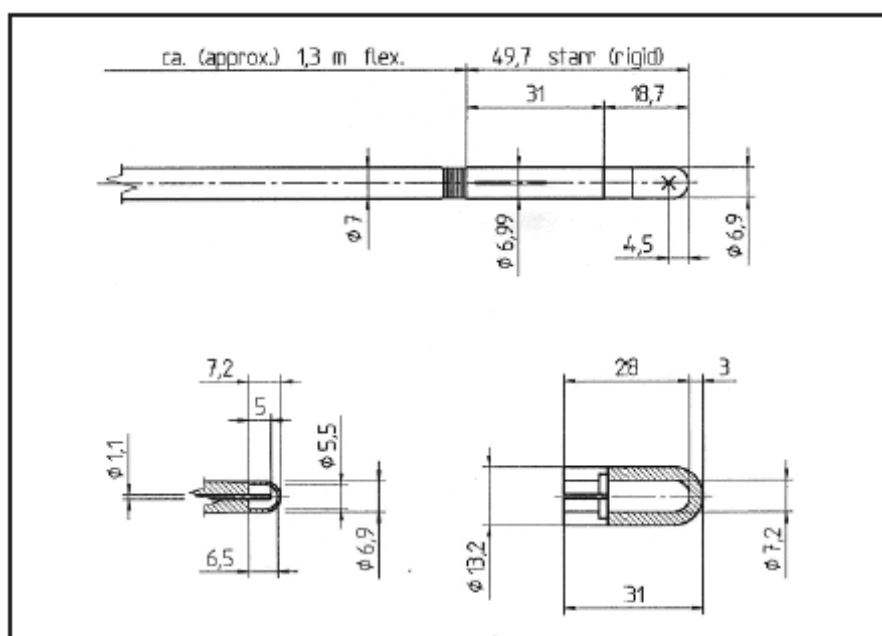


0.125 cm³ Semiflex Chamber                    31010
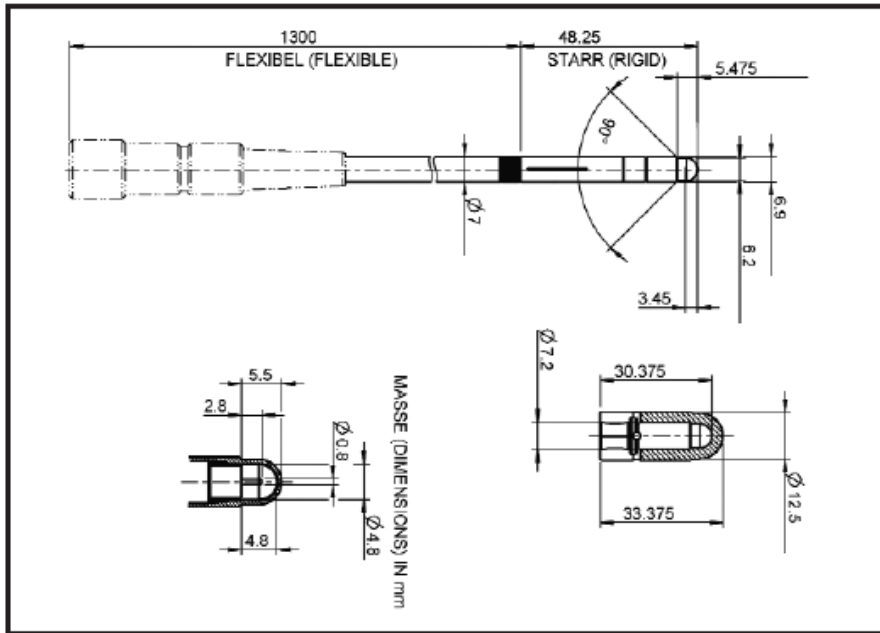
0.07 cm³ Semiflex 3D Chamber       31021
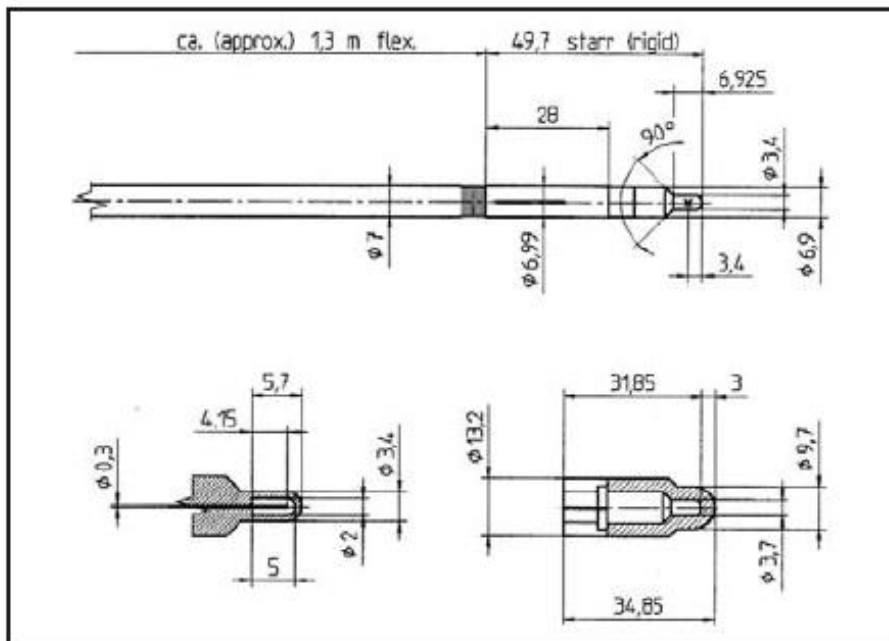


PinPoint Chamber       31014
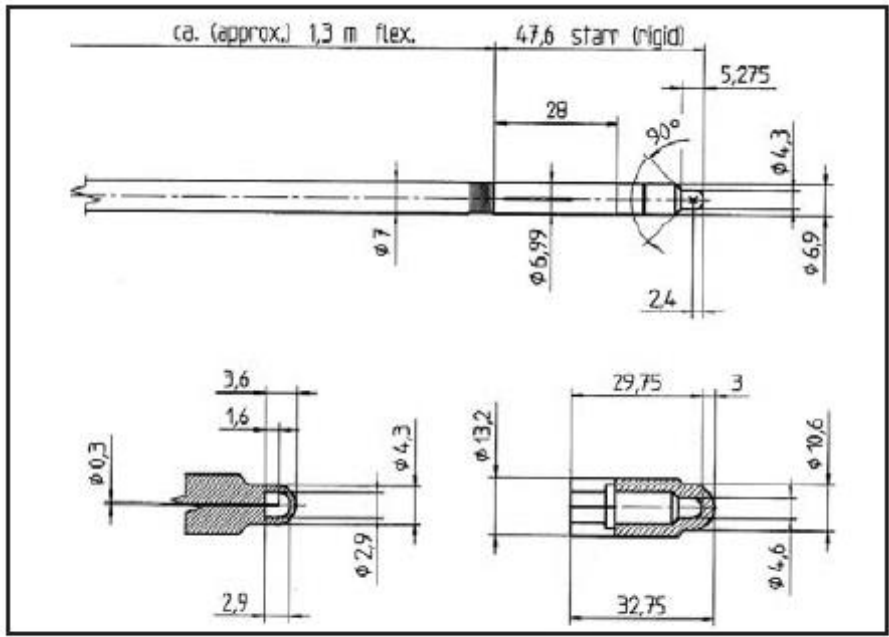
PinPoint 3D Chamber                              31016
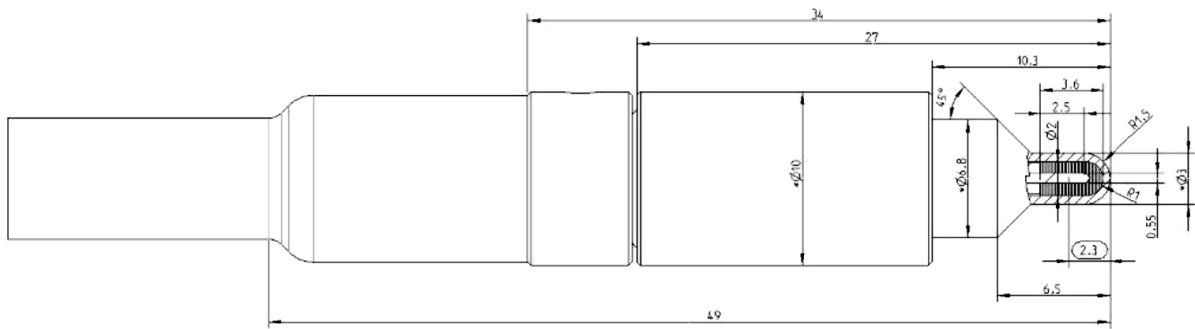


*Dimensions of the RAZOR<sup>Chamber</sup> (dimensions in mm, add 0.2 mm for tolerance if you intend to make adapters)*
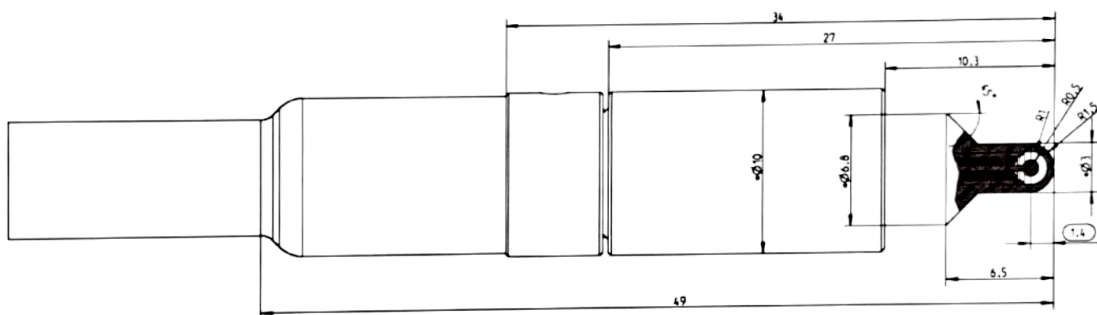


*Dimensions of the RAZOR Nano <sup>Chamber</sup> (dimensions in mm, add 0.2 mm tolerance if you intend to make adapters)*
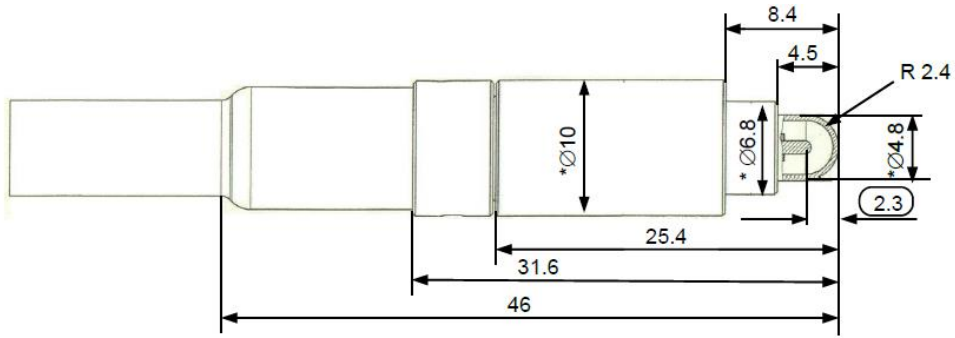
Dimensions of CC04 (dimensions in mm, add 0.2 mm for tolerance if you intend to make adapters)

# Appendix B

A computer code written in MATLAB for the calculation of volume-averaging on Gamma Knife Perfexion for detectors studied in this thesis is provided in this Appendix. The written program calculates volume-averaging correction factor for the following detectors:

- PTW Semiflex T31010
- PTW Semiflex 3D T31021
- PTW PinPoint T31014
- PTW PinPoint 3D T31022
- PTW Diode P T60016
- PTW Diode E T60017
- PTW microDiamond T60019
- IBA RAZOR diode
- IBA RAZOR chamber
- IBA CC04
- EDGE detector
- EFD diode

```matlab
%Calculation of a volume averaging on Gamma Knife
digits(32)
format short
polje=menu('Please select the field size for which volume averaging is calculated',' 16 mm','8
mm','4 mm'); %select the field size
if polje == 1 %16 mm field
%Coefficients for s direction in a cylindrical coordinate system - x direction is fitted from
Leksell coordinate system
c0s =  9.69539388004509E-01;
A1s =  3.81762920289576E-01;
a1s =  2.49913438196976E+01;
b1s =  -1.67550520977859E+00;
A2s =  -2.03591059391798E-01;
a2s =  -8.94687901300991E+00;
b2s =  1.92626666629579E+00;
A3s =  -1.02427191560397E-02;
a3s =  5.32940693032982E+00;
b3s =  4.91979665382671E+01;
A4s =  2.09537779074513E-01;
a4s =  -1.24942845009386E+01;
b4s =  -4.58390178363538E+00;

%Coefficients for z direction in a cylindrical coordinate system - z direction is fitted from
Leksell coordinate system
c0z =  6.23439585197441E-02;
A1z =  1.65016076148551E+00;
a1z =  -6.64266771664852E+00;
b1z =  -2.54636160615763E+00;
A2z =  1.75606701707450E+00;
a2z =  -5.60760279869319E+00;
b2z =  -1.76766384666806E+00;
A3z =  2.97263968316475E+00;
a3z =  -5.79821291403295E+00;
b3z =  1.93643475942725E+00;
A4z =  -3.39734861765111E-03;
a4z =  1.89356823656770E-01;
b4z =  1.17416975626696E+00;
A5z =  4.67330039984927E-01;
a5z =  8.76144173778636E+00;
b5z =  1.80287660180637E+00;
A0z =  3.12810092663561E-02;
az =   -4.71330838427608E+00;
bz =   -7.59998845310368E-01;
else if polje == 2 %8 mm polje
%Coefficients for s direction in a cylindrical coordinate system - x direction is fitted from
Leksell coordinate system
c0s =  5.03635710695764E-01;
```

```matlab
48      A1s =   9.88325720443460E-02;
49      a1s =  -8.01982219971946E+00;
50      b1s =  -4.03898164613522E+00;
51      A2s =   5.27104129024405E-02;
52      a2s =  -1.36396115774001E+01;
53      b2s =  -9.40368469738407E+00;
54      A3s =   2.35344836867871E-01;
55      a3s =  -5.37881836259153E+00;
56      b3s =  -2.18398489903176E+00;
57      A4s =   1.12806315029468E-01;
58      a4s =  -4.58912556690278E+00;
59      b4s =  -1.06379030441735E+00;
60
61      %Coefficients for z direction in a cylindrical coordinate system - z direction is fitted from
62      Leksell coordinate system
63      c0z =   1.15950725257977E+00;
64      A1z =  -5.92978414412138E+00;
65      a1z =  -5.36550589710118E+00;
66      b1z =  -1.08424553524007E+02;
67      A2z =  -4.67178392213500E-01;
68      a2z =   4.67455624404566E+00;
69      b2z =  -1.84823205607355E+00;
70      A3z =   4.83205221309876E-01;
71      a3z =  -5.04296136055748E+00;
72      b3z =  -1.84831005046076E+00;
73      A4z =  -4.78929405327008E+00;
74      a4z =  -4.30280110051637E+00;
75      b4z =   8.53827968025802E+01;
76      A5z =  -3.69804960557376E-02;
77      a5z =   7.56801950098436E+00;
78      b5z =  -3.60316445872631E+00;
79      A0z =   1.34532865234678E+00;
80      az =   -2.51279085600255E+00;
81      bz =    2.69871447884177E+00;
82          else if polje == 3 %4 mm polje
83      %Coefficients for s direction in a cylindrical coordinate system - x direction is fitted from
84      Leksell coordinate system
85      c0s =   5.33262345742450E-01;
86      A1s =   2.66410381382869E-01;
87      a1s =  -2.59032772830263E+00;
88      b1s =  -1.19772081535829E+00;
89      A2s =   8.47103711400306E-02;
90      a2s =  -5.30783226357609E+00;
91      b2s =  -7.40969527700572E+00;
92      A3s =   1.49732918683219E-01;
93      a3s =  -4.03070534843962E+00;
94      b3s =  -2.33322160403931E+00;
```

136

```
95    A4s =  -6.15704845438336E-02;
96    a4s =  5.29242467969531E+00;
97    b4s =  7.00442818850188E+01;
98
99    %Coefficients for z direction in a cylindrical coordinate system - z direction is fitted from
100   Leksell coordinate system
101   c0z =  3.81570813736090E-02;
102   A1z =  4.80640052626926E-01;
103   a1z =  -2.48998145956572E+00;
104   b1z =  -1.24629020543953E+00;
105   A2z =  4.79647659835712E-01;
106   a2z =  2.50218824713077E+00;
107   b2z =  1.20777444317923E+00;
108       end
109     end
110   end
111   %List of variables:
112   %     rr1 - Vector in cylindrical coordinate system
113   %     fss - Dose profile in s direction with "s" variable
114   %     fs1 - Dose profile in s direction with "rr1" variable
115   %     fzz - Dose profile in z direction with "z" variable
116   %     fz1 - Dose profile in +z direction with "rr1&rr2" variable
117   %     fz2 - Dose profile in -z direction with "rr1&rr2" variable
118   %     raspodjela - distribution in an elliptical model
119   %     s0 - shift in field in s direction
120   %     z0 - shift in field in z direction
121   %     z1(s) - initial point of integration of an cylindrical part of
122   %     detector
123   %     z2(s) - final point of integration of an cylindrical part of an
124   %     detector
125   %     z3(s) - length of an electrode above the xy plain determined by
126   %     the reference point
127   %     s1 - initial point of integration of an detector/electrode
128   %     s2 - detector radius
129   %     s3 - radius of an electrode
130   %     z00(s) - defines zero so we can integrate on both z profiles
131   %     zf - function that describes the curvature of an chamber
132   %     n - number of steps of integration in s direction
133   %     m - number of steps of integration in z direction
134   %     f1 - distribution for z>0 and differential for integration in
135   %     cylindrical coordinate system is added at the end
136   %     f2 - distribution for z<0 and differential for integration in
137   %     cylindrical coordinate system is added at the end
138   %     Juk1 - value of an integral of a cylinder in the area z>0 to the
139   %     curved part of chamber
140   %     Juk2 - value of an integral of a cylinder in the area z<0 to the
141   %     curved part of chamber
```

```matlab
142    %      Juk3 - integral of a cylindrical electrode in the area z>0
143    %      Juk4 - integral of a cylindrical electrode in the area z<0
144    %      Juk5 - integral of a curved part
145    syms s
146    z00=@(s) 0;
147    n=100;
148    m=100;
149
150    k=menu('Select the detector to calculate volume averaging','Semiflex TM31010', 'PinPoint
151    TM31014','Dioda P T60016','Dioda E T60017','PinPoint 3D T31022',...
152      'microDiamond T60019','EDGE Detector','EFD diode','RAZOR diode detector','RAZOR
153    chamber','%RAZORnano chamber','Semiflex 3D','IBA CC04', 'Exradin W2 1X1','Excradin W3
154    1X3');
155    if k==1 %Semiflex T31010
156       z1=@(s) -2.7; %length of a detector in z<0
157       z2=@(s) 1.05; %length of a detector in z>0 (only cylindrical part)
158       z3=@(s) 2.3; %length of an electrode above z>0
159       s1=0.0001; %initial point of an integration of a detector
160       s2=2.75; %detector's radius
161       s3=0.55; %radius of an electrode
162       zf=@(s) sqrt(7.5625-s.^2); %function that describes the radius of curvature of a top part
163       V=128; %volume in mm3
164    else if k==2 %PinPoint T31014
165          z1=@(s) -2.3;
166          z2=@(s) 2.4294;
167          z3=@(s) 1.85;
168          s1=0.0001;
169          s2=1;
170          s3=0.15;
171          zf=@(s)sqrt(3.9326-s.^2)-1.71;
172          V=15;
173    else if k==3 %Diode P T60016
174          z1=@(s) -0.015;
175          z2=@(s) 0.015;
176          z3=@(s) 0;
177          s1=0.0001;
178          s2=0.56418;
179          s3=0;
180          zf=@(s) 0;
181          V=0.03;
182      else if k==4 %Diode E T60017
183          z1=@(s) -0.015;
184          z2=@(s) 0.015;
185          z3=@(s) 0;
186          s1=0.0001;
187          s2=0.56418;
188          s3=0;
```

```
189        zf=@(s)0;
190        V=0.03;
191        else if k==5 %PinPoint 3D TM31022
192            z1=@(s) -0.175;
193            z2=@(s) 1.7676;
194            z3=@(s) 1.425;
195            zf=@(s) sqrt(2.4649-s.^2)-0.6192;
196            s1=0.0001;
197            s2=1.45;
198            s3=0.3;
199            V=16;
200          else if k==6 %microDiamond TM60019
201            z1=@(s) -5*10^(-7);
202            z2=@(s) 5*10^(-7);
203            z3=@(s) 0;
204            s1=0.0001;
205            s2=1.1;
206            s3=0;
207            zf=@(s) 0;
208            V=3.801*10^(-6);
209          else if k==7 %EDGE detector
210              xmin=-0.4;
211              xmax=0.4;
212              ymin=-0.015;
213              ymax=0.015;
214              zmin=-0.4;
215              zmax=0.4;
216              V=0.0192;
217            else if k==8 %EFD diode
218                z1=@(s) -0.03;
219                z2=@(s) 0.03;
220                z3=@(s) 0;
221                s1=0.0001;
222                s2=1;
223                s3=0;
224                zf=@(s) 0;
225                V=0.1885;
226              else if k==9 %RAZOR diode
227                  z1=@(s) -0.01;
228                  z2=@(s) 0.01;
229                  z3=@(s) 0;
230                  s1=0.0001;
231                  s2=0.3;
232                  s3=0;
233                  zf=@(s) 0;
234                  V=5.655*10^(-3);
235                else if k==10 %RAZOR chamber
```

```
236                    z1=@(s) -1.8;
237                    z2=@(s) 0.8;
238                    z3=@(s) 0.7;
239                    s1=0.0001;
240                    s2=1;
241                    s3=0.275;
242                    zf=@(s) sqrt(1.001-s.^2);
243                    V=9.668;
244            % else if k==11; %RAZORnano chamber
245                    z1=@(s) 0;
246                    z2=@(s) 0;
247                    z3=@(s) 0;
248                    s1=0.0001;
249                    s2=1;
250                    s3=0.5;%radius of an  spherical electrode
251                    zf=@(s) sqrt(1-s.^2);
252                    zf2=@(s) sqrt(0.5.^2-s.^2);
253                    V=3.665;
254              else if k==12 %Semiflex 3D T31021
255                    z1=@(s) -2.05;
256                    z2=@(s) 0.75;
257                    z3=@(s)0.75;
258                    s1=0.00001;
259                    s2=2.4;
260                    s3=0.4;
261                    zf=@(s) sqrt(5.76-s.^2)-0.4;
262                    V=71.04;
263                else if k==13 %IBA CC04
264                    z1=@(s) -1.6;
265                    z2=@(s) 0;
266                    z3=@(s) 0.5;
267                    s1=0.00001;
268                    s2=2;
269                    s3=0.5;
270                    zf=@(s) sqrt(4-s.^2);
271                    V=35.37;
272                  else if k==14; %Exradin W2 1X1
273                        z1=@(s) -0.5;
274                        z2=@(s) 0.5;
275                        z3=@(s) 0;
276                        s1=0.0001;
277                        s2=0.5;
278                        s3=0;
279                        zf=@(s)0;
280                        V=0.7854;
281                     else if k==15 %Exradin W2 1X3
282                        z1=@(s) -1.5;
```

```matlab
283                                    z2=@(s) 1.5;
284                                    z3=@(s) 0;
285                                    s1=0.0001;
286                                    s2=0.5;
287                                    s3=0;
288                                    zf=@(s)0;
289                                    V=2.3562;
290                                     end
291                                   end
292                                  end
293                                 end
294                               end
295                              end
296                            end
297                          end
298                        end
299                      end
300                    end
301                  end
302              end
303              end
304        end
305
306        if polje ==1
307            disp('16 mm field')
308        else if polje ==2
309                disp('8 mm field')
310            else if polje ==3
311                    disp('4 mm field')
312            end
313            end
314        end
315
316
317        x0=0; y0=0; z0=0;
318
319        if polje == 1 || polje == 2
320
321            if k==7
322        fx=@(x)
323        (c0s+A1s.*erf((x+a1s)./b1s)+A2s.*erf((x+a2s)./b2s)+A3s.*erf((x+a3s)./b3s)+A4s.*erf((x+a4s)./
324        b4s));
325        fy=@(y)
326        (c0s+A1s.*erf((y+a1s)./b1s)+A2s.*erf((y+a2s)./b2s)+A3s.*erf((y+a3s)./b3s)+A4s.*erf((y+a4s).
327        /b4s));
328        fzz=@(z)(c0z+A1z.*erf((z+a1z)./b1z)+A2z.*erf((z+a2z)./b2z)+A3z.*erf((z+a3z)./b3z)+A4z.*erf(
329        (z+a4z)./b4z)+A5z.*erf((z+a5z)./b5z)+A0z.*erf(az./bz));
```

```
330    rr2=@(x,y,z)sqrt((x-x0).^2+(y-y0).^2+(z-z0).^2);
331    fxx=@(x,y,z)
332    (c0s+A1s.*erf((rr2(x,y,z)+a1s)./b1s)+A2s.*erf((rr2(x,y,z)+a2s)./b2s)+A3s.*erf((rr2(x,y,z)+a3s)./
333    b3s)+A4s.*erf((rr2(x,y,z)+a4s)./b4s));
334    fyy=@(x,y,z)
335    (c0s+A1s.*erf((rr2(x,y,z)+a1s)./b1s)+A2s.*erf((rr2(x,y,z)+a2s)./b2s)+A3s.*erf((rr2(x,y,z)+a3s)./
336    b3s)+A4s.*erf((rr2(x,y,z)+a4s)./b4s));
337    fz1=@(x,y,z)(c0z+A1z.*erf((rr2(x,y,z)+a1z)./b1z)+A2z.*erf((rr2(x,y,z)+a2z)./b2z)+A3z.*erf((rr2
338    (x,y,z)+a3z)./b3z)+A4z.*erf((rr2(x,y,z)+a4z)./b4z)+A5z.*erf((rr2(x,y,z)+a5z)./b5z)+A0z.*erf(az.
339    /bz));
340    fz2=@(x,y,z)(c0z+A1z.*erf((-rr2(x,y,z)+a1z)./b1z)+A2z.*erf((-rr2(x,y,z)+a2z)./b2z)+A3z.*erf((-
341    rr2(x,y,z)+a3z)./b3z)+A4z.*erf((-rr2(x,y,z)+a4z)./b4z)+A5z.*erf((-
342    rr2(x,y,z)+a5z)./b5z)+A0z.*erf(az./bz));
343    fedgeplus=@(x,y,z) sqrt((fxx(x,y,z).*abs(x-x0)./rr2(x,y,z)).^2+(fyy(x,y,z).*abs(y-
344    y0)./rr2(x,y,z)).^2+(fz1(x,y,z).*abs(z-z0)./rr2(x,y,z)).^2);
345    fedgeminus=@(x,y,z) sqrt((fxx(x,y,z).*abs(x-x0)./rr2(x,y,z)).^2+(fyy(x,y,z).*abs(y-
346    y0)./rr2(x,y,z)).^2+(fz2(x,y,z).*abs(z-z0)./rr2(x,y,z)).^2);
347
348    integral1=triplequad(fedgeplus,xmin,xmax,ymin,ymax,0.0000001,zmax);
349    integral2=triplequad(fedgeminus,xmin,xmax,ymin,ymax,zmin,-0.0000001);
350    disp('Volume averaging for EDGE detector is: ')
351    kvol=V/(integral1+integral2) %kvol for EDGE detector
352    return
353        end
354    s0=sqrt(x0.^2+y0.^2);
355    rr1=@(s,z) sqrt((s-s0).^2+(z-z0).^2);
356    %function for s direction for 16 & 8 mm field
357    fss=@(s)
358    (c0s+A1s.*erf((s+a1s)./b1s)+A2s.*erf((s+a2s)./b2s)+A3s.*erf((s+a3s)./b3s)+A4s.*erf((s+a4s)./
359    b4s));
360    fs1=@(s,z)
361    (c0s+A1s.*erf((rr1(s,z)+a1s)./b1s)+A2s.*erf((rr1(s,z)+a2s)./b2s)+A3s.*erf((rr1(s,z)+a3s)./b3s)+
362    A4s.*erf((rr1(s,z)+a4s)./b4s));
363
364    %function for z direction for 16%8 mm field size
365    fzz=@(z)(c0z+A1z.*erf((z+a1z)./b1z)+A2z.*erf((z+a2z)./b2z)+A3z.*erf((z+a3z)./b3z)+A4z.*erf(
366    (z+a4z)./b4z)+A5z.*erf((z+a5z)./b5z)+A0z.*erf(az./bz));
367    fz1=@(s,z)(c0z+A1z.*erf((rr1(s,z)+a1z)./b1z)+A2z.*erf((rr1(s,z)+a2z)./b2z)+A3z.*erf((rr1(s,z)+
368    a3z)./b3z)+A4z.*erf((rr1(s,z)+a4z)./b4z)+A5z.*erf((rr1(s,z)+a5z)./b5z)+A0z.*erf(az./bz));
369    fz2=@(s,z)(c0z+A1z.*erf((-rr1(s,z)+a1z)./b1z)+A2z.*erf((-rr1(s,z)+a2z)./b2z)+A3z.*erf((-
370    rr1(s,z)+a3z)./b3z)+A4z.*erf((-rr1(s,z)+a4z)./b4z)+A5z.*erf((-
371    rr1(s,z)+a5z)./b5z)+A0z.*erf(az./bz));
372
373    %distribution
374    f1=@(s,z) sqrt((fs1(s,z).*abs(s-s0)./rr1(s,z)).^2+(fz1(s,z).*abs(z-z0)./rr1(s,z)).^2)*s;
375    f2=@(s,z) sqrt((fs1(s,z).*abs(s-s0)./rr1(s,z)).^2+(fz2(s,z).*abs(z-z0)./rr1(s,z)).^2)*s;
376
```

```matlab
377    else if polje == 3
378
379        if k==7
380    fx=@(x)
381    (c0s+A1s.*erf((x+a1s)./b1s)+A2s.*erf((x+a2s)./b2s)+A3s.*erf((x+a3s)./b3s)+A4s.*erf((x+a4s)./
382    b4s));
383    fy=@(y)
384    (c0s+A1s.*erf((y+a1s)./b1s)+A2s.*erf((y+a2s)./b2s)+A3s.*erf((y+a3s)./b3s)+A4s.*erf((y+a4s).
385    /b4s));
386    fzz=@(z)(c0z+A1z.*erf((z+a1z)./b1z)+A2z.*erf((z+a2z)./b2z));
387    rr2=@(x,y,z)sqrt((x-x0).^2+(y-y0).^2+(z-z0).^2);
388    fxx=@(x,y,z)
389    (c0s+A1s.*erf((rr2(x,y,z)+a1s)./b1s)+A2s.*erf((rr2(x,y,z)+a2s)./b2s)+A3s.*erf((rr2(x,y,z)+a3s)./
390    b3s)+A4s.*erf((rr2(x,y,z)+a4s)./b4s));
391    fyy=@(x,y,z)
392    (c0s+A1s.*erf((rr2(x,y,z)+a1s)./b1s)+A2s.*erf((rr2(x,y,z)+a2s)./b2s)+A3s.*erf((rr2(x,y,z)+a3s)./
393    b3s)+A4s.*erf((rr2(x,y,z)+a4s)./b4s));
394    fz1=@(x,y,z)(c0z+A1z.*erf((rr2(x,y,z)+a1z)./b1z)+A2z.*erf((rr2(x,y,z)+a2z)./b2z));
395    fz2=@(x,y,z)(c0z+A1z.*erf((-rr2(x,y,z)+a1z)./b1z)+A2z.*erf((-rr2(x,y,z)+a2z)./b2z));
396    fedgeplus=@(x,y,z) sqrt((fxx(x,y,z).*abs(x-x0)./rr2(x,y,z)).^2+(fyy(x,y,z).*abs(y-
397    y0)./rr2(x,y,z)).^2+(fz1(x,y,z).*abs(z-z0)./rr2(x,y,z)).^2);
398    fedgeminus=@(x,y,z) sqrt((fxx(x,y,z).*abs(x-x0)./rr2(x,y,z)).^2+(fyy(x,y,z).*abs(y-
399    y0)./rr2(x,y,z)).^2+(fz2(x,y,z).*abs(z-z0)./rr2(x,y,z)).^2);
400
401    integral1=triplequad(fedgeplus,xmin,xmax,ymin,ymax,0.0000001,zmax);
402    integral2=triplequad(fedgeminus,xmin,xmax,ymin,ymax,zmin,-0.0000001);
403    disp('Volume avearging for EDGE SunNuclear detector is: ')
404    kvol=V/(integral1+integral2) %kvol for EDGE detector
405        return
406        end
407
408    s0=sqrt(x0.^2+y0.^2);
409    rr1=@(s,z) sqrt((s-s0).^2+(z-z0).^2);
410    %functions for s direction foe 4 mm field
411    fss=@(s)
412    (c0s+A1s.*erf((s+a1s)./b1s)+A2s.*erf((s+a2s)./b2s)+A3s.*erf((s+a3s)./b3s)+A4s.*erf((s+a4s)./
413    b4s));
414    fs1=@(s,z)
415    (c0s+A1s.*erf((rr1(s,z)+a1s)./b1s)+A2s.*erf((rr1(s,z)+a2s)./b2s)+A3s.*erf((rr1(s,z)+a3s)./b3s)+
416    A4s.*erf((rr1(s,z)+a4s)./b4s));
417
418    %functions for z direction for 4 mm field
419    fzz=@(z)(c0z+A1z.*erf((z+a1z)./b1z)+A2z.*erf((z+a2z)./b2z));
420    fz1=@(s,z)(c0z+A1z.*erf((rr1(s,z)+a1z)./b1z)+A2z.*erf((rr1(s,z)+a2z)./b2z));
421    fz2=@(s,z)(c0z+A1z.*erf((-rr1(s,z)+a1z)./b1z)+A2z.*erf((-rr1(s,z)+a2z)./b2z));
422
423    %rdistributions
```

```matlab
424    f1=@(s,z) sqrt((fs1(s,z).*abs(s-s0)./rr1(s,z)).^2+(fz1(s,z).*abs(z-z0)./rr1(s,z)).^2)*s;
425    f2=@(s,z) sqrt((fs1(s,z).*abs(s-s0)./rr1(s,z)).^2+(fz2(s,z).*abs(z-z0)./rr1(s,z)).^2)*s;
426
427      end
428    end
429
430    if k==1
431       disp('Volume averaging for Semiflex TM31010 is: ')
432    else if k==2
433        disp('Volume averaging for PinPoint T31014 is: ')
434    else if k==3
435         disp('Volume averaging for Diode P T60016 is: ')
436    else if k==4
437          disp('Volume averaging for Diode E T60017 is: ')
438    else if k==5
439           disp('Volume averaging for PinPoint 3D T31022 is: ')
440    else if k==6
441            disp('Volume averaging for microDiamond T60019 is: ')
442    else if k==8
443             disp('Volume averaging for EFD is: ')
444    else if k==9
445              disp('Volume averaging for RAZOR diode is: ')
446    else if k==10
447               disp('Volume averaging for RAZOR chamber is: ')
448    else if k==11
449                disp('Volume averaging for RAZORnano chamber is: ')
450    else if k==12
451               disp('Volume averaging for Semiflex 3D T31021 is: ')
452    else if k==13
453             disp('Volume averaging for IBA CC04 is: ')
454    else if k==14
455           disp('Volume averaging for Exradin W2 1X1 is: ')
456    else if k==15
457         disp('Volume averaging for Exradin W2 1X3 is: ')
458                              end
459                             end
460                            end
461                           end
462                          end
463                         end
464                        end
465                       end
466                      end
467                     end
468                    end
469                   end
470                  end
```

```matlab
471     end



475     if k~=11 % to exclude nanochamber since it had different geometry

477        h=(s2-s1)/n; % integral for the cylinder in the area z>0
478        J1=0; J2=0; J3=0;
479        for i=0:n
480        s = s1 + i*h;
481        HX = (z2(s)-z00(s))/m;
482        K1 = f1(s, z00(s))+f1(s, z2(s));
483        K2 = 0; K3 =0;
484        for j=1:m-1
485         z = z00(s) + j*HX;
486         Q = f1(s,z);
487         if rem(j,2) == 0
488            K2 = K2 + Q;
489         else
490            K3 = K3 + Q;
491         end
492        end
493        L = (K1 + 2*K2 + 4*K3)*HX/3;
494        if  i == 0 || i == n
495           J1 = J1 + L;
496        else if rem(i,2) == 0
497             J2 = J2 + L;
498        else
499           J3 = J3 + L;
500          end
501        end
502        end
503        Juk1 = 2 * pi* h * (J1 + 2*J2 + 4*J3)/3;

505        h=(s2-s1)/n; %integral for the cylinder in the area z<0
506        J1=0; J2=0; J3=0;
507        for i=0:n
508        s = s1 + i*h;
509        HX = (z00(s)-z1(s))/m;
510        K1 = f2(s, z1(s))+f2(s, z00(s));
511        K2 = 0; K3 =0;
512        for j=1:m-1
513         z = z1(s) + j*HX;
514         Q = f2(s,z);
515         if rem(j,2) == 0
516            K2 = K2 + Q;
517         else
```

```matlab
518          K3 = K3 + Q;
519       end
520      end
521      L = (K1 + 2*K2 + 4*K3)*HX/3;
522      if  i == 0 || i == n
523         J1 = J1 + L;
524      else if rem(i,2) == 0
525            J2 = J2 + L;
526      else
527         J3 = J3 + L;
528          end
529      end
530      end
531      Juk2 = 2 * pi * h * (J1 + 2*J2 + 4*J3)/3;
532
533      h=(s3-s1)/n; %integral for the electrode in the area z>0
534      J1=0; J2=0; J3=0;
535      for i=0:n
536      s = s1 + i*h;
537      HX = (z3(s)-z00(s))/m;
538      K1 = f1(s, z00(s))+f1(s, z3(s));
539      K2 = 0; K3 =0;
540      for j=1:m-1
541       z = z00(s) + j*HX;
542       Q = f1(s,z);
543       if rem(j,2) == 0
544          K2 = K2 + Q;
545       else
546          K3 = K3 + Q;
547       end
548      end
549      L = (K1 + 2*K2 + 4*K3)*HX/3;
550      if  i == 0 || i == n
551         J1 = J1 + L;
552      else if rem(i,2) == 0
553            J2 = J2 + L;
554      else
555         J3 = J3 + L;
556          end
557      end
558      end
559      Juk3 = 2 * pi* h * (J1 + 2*J2 + 4*J3)/3;
560
561      h=(s3-s1)/n; %integral for the electrode in the area z<0
562      J1=0; J2=0; J3=0;
563      for i=0:n
564      s = s1 + i*h;
```

```matlab
565        HX = (z00(s)-z1(s))/m;
566        K1 = f2(s, z1(s))+f2(s, z00(s));
567        K2 = 0; K3 =0;
568        for j=1:m-1
569         z = z1(s) + j*HX;
570         Q = f2(s,z);
571         if rem(j,2) == 0
572            K2 = K2 + Q;
573         else
574            K3 = K3 + Q;
575         end
576        end
577        L = (K1 + 2*K2 + 4*K3)*HX/3;
578        if  i == 0 || i == n
579           J1 = J1 + L;
580        else if rem(i,2) == 0
581             J2 = J2 + L;
582        else
583           J3 = J3 + L;
584          end
585        end
586        end
587        Juk4 = 2 * pi * h * (J1 + 2*J2 + 4*J3)/3;
588
589      if k==1 % moving the field so the curvature part of a chamber could be in the right place
590        z0=-z0-1.05;
591    else if k==2
592            z0=-z0-2.4294;
593         else if k==5
594               z0=-z0-0.275;
595            else if k==10
596                  z0=-z0-0.8;
597               else if k==12
598                    z0=-z0-0.75;
599                  end
600                end
601             end
602             end
603      end
604
605      rr1=@(s,z) sqrt((s-s0).^2+(z-z0).^2);
606      fs1=@(s,z)
607    (c0s+A1s.*erf((rr1(s,z)+a1s)./b1s)+A2s.*erf((rr1(s,z)+a2s)./b2s)+A3s.*erf((rr1(s,z)+a3s)./b3s)+
608    A4s.*erf((rr1(s,z)+a4s)./b4s));
609
610      if polje == 1 || polje == 2
```

```matlab
611
612    fz1=@(s,z)(c0z+A1z.*erf((rr1(s,z)+a1z)./b1z)+A2z.*erf((rr1(s,z)+a2z)./b2z)+A3z.*erf((rr1(s,z)+
613    a3z)./b3z)+A4z.*erf((rr1(s,z)+a4z)./b4z)+A5z.*erf((rr1(s,z)+a5z)./b5z)+A0z.*erf(az./bz));
614      else if polje == 3
615        fz1=@(s,z)(c0z+A1z.*erf((rr1(s,z)+a1z)./b1z)+A2z.*erf((rr1(s,z)+a2z)./b2z));
616        end
617      end
618
619    f1=@(s,z) sqrt((fs1(s,z).*abs(s-s0)./rr1(s,z)).^2+(fz1(s,z).*abs(z-z0)./rr1(s,z)).^2)*s;
620
621    h=(s2-s1)/n; %calculation of an integral of top helispherical part
622    J1=0; J2=0; J3=0;
623    for i=0:n
624    s = s1 + i*h;
625    HX = (zf(s)-z00(s))/m;
626    K1 = f1(s, z00(s))+f1(s, zf(s));
627    K2 = 0; K3 =0;
628    for j=1:m-1
629     z = z00(s) + j*HX;
630     Q = f1(s,z);
631     if rem(j,2) == 0
632        K2 = K2 + Q;
633     else
634        K3 = K3 + Q;
635     end
636    end
637    L = (K1 + 2*K2 + 4*K3)*HX/3;
638    if  i == 0 || i == n
639       J1 = J1 + L;
640    else if rem(i,2) == 0
641         J2 = J2 + L;
642    else
643       J3 = J3 + L;
644       end
645    end
646    end
647    Juk5 = 2 * pi* h * (J1 + 2*J2 + 4*J3)/3;
648
649    kvol=V/(Juk1+Juk2+Juk5-Juk3-Juk4)
650
651    else if k==11 %RAZORnano chamber
652
653    h=(s2-s1)/n; %calculation of an integral of top half spherical part
654    J1=0; J2=0; J3=0;
655    for i=0:n
656    s = s1 + i*h;
657    HX = (zf(s)-z00(s))/m;
```

```
658    K1 = f1(s, z00(s))+f1(s, zf(s));
659    K2 = 0; K3 =0;
660    for j=1:m-1
661     z = z00(s) + j*HX;
662     Q = f1(s,z);
663     if rem(j,2) == 0
664        K2 = K2 + Q;
665     else
666        K3 = K3 + Q;
667     end
668    end
669    L = (K1 + 2*K2 + 4*K3)*HX/3;
670    if  i == 0 || i == n
671       J1 = J1 + L;
672    else if rem(i,2) == 0
673          J2 = J2 + L;
674    else
675       J3 = J3 + L;
676        end
677    end
678    end
679    Juk1RAZOR = 2 * pi* h * (J1 + 2*J2 + 4*J3)/3;
680
681    h=(s2-s1)/n; %calculation of an integral of bottom half spherical part
682    J1=0; J2=0; J3=0;
683    for i=0:n
684    s = s1 + i*h;
685    HX=(z00(s)-zf(s))/m;
686    K1 = f2(s, z00(s))+f2(s, zf(s));
687    K2 = 0; K3 =0;
688    for j=1:m-1
689     z = z00(s) + j*HX;
690     Q = f2(s,z);
691     if rem(j,2) == 0
692        K2 = K2 + Q;
693     else
694        K3 = K3 + Q;
695     end
696    end
697    L = (K1 + 2*K2 + 4*K3)*HX/3;
698    if  i == 0 || i == n
699       J1 = J1 + L;
700    else if rem(i,2) == 0
701          J2 = J2 + L;
702    else
703       J3 = J3 + L;
704        end
```

```
705     end
706     end
707     Juk2RAZOR = 2 * pi* h * (J1 + 2*J2 + 4*J3)/3;
708
709     h=(s3-s1)/n; %calculation of an integral of top half spherical part of an electrode
710     J1=0; J2=0; J3=0;
711     for i=0:n
712     s = s1 + i*h;
713     HX = (zf2(s)-z00(s))/m;
714     K1 = f1(s, z00(s))+f1(s, zf2(s));
715     K2 = 0; K3 =0;
716     for j=1:m-1
717      z = z00(s) + j*HX;
718      Q = f1(s,z);
719      if rem(j,2) == 0
720         K2 = K2 + Q;
721      else
722         K3 = K3 + Q;
723      end
724     end
725     L = (K1 + 2*K2 + 4*K3)*HX/3;
726     if  i == 0 || i == n
727        J1 = J1 + L;
728     else if rem(i,2) == 0
729           J2 = J2 + L;
730     else
731        J3 = J3 + L;
732        end
733     end
734     end
735     Juk3RAZOR = 2 * pi* h * (J1 + 2*J2 + 4*J3)/3;
736
737     h=(s3-s1)/n; %calculation of an integral of bottom half spherical part of an electrode
738     J1=0; J2=0; J3=0;
739     for i=0:n
740     s = s1 + i*h;
741     HX = (z00(s)- zf2(s))/m;
742     K1 = f2(s, z00(s))+f2(s, zf2(s));
743     K2 = 0; K3 =0;
744     for j=1:m-1
745      z = z00(s) + j*HX;
746      Q = f2(s,z);
747      if rem(j,2) == 0
748         K2 = K2 + Q;
749      else
750         K3 = K3 + Q;
751      end
```

```
752      end
753      L = (K1 + 2*K2 + 4*K3)*HX/3;
754      if  i == 0 || i == n
755        J1 = J1 + L;
756      else if rem(i,2) == 0
757          J2 = J2 + L;
758      else
759        J3 = J3 + L;
760        end
761      end
762      end
763     Juk4RAZOR = 2 * pi* h * (J1 + 2*J2 + 4*J3)/3;
764
765     kvol=V/(Juk1RAZOR + abs(Juk2RAZOR)-abs(Juk3RAZOR)-abs(Juk4RAZOR))
766       end
767      end
```

# List of Figures

# List of Tables

# List of abbreviations

## S

SRS

## T

TCPE